Exploring Earth's core-mantle boundary with multi-technique approaches

Thesis by
Vasilije V. Dobrosavljevic

In Partial Fulfillment of the Requirements for the
Degree of
Doctor of Philosophy

CALIFORNIA INSTITUTE OF TECHNOLOGY
Pasadena, California

2022
Defended May 26, 2022

Vasilije V. Dobrosavljevic
ORCID: 0000-0002-3710-2188

“Is the Master out of his mind?" she asked me.

I nodded.

"And he’s taking you with him?"

I nodded again.

"Where?" she asked.

I pointed towards the centre of the earth.

"Into the cellar?" exclaimed the old servant.

"No," I said, "farther down than that.”

-Jules Verne

Voyage au centre de la Terre

"Once I understand the heavens and earth are a giant forge, and transformation is the great ironsmith, wherever I go is just fine. Relaxed I nod off, and happily I awake."

-Zhuangzi

ACKNOWLEDGEMENTS

This thesis is the result of an incredible network of people who have nurtured my growth, supported my journey, and taught me innumerable lessons over many years. First and foremost, I extend my sincerest and deepest gratitude to my advisor Jennifer Jackson. When I arrived at Caltech in Fall 2016, I felt insecure in my scientific abilities and uncertain about my interests in a research career. In the nearly six years we worked together since then, Jennifer's approach to mentorship and research has nurtured my growth as a researcher, scientific thinker, collaborator, and human being. She has shared with me her genuine and contagious excitement for topics and questions of geoscience, the deep Earth, and the mysterious core-mantle boundary region. She motivated me to work hard without pushing me, encouraging me to take responsibility for my own path. At the same time, she constantly offered affirmation and support, cultivating my self-confidence and determination. She taught me the profound value and importance of patience, presence, deep thinking, and thoughtfulness, as both scientific best practices and keystones of healthy collaborative relationships. She showed me how to attend to the tiniest details while always coming back to the big picture. She stands for me as the utmost role model for a scientist, a mentor, and a friend. I feel so lucky to have had her as my advisor. I will cherish her wisdom for a lifetime and hope to pass it on to those I may have the chance to mentor myself.

Next, I want to express my gratitude and respect for the other members of my thesis committee: Mike Gurnis, for his deep understanding of the dynamic Earth, his insights during deep Earth discussions, his support of my career path, and his leadership of the very special environment of the Seismolab; Zhongwen Zhan, for his genuine enthusiasm, his kindness, and his exciting development of seismic techniques that promise to shed more and more light on what lies beneath our feet; and Paul Asimow, for his seemingly endless well of knowledge, his creative thinking, his excellent pedagogy, and his leadership of the unforgettable Pahoehoe trip.

I also thank all the other faculty members of the Seismolab and the GPS division who have taught me so much about our planet and about bold creative thinking. In particular, I would like to thank Tapio Schneider for taking me on in my first year as a mentee on my second project for my qualifying exam. Though my focus is on the deep Earth, Tapio welcomed me warmly and taught me a great deal about our

atmosphere and climate, along with then-postdoc Kyle Pressel. I must also express my gratitude and respect for the late Don Helmberger. Though I had limited personal interactions with him, it is clear how much he inspired generations of seismologists, students, and deep Earth scientists. His legacy will carry on for many generations to come. I also thank Wolfgang Sturhahn for his incredible sharp insights on atomic physics, the experimental techniques we use, and their theoretical underpinnings. He has been a warm and cheerful presence in our group, and his advice has been indispensable. A special thanks to Joe Kirschvink for inspiring me with his bold science, intuition, and leadership of the Ge136 trips, a really unique and memorable part of the GPS experience. It taught me that the best learning comes from casual conversation with peers and sharing excitement with those around you.

I would never have set out on the path of geoscience research if not for the support and encouragement of several incredible people. To Kanani Lee, my senior thesis advisor during my undergrad at Yale, I cannot begin to express my gratitude and appreciation for you. At a time when I was lost on what to do after college, you welcomed me into your lab, taught me so much, encouraged me to apply to grad schools for mineral physics, and supported me through the applications. You set a standard for me in terms of warm, supportive, and thoughtful advising. Your excitement for this field and my wonderful experience in your lab made me choose the path I'm on now. As part of that experience, I also give great thanks to Jennifer Girard, Zhixue Du, Jie Deng, Neala Creasy, Kierstin Daviau, and Sarah Arveson. You showed me what a vibrant research group looks like, and your insights were indispensable to me. Zhixue and Jie, I will never forget our trip to Brookhaven. I also am deeply grateful to Vincent Salters, who took me in to his geochemistry lab in Summer 2014 and first introduced me to the exciting world of geoscience and the mysteries of the ancient past and deep interior that we try to uncover. Your passion, kindness, and support then and later have been so meaningful to me. You taught me that the data tell a story, and it's up to us to discover it and share it with the world.

I am deeply thankful to the other members of the Jackson research group, both current and former. To Rachel Morrison, Natalia Solomatova, Greg Finkelstein, and Tyler Perez, you were so critical when I first arrived in welcoming me and supporting me. I will never forget my first beamtime in Berkeley and the many group meetings and get togethers we all shared. To Johannes Buchen, I will always cherish our time together and look forward with joy to our future meetings. You taught me so much about our field and about careful methodical work. To Olivia Pardo, I couldn't have

imagined a better person to share so many years with as a close friend, beamtime trip partner, and colleague. The wonderful memories over these years are too many to list. The COMPRES trip to Montana with Olivia and Johannes is truly a special memory. To Ben Strozewski, Ojashvi Rautela, and Jack Wilding, spending these last several years with you, though cut short by COVID, has been a true joy. I know you will all continue to blossom as scientists and go on to do great things. And to Cijin Zhou, it has meant so much to me to have had the chance to mentor you first in Summer 2019, and then to see you come to Caltech and grow as a scientist. I am so glad you chose to join us for graduate school and to enter into this field as a researcher. We will all benefit from your work and future insights.

In addition, I would like to express truly sincere gratitude to Dongzhou Zhang. Over my many visits to APS, you have been a constant source of support, knowledge, and joy. It has been so special to become friends and colleagues with you. I greatly admire your work and your drive, and I would not have been able to do these challenging melting experiments without you. I greatly look forward to our future meetings, discussions, and collaborations. I would like to further thank all the incredible scientists at the synchrotron beamlines who make this research possible and provide their deep knowledge. In particular, I would like to thank Jiyong Zhao and Tom Toellner at Sector 3 of the Advanced Photon Source (APS) and Stella Chariton and Vitali Prakapenka at Sector 13 of the APS. Your dedication to research is truly inspiring and motivating. I would also like to thank June Wicks for pioneering so much essential research on iron-rich (Mg,Fe)O and properties of the CMB and ULVZs. Your work has been my constant inspiration in this thesis. And a thanks to June, Caitlin Murphy, and Lisa Mauger for the synthesis of samples used in my research.

I would like to thank the administrative office for all their hard work in keeping the Seismolab running and for their genuine warmth and friendliness throughout my time here. In particular, I thank Sarah Gordon for all your support in making sure my travels to beamtime and conferences go smoothly. To Sarah and Donna Mireles, thank you both so much for all the chats and laughs we shared over the years. I also want to thank my various officemates and close friends over the years. In particular, to Vish, Minyan, Zhe, Xiaolin in my old office and to Yan in my new one. Beyond these good folks, I am deeply thankful for my cohort of geophysics students: Zhe, Zhichao, Ollie, Stacy, Celeste, and Valère. To spend so many years with you and to be reaching the finish line now and seeing how each of you has blossomed into

an outstanding scientist, presenter, and wonderful friend, that is truly special to me. To Katrina, Steve, and Nicole, our first year shenanigans were unparalleled, and I can't wait to keep that energy alive in years to come. To the "SeismoFam" as a whole and to the amazing students across GPS, I couldn't imagine a more wonderful group of people to work and share time with. I have felt so lucky to be part of this community, a really unique part of Caltech's campus. A special shout-out to Voon, Jack, and Jorge, you set a standard for us in terms of camaraderie and community building that I will never forget.

Beyond GPS, I have made so many incredible friends across and outside Caltech during my time in Pasadena. These folks have been constant sources of joy, love, adventure, and inspiration. There are too many to list but you know who you are, and I send you my gratitude and love, now and onward. These include the special communities in the Socialists of Caltech, the abolition reading group, and the Pasadena tenants union. To learn, grow, and work with you all on concrete projects with concrete outcomes has taught me lessons I would never have learned just doing my research. In the trying times ahead, may we cultivate that same dedication, solidarity, passion, love, and community that bring light to the world we live in. May we remember that, more than anything, we are human, and may we honor our kinship with all those worldwide who struggle for a brighter future for humanity and all life on this planet.

To my dearest friends from this chapter of my life: Peishi, Ollie, Stax, Eduardo, Wilbur, Weilai. The memories we have shared together could fill an entire thesis. You have been light, joy, and love for me. To grow, share, and laugh together has been a blessing I will cherish forever. You made Pasadena a warm home for me. In these last several quarantine years especially, I couldn't have asked for a better group to not just survive with but to thrive with in the darkest days. To have built lifelong friendships with you is a blessing and an honor, and I look forward to many many more years of togetherness.

To Kat, Dr. Katherine Zoe Rinaldi, my incredible partner and greatest love, I cannot put in words what these last few years have meant to me. Our connection has been a constant source of light and love radiating brightly in years of uncertainty and challenges. You inspire me relentlessly with your warmth, joy, kindness, energy, goofiness, sincerity, sociability, and courage. I'm filled with such excitement for the next chapter in our journey together. You have supported me in so many ways in this closing of my PhD time, and I am so eager to continue supporting you and watching

you build your path. To fully witness each other, accept each other, energize each other, care for each other, and help each other grow has been the most profound experience I've had. May we stay open and present for the many adventures and unexpected delights in our future ahead. And a special mention to Kat's sweet cat Panda, whose goofy vibes, gentle love, and soft belly have kept me company during long days of working from home.

And finally, to my parents Dragana and Vladimir, you have given me the greatest gift of all: unconditional, enduring love. Without your love, your support, your belief in me, the countless sacrifices and energy and time poured into my growth, I could never be where I am today and who I am today. Every day I cherish you, my grandparents, and our Serbian and Yugoslav ancestors, whose love, care, bravery, perseverance, honor, and wisdom have been carried through generations to me. For these roots and foundations, I am the most grateful of all.

The research in this thesis was funded by the National Science Foundation (NSF-EAR-1727020, NSF-EAR-CSEDI-2009935, NSF-CSEDI-EAR-1161046, and NSF-EAR-CAREER-0956166). GeoSoilEnviroCARS and Sector 3 operations are partially supported by COMPRES (NSF-EAR-1661511). GeoSoilEnviroCARS is supported by the National Science Foundation – Earth Sciences (NSF-EAR-1634415) and Department of Energy- GeoSciences (DE-FG02-94ER14466). Use of APS is supported by the U.S.DOE, Office of Science (DE-AC02-06CH11357). Advanced Light Source is a DOE Office of Science User Facilities under contract DE-AC02-05CH11231.

ABSTRACT

Earth's core-mantle boundary (CMB) is the most extreme interface of the planet's interior. It regulates the flow of heat out of the core and in doing so influences the two internal engines of our dynamic habitable planet: convection in the solid mantle and the magnetic geodynamo in the core. Seismic observations of the CMB have revealed a complex landscape of heterogeneous multi-scale structures that likely play key roles in Earth's internal dynamics and may hold memory of Earth's ancient past. Many details of the compositions and properties of these structures, however, are essentially unknown. In this thesis, I deploy a suite of experimental techniques and interdisciplinary approaches to constrain the temperature and phase relations of the CMB, properties that affect dynamics of the mantle and core. In particular, I focus my study on ultralow velocity zones (ULVZs) - the most extreme and perhaps least well understood structures in the lowermost mantle. I first quantitatively show that these structures, originally posited to be areas of partial melt, can be well explained as solid FeO-rich formations given seismic, geodynamic, and mineralogical constraints. To further explore the viability of such solid FeO-rich structures, I develop a multi-technique approach combining two *in-situ* synchrotron-based methods, one sensitive to crystal structure and another to atomic dynamics, to study the high-pressure melting of iron-bearing materials. With this approach, I place new constraints on the core-mantle boundary temperature by measuring the melting temperature of a candidate core-forming alloy ($Fe_{0.8}Ni_{0.1}Si_{0.1}$) at high pressures, finding that the addition of silicon to an $Fe_{0.9}Ni_{0.1}$ core can reduce CMB temperatures to ~3500 K. I then measure the melting of $Fe_{0.94}O$, finding a melting temperature of 4140 ± 110 K at CMB pressure, demonstrating the stability of solid FeO-rich ULVZs in the lowermost mantle. The melting experiments show strong agreement between the two independent techniques, helping to address sources of large discrepancies in previous high-pressure melting experiments. Reported high conductivity for iron-rich (Mg,Fe)O at CMB conditions may provide a mechanism for upwelling promoted by solid conductive ULVZs at roots of major hotspot plumes. As a whole, the thesis advances our understanding of the compositions and origins of ultralow velocity zones and, more broadly, the physical properties of Earth's core-mantle boundary region.

PUBLISHED CONTENT AND CONTRIBUTIONS

Dobrosavljevic, V. V., Zhang, D., Sturhahn, W., Zhao, J., Toellner, T. S., Chariton, S., Prakapenka, V. B., Pardo, O. S., & Jackson, J. M. (2022). Melting and phase relations of Fe-Ni-Si determined by a multi-technique approach. *Earth and Planetary Science Letters*, *584*, 117358. https://doi.org/10.1016/j.epsl.2021.117358.

V.V.D. conducted the experimental work and data analysis, wrote the original manuscript, and conceived of the study with J.M.J.

Lai, V. H., Helmberger, D. V., Dobrosavljevic, V. V., Wu, W., Sun, D., Jackson, J. M., & Gurnis, M. (2022). Strong ULVZ and Slab Interaction at the Northeastern Edge of the Pacific LLSVP Favors Plume Generation. *Geochemistry, Geophysics, Geosystems*, *23*(2). https://doi.org/10.1029/2021GC010020.

V.V.D. contributed the mineralogical analysis and writing of the relevant section (4.1), as well as discussion with V.H.L. on the seismic tradeoff analysis and editing of the entire manuscript.

Dobrosavljevic, V. V., Sturhahn, W., & Jackson, J. M. (2019). Evaluating the Role of Iron-Rich (Mg,Fe)O in Ultralow Velocity Zones. *Minerals*, *9*(12), 762. https://doi.org/10.3390/min9120762.

V.V.D. conducted the experimental work and data analysis, wrote the original manuscript, and conceived of the study with J.M.J.

TABLE OF CONTENTS

Acknowledgements iv
Abstract ix
Published Content and Contributions x
Table of Contents x
Chapter I: Introduction 1
1.1 Earth's core-mantle boundary 1
1.2 Ultralow velocity zones in Earth's lowermost mantle 3
1.3 Temperature of the lowermost mantle and core 4
1.4 Thesis overview 5
Chapter II: Evaluating the role of iron-rich (Mg,Fe)O in ultralow velocity zones 7
2.1 Introduction 7
2.2 Materials and methods 9
2.3 Experimental results 10
2.4 Modeling iron-rich (Mg,Fe)O in the lowermost mantle 14
Chapter III: Interdisciplinary approaches for quantifying compositions of ultralow velocity zones:
Case study of a region underneath Hawai'i 20
3.1 Introduction 20
3.2 Mineralogy of ULVZ 22
3.3 Conclusion 27
Chapter IV: Constraining temperatures of Earth's core: melting and phase relations of Fe-Ni-Si determined by a multi-technique approach 29
4.1 Introduction 29
4.2 Methods 31
4.3 Results 35
4.4 Discussion 46
4.5 Conclusion 52
Chapter V: Melting and vacancy structure transitions in $Fe_{0.94}O$ up to 140 GPa 53
5.1 Introduction 53
5.2 Methods 55
5.3 Data analysis 56
5.4 Results and interpretations 60
5.5 Discussion 65
Chapter VI: Conclusion 69
Bibliography 72
Appendix A: Supplementary Material for Chapter 2 92
Appendix B: Supplementary Material for Chapter 3 100
Appendix C: Supplementary Material for Chapter 4 104
C.1 Sample preparation procedures 104

C.2 Temperature-laser power relationships 105
C.3 Choice of background regions for detecting liquid diffuse signals . . 106
C.4 Equations of state 108
C.5 Thermal pressure modeling 108
C.6 Error analysis for calculating phase boundaries and the triple point locations 110
C.7 Recalculating melting pressures from previous studies and refitting melting curves of *fcc*-Fe and *fcc*-$Fe_{0.9}Ni_{0.1}$ 111
Appendix D: Supplementary Material for Chapter 5 134

Chapter 1

INTRODUCTION

1.1 Earth's core-mantle boundary

Multidisciplinary research over the last several decades is increasingly supporting the view that surface processes critical to Earth's habitability – such as the production of continental crust and the recycling of life-forming volatile elements – are expressions of dynamic processes that extend all the way down to Earth's core-mantle boundary (CMB) (H.-k. Mao & Mao, 2020; Tatsumi & Stern, 2006; Tatsumi et al., 2014). Advances in deep Earth seismic observation (French & Romanowicz, 2015; Hosseini et al., 2020; Shen et al., 2020; Zhan, 2020), mineral physics experiments at extreme conditions (J. Liu et al., 2019; Ohtani, 2020), and geodynamic simulations of the convecting rocky mantle (Gülcher et al., 2020; Hu et al., 2022) together have demonstrated that subducted oceanic crust can transport critical volatile elements like carbon, hydrogen, and oxygen to the base of the mantle, where deep-rooted upwelling plumes form and rise to return recycled material back to the surface. These scientific advances have definitively highlighted the centrality of the deep interior in sustaining Earth's habitable surface, and new questions have been raised around the role of the CMB in triggering major events of Earth's evolutionary history. Such events may include the merging and rifting of supercontinents (Gurnis, 1988; Mitchell et al., 2021; Santosh et al., 2009; Shirey & Richardson, 2011), the Great Oxidation Event (Holland, 2002), snowball Earth events (Hoffman et al., 1998; Kopp et al., 2005), and mass extinction events in the biosphere (Schmidt et al., 2016).

While the complexity of the Earth's surface has received extensive study and benefited from unified descriptions of diverse observations as in the plate tectonics revolution of the 1960s (McKenzie & Parker, 1967), basic understanding of the core-mantle boundary has started to develop only in the last few decades with technical developments in seismological and mineral physics capabilities (Bower et al., 2013; Bower et al., 2011; Garnero & Helmberger, 1998; Hirose et al., 2017; H.-k. Mao & Mao, 2020; McNamara, 2019; D. Sun et al., 2009; D. Sun et al., 2013; Wicks et al., 2010; Yu & Garnero, 2018). As the most extreme interface of Earth's interior, the CMB is believed to play a key role in planetary evolution and habitability through

its regulation of heat flow from the core to the mantle. In this role, the CMB – like a hot plate at the mantle base – provides a driving force for mantle convection, while its control on heat escaping the core powers the geodynamo that creates and sustains the magnetic field necessary for shielding the planet from the Sun's harmful radiation (Olson, 2013).

Beyond these basic roles, however, most details about the CMB remain enigmatic. Seismology is increasingly revealing a heterogeneous landscape of multi-scale structures (Fig. 1.1a), from continent-sized thermochemical piles to kilometer-sized small anomalies that scatter seismic waves (Jackson & Thomas, 2021; Ni et al., 2002; B. Zhang et al., 2018). Such a complex landscape suggests heterogeneous heat flow across the CMB, with implications for reversals in the magnetic field and for the locations of deep-rooted mantle plumes (Jellinek & Manga, 2002, 2004). This region may contain primordial material formed during the solidification of the mantle and could thus hold key information about Earth's early evolution and the onset of plate tectonic convection (McNamara, 2019). All of these details depend entirely on the precise temperature of the region and on the compositions and material properties of the heterogeneous structures, both are which are closely intertwined. However, these properties are largely unconstrained, presenting a major obstacle for our understanding of the CMB and its role in the solid Earth system.

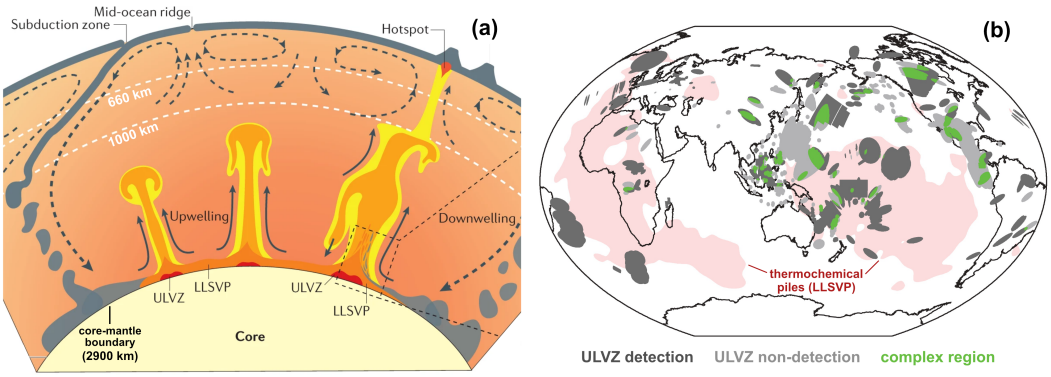

Figure 1.1: (a) Simplified cross-section of Earth's deep interior, modified from Koppers et al. (2021), showing ultralow velocity zones (ULVZs) at mantle plume roots and at edges of thermochemical piles (large low-seismic velocity provinces – LLSVPs). (b) Distribution of core-mantle boundary locations featuring evidence (dark), no evidence (light), and mixed evidence (green) for ULVZs, modified from Yu and Garnero (2018).

1.2 Ultralow velocity zones in Earth's lowermost mantle

The most extreme and perhaps least well understood structures at the CMB are the ultralow velocity zones (ULVZs). These mountain-like mid-scale structures – 10s of km in height and 100s of km wide – feature extreme velocity reductions, as large as ~50% lower than the surrounding mantle, as well as relative density increases up to 15% (e.g., Yu and Garnero, 2018). Since the earliest detections of these anomalous structures in the late 1990s (Garnero & Helmberger, 1998), seismic imaging has discovered ULVZs in a diverse set of locations (Fig. 1.1b): at the roots of major deep-mantle plumes that source volcanic surface hotspots like Hawai'i, Iceland, and Yellowstone over millions of years and around the edges of large thermochemical piles where cold subducted slabs interact with hot upwellings (Yu & Garnero, 2018). A recent discovery of a "snake-like" mountain range underneath Samoa may represent a new type of actively migrating ULVZ (Krier et al., 2021). These structures represent a local phenomenon that may generate and sustain upwelling plumes and hotspot volcanism and a global phenomenon whose heterogeneous distribution across the CMB could affect magnetic field generation and mantle convection. ULVZs have also been suggested to be transient structures formed from a thin (< 5 km) ubiquitous layer of possibly primordial material blanketing the CMB (Yu & Garnero, 2018), though the timescales of such ULVZ lifecycles are unknown.

Since the discovery of ULVZ regions along the CMB (Garnero & Helmberger, 1998), researchers have proposed a range of physical phenomena that could cause such extreme velocity reductions. The proposed hypotheses can generally be grouped into two categories: varieties of partial melting and iron enrichment of solid mineral phases, or possibly a combination of both. The partial melting hypothesis, whether of ambient mantle material (Williams & Garnero, 1996) or of subducted slab debris (Andrault et al., 2014; J. Liu et al., 2016; Ohtani & Maeda, 2001), is challenged by a lack of *in-situ* experimental data on how sound velocities are affected by the presence of partial melt, as well as by persistently large uncertainties in CMB temperatures (Anzellini et al., 2013; Dobrosavljevic et al., 2022; D. Zhang et al., 2016). It may also be difficult to appeal to partial melting to explain the frequent detection of ULVZs relatively distant from the hottest areas of the CMB, as at the edges of large thermochemical piles (M. Li et al., 2017). In addition, it is unclear from geodynamic studies whether partially molten material without compositional heterogeneity like iron enrichment could produce observed ULVZ morphologies (Dannberg et al., 2021; Hernlund & Jellinek, 2010; Hernlund & Tackley, 2007). For iron enrichment, researchers have proposed the possibility

of subducted banded iron formations (Dobson & Brodholt, 2005), hydrous iron peroxide (J. Liu et al., 2017), iron-rich (Mg,Fe)O magnesiowüstite (Finkelstein et al., 2018; Finkelstein et al., 2017; Wicks et al., 2010; Wicks et al., 2017), and iron-enriched post-perovskite (W. L. Mao et al., 2006), though large disagreements between experimental (W. L. Mao et al., 2006) and theoretical (Caracas & Cohen, 2006) values of post-perovskite elasticity at CMB conditions preclude robust evaluation of this hypothesis.

More broadly, little progress has been made in quantifying mineralogical assemblages that could viably explain specific ULVZ observations, given uncertainties in both seismic interpretations and mineralogical data, as well as geodynamic constraints on realistic morphologies (Jackson & Thomas, 2021; Reali et al., 2019). Such quantitative treatment is necessary for statistical comparison of proposed hypotheses and the possibility of ruling out certain suggested explanations. Unlocking the origins of ULVZs and their roles in Earth's evolution requires progress in determining viable compositions and consequent physical properties, which are still largely unconstrained and represent a fundamental gap in the current understanding of how our planet works.

1.3 Temperature of the lowermost mantle and core

As highlighted above, the precise temperature of the core-mantle boundary region affects numerous aspects of the deep Earth. These include the determination of viable compositions of ULVZs and other heterogeneous structures in the lowermost mantle, the consequent physical properties of these features, and the rate of heat flow through the region. The latter in turn affects the onset and convective rigor of the core's geodynamo that powers the magnetic field, as well as the dynamics of mantle convection. The temperature of the core-mantle boundary largely depends on the thermal profile of the outer core, which is generally constructed as an adiabatic profile anchored at the solid-liquid interface of the outer core - inner core boundary. This anchor temperature has been investigated by experiments measuring the high-pressure melting temperatures of iron and iron alloys proposed as core compositions (Anzellini et al., 2013; Morard et al., 2011; Sinmyo et al., 2019; Torchio et al., 2020; D. Zhang et al., 2016). However, such studies have exhibited persistently large disagreements on melting temperatures at high pressure, leading to uncertainties on CMB temperatures as large as 1000 K. Such experiments are particularly challenging due to necessarily small sample volumes required to reach high pressures in diamond anvil cells and associated difficulties in precisely

detecting the onset of melting in the samples. In addition, the composition of the core itself remains a major open question of deep Earth science, presenting yet another challenge for placing precise constraints on core temperatures. As a result, there are many outstanding questions regarding the accuracy of various techniques used for measuring melting and possible sources of error that could affect previous discrepant results.

1.4 Thesis overview

In this thesis, I use multi-technique experimental approaches and interdisciplinary collaboration to address open questions regarding the compositions of ultralow velocity zones and the temperature of the core-mantle boundary region. In Chapter 2, I use measurements at high pressure and 300 K improve the precision of the equation of state of solid iron-rich (Mg,Fe)O magnesiowüstite, a material proposed to explain the low velocities of ULVZs. With these results, I calculate elastic properties of magnesiowüstite and coexisting minerals at CMB conditions. We then develop a mixing model to find best-fitting compositions for observed ULVZ properties, given uncertainties in both the seismic observations and mineral elastic properties. In Chapter 3, I extend this approach by incorporating constraints from previous geodynamic simulations of solid iron-rich ULVZs and apply it to a case study of a region under Hawai'i in collaboration with an interdisciplinary team of deep Earth scientists. We find that a solid magnesiowüstite-bearing ULVZ is compatible with constraints from seismology, mineral physics, and geodynamics. Consideration of correlated uncertainties shows that such an assemblage can produce velocity reduction ratios commonly used to justify a partial melt explanation of ULVZs.

In Chapter 4, we develop a multi-technique experimental approach to measure the melting and solid phase relations of iron-bearing materials, combining two *in-situ* techniques – synchrotron Mössbauer spectroscopy and synchrotron x-ray diffraction. I apply this approach to $Fe_{0.8}Ni_{0.1}Si_{0.1}$, shown to be compatible with Earth's core composition, and find that the addition of 10mol% silicon reduces melting temperatures of $Fe_{0.9}Ni_{0.1}$ by 500 K at core temperatures, implying a CMB temperature of 3500 K. We find excellent agreement on melting temperatures between the two independent techniques and address discrepancies in previous studies on the melting of iron. In Chapter 5, I investigate whether proposed FeO-rich ULVZs could be solid in the present-day lowermost mantle, given our new constraint on the CMB temperature. To do so, I apply the multi-technique approach to measure the melting

of $Fe_{0.94}O$, the end-member of the (Mg,Fe)O magnesiowüstite solid solution with the lower melting temperature. We find that iron vacancies in the material form long-range ordered structures at moderately elevated temperatures and undergo an order-disorder transition several hundred kelvin below melting, processes observed at ambient pressure but never studied at high pressures. We constrain a melting temperature of 4140 ± 110 K at the core-mantle boundary, suggesting that FeO-rich ULVZs can exist as solid structures in the present-day lowermost mantle. Chapter 6 summarizes the work in the thesis, highlights outstanding questions in the topics of study, and suggests avenues for future research to advance our understanding of Earth's core-mantle boundary region.

Chapter 2

EVALUATING THE ROLE OF IRON-RICH (Mg,Fe)O IN ULTRALOW VELOCITY ZONES

**This chapter has been previously published as*

Dobrosavljevic, V. V., Sturhahn, W., & Jackson, J. M. (2019). Evaluating the Role of Iron-Rich (Mg,Fe)O in Ultralow Velocity Zones. *Minerals, 9*(12), 762. doi.org/10.3390/min9120762.

2.1 Introduction

The boundary layer separating the iron-dominant liquid outer core from the silicate-rich mantle is a region of great complexity, where extreme contrasts in material properties promote the persistence of multiscale structural heterogeneities (e.g., Cobden et al., 2015; Lay, 2015; Lay and Helmberger, 1983). The thermoelastic variations at the lowermost mantle play a dominant role in the evolutionary history of the Earth through regulation of heat flow and consequent influence over the dynamics of both the mantle and the core. Despite the centrality of this region in the development of the solid Earth system, many open questions remain regarding the characteristics, origins, and dynamic interactions of observed heterogeneities, such as large thermochemical piles, ultralow velocity zones, subducted former oceanic material, and small seismic scatterers. As individual observational studies of such features and experimental investigations into candidate compositions continue to develop, synthesis of results from seismology and mineral physics provides quantitative and systematic avenues for revealing new insights into this complex region.

Advances in seismological observation over the past several decades have provided increasing evidence for the existence of ultralow velocity zones (ULVZs) — small (<50 km in height) localized seismic anomalies at the base of the mantle that are characterized by significant reductions in velocities (up to 25% and 50% for P and S waves, respectively) and likely increases in density (up to 20%) relative to the surrounding mantle (Garnero and Helmberger, 1998; McNamara et al., 2010; Thorne and Garnero, 2004, see also Yu and Garnero, 2018 for a recent review). To date, less than 20% of the core–mantle boundary (CMB) has been explored by

seismic studies investigating ULVZs, yet the existing observations of ULVZs reveal a large variety of elastic properties, locations, and structural geometries (e.g., Yu and Garnero, 2018). Nevertheless, the growing set of seismic studies observing diverse ULVZ properties can inform us of the causes of such significant velocity reductions. Whether all ULVZs share common characteristics and/or origins and what dynamical links may exist between them and other multi-scale features like slabs or slab debris, large thermochemical piles, and upwelling mantle plumes is the subject of current multidisciplinary research.

The very existence of ULVZs poses the question of their origin and dynamics and has attracted a variety of proposed explanations, including an iron-bearing layer of FeO and FeSi (Knittle & Jeanloz, 1991a; Manga & Jeanloz, 1996), iron-enriched postperovskite (Mg,Fe)SiO_3 (W. L. Mao et al., 2006), subducted banded iron formations (Dobson & Brodholt, 2005), silicate sediments from the core (Buffet et al., 2000), melt within subducted oceanic crust (Andrault et al., 2014; Ohtani & Maeda, 2001; Pradhan et al., 2015), slab-derived metallic melt (J. Liu et al., 2016), and partial melting of mantle material (Berryman, 2000; Williams & Garnero, 1996). Reports of preferential iron partitioning into ferropericlase coexisting with bridgmanite or postperovskite (Sinmyo et al., 2008) have motivated recent high-pressure experimental studies on iron-rich compositions of (Mg,Fe)O. These materials show remarkably low sound velocities (Wicks et al., 2010; Wicks et al., 2017), and dynamic modeling work on assemblages containing this material could reproduce the velocities and topography of some observed ULVZs (Bower et al., 2011). In addition, recent seismic and dynamic studies have suggested that compositionally distinct origin may be necessary to explain many ULVZs (Brown et al., 2015; M. Li et al., 2017). However, quantitative comparisons of such proposed features with seismic observations remain largely unexplored, creating difficulty in evaluating the likelihood of proposed explanations.

With this study, we aim to develop a quantitative approach to assess the role of iron-rich (Mg,Fe)O in ULVZs. First, we present new measurements of the compressional behavior of $(Mg_{0.06}Fe_{0.94})O$ in a helium pressure medium at ambient temperatures using synchrotron X-ray diffraction and produce a well-constrained equation of state for this material, which had not been done previously (Wicks et al., 2015). We combine these results with sound velocities and thermo-elastic information from previous studies (Finkelstein et al., 2017; Wicks et al., 2017; Wicks et al., 2015) to calculate the densities and velocities of iron-rich (Mg,Fe)O com-

positions at CMB pressure–temperature conditions. Using recent thermoelasticity measurements of bridgmanite and calcium silicate perovskite, we calculate seismic properties of coexisting mineral assemblages containing iron-enriched (Mg,Fe)O and build a linear mixing model that combines uncertainty estimates from both mineral physics and seismic observations to invert for the best-fit concentrations of iron-rich (Mg,Fe)O for select ULVZ observations. While an inversion approach has been used for other applications, such as constraining the composition of the bulk lower mantle (Matas et al., 2007), this study applies a similar approach to constraining the compositions of ULVZs. Our study quantifies the viability of iron-rich (Mg,Fe)O to account for certain classes of ULVZ seismic observations and, in doing so, contributes to developing a framework for a systematic evaluation of proposed origins of ULVZs.

2.2 Materials and methods

A sample of polycrystalline $(Mg_{0.058(1)}Fe_{0.942(1)})O$, hereafter referred to as Mw94, mixed with NaCl powder, was synthesized at ambient pressure conditions using 95% enriched ^{57}Fe and MgO powders, with ferric iron content capped at 5% by conventional Mössbauer spectroscopy (Wicks et al., 2015). The powdered sample was loaded inside a rhenium gasket between two beveled diamond anvils of 250 μm diameter within a symmetric diamond-anvil cell. The sample chamber also contained two ruby spheres for use as pressure markers by measurement of their pressure-dependent fluorescence spectra. The chamber was then loaded with compressed helium gas at 170 MPa, explicitly chosen as a pressure-transmitting medium to minimize the nonhydrostatic behavior of the pressure environment (e.g., Finkelstein et al., 2017), using the gas-loading system at Caltech.

2.2.1 X-ray Diffraction

High-pressure X-ray diffraction experiments were performed at Beamline 12.2.2 of the Advanced Light Source (ALS) of Lawrence Berkeley National Laboratory (Berkeley, CA, USA). The LaB_6 standard was used to calibrate the sample to detector distance. Diffraction patterns at each pressure point were collected using a high-resolution image plate (MAR345) with an incident X-ray energy of 25 keV and a size of about 10 μm x 10 μm (full width at half maximum). Diffraction patterns were collected at a series of 27 compression points across the pressure range of 1.5 to 88.7 GPa. Intervals between pressure steps were limited to ~2 GPa for the range below 30 GPa, in order to finely sample the compressional behavior of the material in the

low-pressure regime, a critical step for tightly determining the material's equation of state.

Measurements of the ruby fluorescence spectra were performed immediately before and after each diffraction measurement, using the pressure scale of Dewaele et al. (2008). The cell was allowed to rest for 15 min on average after pressure increases, in order to reduce pressure creep during the collection of diffraction patterns. The uncertainty in pressure at each step was estimated as the difference of the pressures measured for the two rubies before and after each diffraction measurement. Diffraction patterns were radially integrated from the 2D image plate using the Dioptas software (Prescher & Prakapenka, 2015). Selected diffraction patterns are shown in Figure A.1. Peaks for Mw94 and NaCl, as well as for ruby and rhenium, were identified and fit using the GSAS-II software (Toby & Von Dreele, 2013) to derive the unit cell volume for Mw94 at each pressure point. The unit cell volumes of NaCl were used as a secondary pressure gauge (Fei et al., 2007) when present in the diffraction patterns and confirmed pressures determined by ruby fluorescence.

2.2.2 Synchrotron Mössbauer Spectroscopy

We complement our diffraction data with synchrotron Mössbauer spectroscopy (SMS) performed at Sector 3-ID-B of the Advanced Photon Source (APS) at Argonne National Laboratory (Lemont, IL, USA), using top-up mode of the storage ring with 24 bunches separated by 153 ns. X-rays were focused to an area of about 12 μm x 18 μm and tuned to 14.4125 keV, a nuclear transition energy of ^{57}Fe. A high-resolution monochromator provided an energy bandwidth of 1 meV (Toellner, 2000). A time window of 25 to 125 ns after excitation was used to observe nuclear resonant forward scattering and to fit the data. We performed SMS measurements at three compression points (95.4, 97.0, and 116.4 GPa) on the identical sample used for the diffraction measurements, in order to determine the magnetic ordering and spin state. Pressures were measured before and after SMS data collection using ruby fluorescence (Dewaele et al., 2008) and Raman spectroscopy, using the high-frequency edge of the diamond Raman band (Akahama & Kawamura, 2010).

2.3 Experimental results

The unit cell volume per atom of Mw94 at each compression point was calculated using the following hkl reflections: 111, 200, 220, 311, and 222 for B1; 003, 101, 102, 104, 110, and 105 for the rhombohedral phase (Figures 2.1 and A.2, and Table A.1). The splitting of 111 and 220 B1 peaks was observed at 34.5 GPa, suggesting a

rhombohedral distortion of the cubic lattice. We bracketed this structural transition from the B1-cubic phase to a rhombohedral phase between 30.1 and 34.5 GPa. The material remains in the rhombohedral phase up to at least 88.7 GPa. We observed a change in the trend of the unit-cell volume as a function of pressure at the two compression points prior to the structural transition (26.8 GPa, 30.1 GPa) and excluded these data in fitting the equation of state.

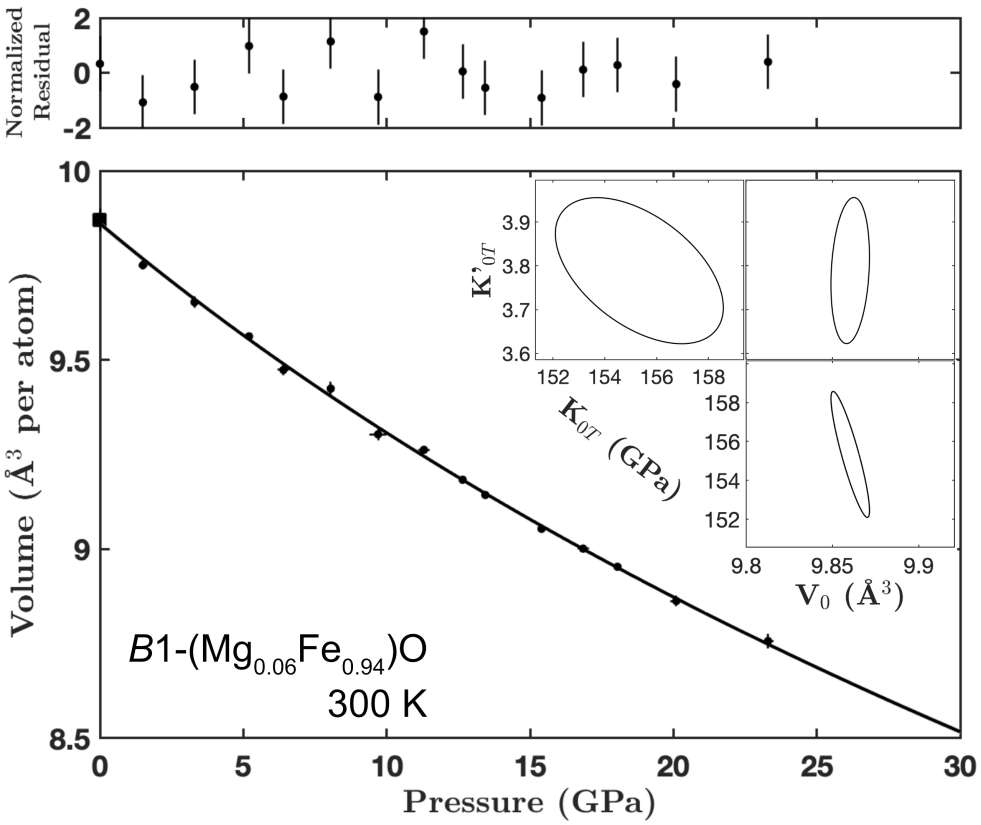

Figure 2.1: Unit-cell volumes of B1-($Mg_{0.058(1)}Fe_{0.942(1)}$)O (Mw94) (solid black circles) and equation of state (solid black line) fit using MINUTI (Sturhahn, 2021). The uncertainty in pressure at each step was estimated as the difference of the pressures measured by the two rubies before and after each diffraction measurements. We include a zero-pressure measurement of Mw94 (solid black square) from a previous study (Wicks et al., 2015) for comparison. Normalized residuals are shown on the top panel. Error ellipses demonstrate the correlations between fit parameters.

2.3.1 Equation of State (B1 Phase)

The pressure–volume data for the B1-cubic phase and for the rhombohedral phase were fit separately with two distinct equations of state using the MINUTI software package (Sturhahn, 2021). We used a third-order Burch–Murnaghan equation of state and varied the fit parameters V_0, K_{0T}, and K'_{0T} representing the zero-pressure unit cell volume per atom, the isothermal zero-pressure bulk modulus, and its pressure derivative, respectively. Due to large tradeoffs between K_{0T} and K'_{0T} and motivated by previous reports of K'_{0T} values for similar compositions (see Finkelstein et al., 2017), we performed the fit using an initial value of 3.8 for K'_{0T} with a prior window of 0.3; given the reduced χ^2 value of 0.70 ± 0.23 using this prior and an equivalent value of χ^2 = 0.74 ± 0.25 with no prior, we find the prior information to be a good fit to the data. For the B1-cubic phase, the best fit parameters are V_0 = 9.860 ± 0.007 Å^3 /atom, K_{0T} = 155.3 ± 2.2 GPa, K'_{0T} = 3.79 ± 0.11 (Table 2.1), which are significantly more compatible with the trends of K_{0T} as a function of iron concentration presented in Finkelstein et al. (2017) for the (Mg,Fe)O solid solution, compared with the results from an X-ray diffraction study of Mw94 from the same bulk sample (Wicks et al., 2015). These results underscore the need to perform measurements using a helium pressure medium in the low pressure regime, which were absent in the experimental range of Wicks et al. (2015). While the choice of neon or helium as the pressure medium can have a significant effect on elastic properties and transition pressure ranges for the (Mg,Fe)O system, the effect may be different for other phases with different crystal structures, such as (Mg,Fe)SiO_3 and $CaSiO_3$.

2.3.2 Equation of State (Rhombohedral Phase)

We fit a third-order Burch–Murnaghan isothermal equation of state to the pressure–volume data for the rhombohedral phase and found best fit parameter values V_0 = 9.59 ± 0.10 Å3 /atom, K_{0T} = 217 ± 19 GPa, K'_{0T} = 2.06 ± 0.22, with a reduced χ^2 value of 1.37 ± 0.37 (data and fit with residuals is shown in Figure A.2). While Wicks et al. (2015) bracketed the transition pressure for the cubic to rhombohedral transition between 13 and 24 GPa for a sample of Mw94 in a neon pressure medium, we observed a transition pressure in the range of 30.1 to 34.5 GPa for Mw94 in a helium medium. It is likely that a steep increase of non-hydrostaticity at ~20 GPa caused by neon compared to helium (Finkelstein et al., 2017) induced the rhombohedral distortion at a lower pressure.

2.3.3 Synchrotron Mössbauer Spectroscopy

In order to explore the possibility of a high-pressure ferrous-iron spin transition in Mw94, we performed synchrotron Mössbauer spectroscopy (SMS) on Mw94 at three compression points (95.4 ± 0.2, 97.0 ± 0.5, and 116.4 ± 0.5 GPa). Pressures were determined by Raman spectroscopy using the high-frequency edge of the diamond Raman band (Akahama & Kawamura, 2010), with uncertainties estimated as the difference of pressures before and after SMS measurements and of pressures at two different locations on the anvil. At the two lower pressures, we observed fast oscillations in the time spectra that are caused by magnetic ordering in the sample. At 116.4 GPa, a significant fraction of the fast oscillations was no longer present (Figure A.3), suggesting an absence of magnetic ordering that could indicate a high-spin to low-spin transition occurring in the Fe^{2+} sites of Mw94. In order to evaluate the possibility of a spin transition, we used the CONUSS software version 2.2.0 (Sturhahn, 2000) to fit the 116.4 GPa spectrum. We found that three distinct Fe^{2+} environments are required to fit the spectrum. One site is characteristic of low-spin Fe^{2+} and the other two sites are characterized by high-spin Fe^{2+}-like sites: one with no magnetic ordering and one with a magnetic hyperfine field. The best-fit model (Table A.2) shows that 37 ± 2% of the iron atoms have transitioned into the low-spin state at 116.4 GPa, with 3% of the iron atoms retaining the magnetic ordering in a high-spin state, and the remaining fraction indicative of a broad high-spin Fe^{2+}-like site with no magnetic ordering. The pressure of the Fe^{2+} spin transition suggested by this result is consistent with the trend of increasing spin transition pressure with increasing iron content in (Mg,Fe)O (e.g., Solomatova et al., 2016; Wicks et al., 2010). It should be noted that Mw94 is in the rhombohedral phase at the P–T conditions of these SMS measurements, so the reduced symmetry of the crystal structure compared to the B1 phase may affect the pressure range of the spin transition. The temperature dependence of the spin state in Fe-rich (Mg,Fe)O at CMB conditions has not been thoroughly studied, although the higher temperatures of Earth's mantle would likely drive the spin transition to higher pressures than those expected within the mantle (e.g., Sturhahn et al., 2005; Tsuchiya et al., 2006). Taken together, these results suggest that, unlike for ferropericlase (Wu & Wentzcovitch, 2014), the fraction of low-spin magnesiowüstite would either be relatively low or negligible at CMB conditions.

2.4 Modeling iron-rich (Mg,Fe)O in the lowermost mantle

2.4.1 Calculating Iron-Rich (Mg,Fe)O Elasticity at CMB Conditions

Mw94 has been reported to remain in the B1-cubic phase along the mantle geotherm up to CMB conditions (Wicks et al., 2015). We thus combined our results with those from previous studies in order to calculate the densities and sound velocities of iron-rich (Mg, Fe)O compositions at the pressure and temperature of the CMB. We first calculated the bulk sound velocity for Mw94 at 135.8 GPa (CMB pressure given in PREM) and 300 K using our isothermal equation of state. We then used this value and the Debye velocity V_D = 4.27 ± 0.09 km/s reported by Wicks et al. (2017) for an identical composition at the same pressure–temperature condition in order to calculate a V_P and V_S for Mw94 at 135.8 GPa and 300 K, following the procedure taken by Wicks et al. (2017). We applied the temperature corrections reported by Wentzcovitch et al. (2010) for MgO at CMB conditions to our results and thereby calculated the sound velocities for Mw94 at 135.8 GPa and 3800 K. In addition, we incorporated the thermal parameters reported by Wicks et al. (2015) for Mw94 in order to calculate the density of Mw94 at 135.8 GPa and 3800 K. We then repeated this procedure for Mw84 by using the same equation of state except with a zero-pressure volume V_0 = 9.79 ± 0.04 Å^3 /atom as reported by Wicks et al. (2017), and for Mw78 using the isothermal equation of state reported by Finkelstein et al. (2017). In doing so, we computed V_P, V_S, and density with uncertainties estimated from experimental reports (Table A.3) for the behavior of three iron-rich compositions of (Mg,Fe)O at the pressure–temperature conditions of the CMB. We note that while the equation of state for these iron-rich compositions is taken from measurements of the B1 phase that exists at CMB conditions, the measurements reported for the Debye velocity at lower mantle pressures (Wicks et al., 2017) were performed on the rhombohedral phase. Nevertheless, these values reflect the best available understanding of this material's shear elastic behavior. It is also important to note that Wicks et al. (2017) found no discernible compositional dependence of the Debye velocity for Mw84, Mw94, and FeO (Wicks et al., 2017), such that the effect of composition appears primarily in the equations of state used for extrapolation (Table 2.1).

2.4.2 Forward Modeling

Having calculated sound velocities and densities for three iron-rich compositions of (Mg,Fe)O at the pressure–temperature conditions of the CMB, we next investigated the likelihood of the presence of this material in ULVZs given the

Table 2.1: Isothermal equation of state parameters for the B1 and rhombohedral phases of Mw94, with thermal equation of state models for three iron-rich compositions of Mw.

Parameters	B1–Mw94	r–Mw94	Mw94 Model [a]	Mw84 Model [b]	Mw78 Model [c]
V_0 (Å^3 /atom)	9.860 ± 0.007	9.59 ± 0.10	9.860 ± 0.007	9.79 ± 0.04	9.86 ± 0.02
K_{0T} (GPa)	155.3 ± 2.2	217 ± 19	155.3 ± 2.2	155.3 ± 2.2	148 ± 3
K'_{0T}	3.79 ± 0.11	2.06 ± 0.22	3.79 ± 0.11	3.79 ± 0.11	4.09 ± 0.12
θ_0 (K)	—	—	426	426	426
γ_0	—	—	1.17	1.17	1.17
q	—	—	0.5	0.5	0.5
Reduced χ^2	0.70 ± 0.23	1.37 ± 0.37	—	—	—

[a] γ_0 and q taken from previously reported values for Mw94 (Wicks et al. 2015). [b] Identical to Mw94 model except for V_0 taken from Wicks et al. (2017). [c] Non-thermal parameters from Finkelstein et al. (2017).

range of seismic observations. In order to do so, we first constructed a forward linear mixing model for calculating the sound velocities and densities of mineral aggregates containing iron-rich (Mg,Fe)O mixed with bridgmanite (Br) and calcium silicate perovskite (CaPv). The iron content of Br was determined by the partitioning of iron between Mw and Br using a K_D value of 0.03 (Wicks et al., 2017). For CaPv, we used recent ultrasonic interferometry experiments reported by Gréaux et al. (2019) and extrapolated to CMB conditions using finite strain analysis (Duffy & Anderson, 1989). For modeling Br properties, we used a combination of theoretical and experimental constraints (e.g., Dorfman et al., 2013; B. Li and Zhang, 2005; Wentzcovitch et al., 2010; Wolf et al., 2015) (see Table A.3). We calculated properties for aggregates containing concentrations of Mw ranging from 0% to 50% combined with a mixture of Br and CaPv where the concentration of CaPv was controlled by fixing it at 10% of Br concentration, with an uncertainty of 5%. By computing bulk and shear moduli for the minerals we were mixing, we could compute Voigt and Reuss bounds for the aggregate elastic properties in order to determine the range of velocity reductions that can be accounted for by the presence of iron-rich (Mg,Fe)O. The Hill averages for P and S wave velocity reductions relative to PREM for aggregates containing Mw94, Mw84, and Mw78 are shown in Figure 2.2, as well as markers indicating density increases relative to PREM. Voigt and Reuss bounds for all three compositions of Mw are shown in Figure A.4, with markers indicating Mw concentrations.

2.4.3 Inverse Modeling

While the forward model demonstrates that a wide array of observed velocity reductions could be caused by the presence of iron-rich (Mg,Fe)O, it does not offer a direct quantitative assessment of the compatibility of ULVZ observations with hypothetical mineral aggregates bearing iron-rich (Mg,Fe)O. To that end, we additionally constructed an inverse linear mixing model that can more comprehensively compare seismic observations with experimental results from mineral physics. The inputs to the inverse model were the bulk and shear moduli and density (computed from reported seismic velocities and density) of an observed ULVZ with estimated uncertainties, as well as these properties for the minerals that were being mixed (e.g., Mw94 + Br32 + CaPv, where Br32 represents $(Mg_{0.68}Fe_{0.32})SiO_3$), with errors propagated from the relevant experimental results. The model minimizes the difference between the target assemblage elastic properties and the hypothetical assemblage properties, with properties weighted according to the inverse of their observational and experimental uncertainties during the fitting procedure. In this way, the model computes individual mineral concentrations for the assemblage that best fits the observational target, following either the Voigt or Reuss formulation of aggregate mixing. Thus, for a given ULVZ observation, we can compute the concentration (X, in percent) of an iron-rich composition of (Mg,Fe)O for the aggregate that would provide the closest fit of seismic wave velocities and density to the observation. The uncertainty in the resulting (Mg,Fe)O concentration includes uncertainty estimates from both the seismic observation of the ULVZ and from the elastic properties of the constituent minerals. By using the χ^2 value to evaluate the quality of the fit, we can compare best-fit assemblages of various mineral compositions to determine which set of minerals with which set of concentrations can best explain a ULVZ observation. More details of the inverse modeling approach can be found in Appendix A.

In order to demonstrate the applicability of this approach, we evaluated two ULVZ seismic observations chosen specifically because the studies report constraints on both V_P and V_S, as well as density and estimates of uncertainties (Table 2.2). For the inversions, we report the best-fit assemblages containing magnesiowüstite compositions that result in the lowest χ^2 values (Table 2.2). As part of the inversion process, we can use priors on mineral concentrations to test whether these observed ULVZ properties are compatible with an iron-enriched pyrolitic composition, or whether a non-pyrolitic composition is required to explain the observation. We additionally make use of priors to account for the tradeoffs in concentration

between Br and CaPv, which exhibit velocities much closer to PREM than Mw. To that end, for the ULVZ underneath the South Atlantic (Simmons & Grand, 2002), we impose a prior on the Br concentration of 0.7 with a prior window of 0.2, both due to the trade-off with CaPv and in order to maintain pyrolitic proportions, while for the Mw78 inversion a wider prior window of 0.4 can be used to produce reasonable results. The results demonstrate that an iron-enriched pyrolitic composition is compatible with the South Atlantic ULVZ observation. In contrast, the inversion for the selected seismic observation of a ULVZ beneath the Coral Sea (Rost et al., 2006) requires more magnesiowüstite than a pyrolitic model would suggest, necessitating a different set of priors. These results suggest that two different formation scenarios may be required for these two ULVZ observations.

Table 2.2: Isothermal equation of state parameters for the B1 and rhombohedral phases of Mw94, with thermal equation of state models for three iron-rich compositions of Mw.

Result	δV_P (%)[a]	δV_S (%)	$\delta\rho$ (%)	Mw#	X_{Mw} (%)	X_{Br} (%)	X_{CaPv} (%)	Reduced χ^2
ULVZ: S. Atlantic[b]	−3 ± 3	−9 ± 3	+10 ± 10					
Fit: Voigt	−8.3 ± 3.4	−10.2 ± 3.9	+17.2 ± 2.6	94	29.0 ± 11	59.9 ± 13	11.1	0.58 ± 0.54
Reuss	−4.4 ± 2.3	−8.3 ± 2.0	+8.2 ± 0.6	94	11.6 ± 1.8	72.1 ± 5.6	16.3	0.09 ± 0.21
Hill	−6.4 ± 2.1	−9.3 ± 1.7	+12.7 ± 2.2	94	20.3 ± 5.6	66.0 ± 7.1	13.7	
Fit: Voigt	−7.7 ± 2.9	−10.0 ± 3.1	+15.3 ± 1.7	84	34.1 ± 8.6	64.5 ± 9.9	1.4	0.32 ± 0.40
Reuss	−1.6 ± 2.6	−6.1 ± 2.6	+2.4 ± 0.6	84	11.4 ± 2.7	73.0 ± 9.2	15.6	0.22 ± 0.33
Hill	−5.3 ± 1.9	−8.5 ± 2.0	+9.7 ± 0.9	84	22.7 ± 4.5	68.7 ± 6.7	8.6	
Fit: Voigt[c]	−6.6 ± 2.6%	−9.7 ± 2.7	+12.8 ± 1.3	78	34.4 ± 7.7	63 ± 11	2.6	0.15 ± 0.27
Reuss[c]	−1.4 ± 2.9	−6.3 ± 2.6	+2.8 ± 0.7	78	11.8 ± 4.1	80 ± 19	8.2	0.28 ± 0.37
Hill	−4.1 ± 1.9	−8.0 ± 1.9	+7.8 ± 0.8	78	23.1 ± 4.4	71 ± 11	5.9	
ULVZ: Coral Sea [d]	−8 ± 3	−24 ± 4	+8 ± 6					
Fit: Voigt [e]	−11.9 ± 3.6	−17.9 ± 5.2	+18.3 ± 2.4	78	46.7 ± 14	48.4 ± 17	4.9	3.5 ± 1.1
Reuss [e]	−12.6 ± 2.1	−25.9 ± 2.4	+12.7 ± 1.5	78	34.1 ± 4.0	61.1 ± 6.3	7.9	0.41 ± 0.37
Hill	−12.2 ± 2.1	−21.7 ± 3.0	+15.5 ± 1.3	78	40.4 ± 7.3	54.7 ± 9.1	4.9	

Note: Uncertainties are reported at the 68% level. Unless otherwise noted, all inversions use a prior of $X_{Br} = 0.7$ with a window of 0.2. [a] Velocity and density changes are reported as a percentage relative to PREM at the CMB. [b] Simmons & Grand (2002). [c] Prior: $X_{Br} = 0.7$ with a window of 0.4. [d] Rost et al. (2006). [e] Priors: $X_{Br} = 0.6$ and $X_{Mw} = 0.4$, with windows of 0.1 for each.

The modeling results shown in Figure 2.2 demonstrate that the presence of iron-rich (Mg,Fe)O results in velocity reductions relative to PREM close to the 1:2 δV_P:δV_S ratio. It can additionally be seen that the inversion results suggest that ULVZ observations exhibiting a 1:3 V_P:V_S reduction ratio can also be explained by the presence of iron-rich (Mg,Fe)O, within the estimated uncertainty bounds. To help clarify this result, the vertical bars on the forward models (Figures 2.2a and A.4) demonstrate the wide range of reduction ratios, particularly at low S-wave speed reductions, that can be produced by the presence of Mw within uncertainty

bounds. It is additionally worth noting that the aggregate elastic properties of the inverted ULVZs could in fact be closer to the Reuss or Voigt bounds than the Hill average, depending on the microstructure of the mineral phases. While the observed 1:3 V_P:V_S reduction ratio is commonly attributed to the presence of partial melt (e.g., Simmons and Grand, 2002; Yuan and Romanowicz, 2017), the compatibility of solid iron-enriched magnesiowüstite with this reduction ratio, as demonstrated by our results, underscores the necessity of applying a quantitative approach to evaluating ULVZ hypotheses. By using an inverse linear mixing model, we have shown that the presence of iron-rich (Mg,Fe)O is a viable hypothesis for explaining the seismic anomalies observed within certain ULVZs. The strength of our approach lies in the fact that it incorporates estimated uncertainties from both seismic observations and results from mineral physics, thus permitting a synthesis of information from both fields of study in a quantitative way. We have therefore contributed to the development of a framework for evaluating the likelihood of proposed hypotheses for ULVZs that can be expanded and applied in a systematic way to the growing set of ULVZ observations, in order to develop a comprehensive understanding of heterogeneities in the lowermost mantle.

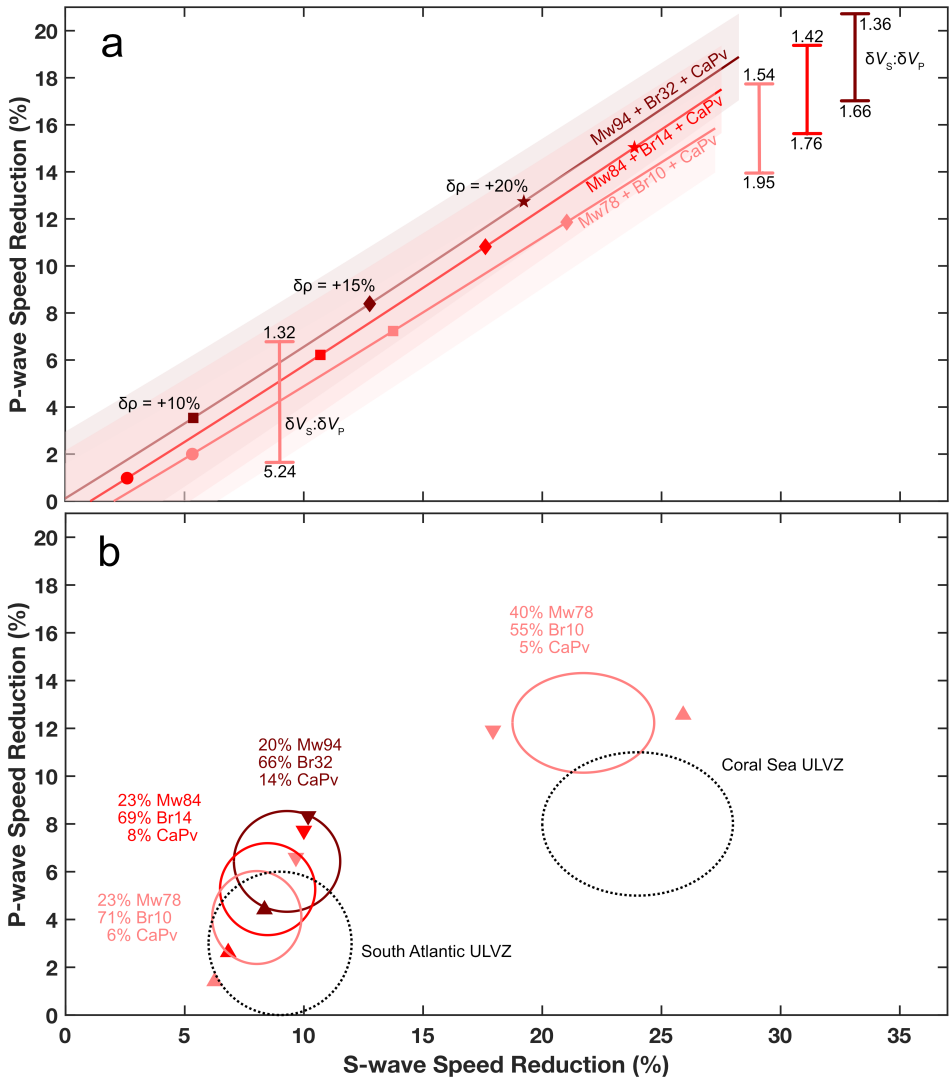

Figure 2.2: Seismic signatures of iron-rich (Mg,Fe)O in the lowermost mantle relative to PREM (Dziewonski & Anderson, 1981). (a) Forward models (Hill average) of three Mw compositions with Mw concentrations ranging from 8.3% (Mw94), 10.2% (Mw84), and 10.6% (Mw78) up to 50%, mixed with bridgmanite and calcium perovskite at a constant Br:CaPv ratio of 10:1. Symbols indicate density increases relative to PREM (circle 5%, square 10%, diamond 15%, star 20%). Vertical bars indicate the range of $\delta V_P : \delta V_S$ for a given Mw composition at a given δV_S. (b) Best-fit results of the inverse model for two ULVZ observations: South Atlantic (Simmons & Grand, 2002) and Coral Sea (Rost et al., 2006). Ellipses represent uncertainties for observations (black dotted lines) and uncertainties at the 68% level for Hill average of best-fit Mw-containing assemblages (solid lines), with corresponding concentrations and compositions noted. Downward and upward triangles indicate best-fit assemblage properties for Voigt and Reuss mixing bounds, respectively. The complete inversion results, including the Voigt and Reuss bounds, are reported in Table 2.2 .

Chapter 3

INTERDISCIPLINARY APPROACHES FOR QUANTIFYING COMPOSITIONS OF ULTRALOW VELOCITY ZONES: CASE STUDY OF A REGION UNDERNEATH HAWAI'I

**This chapter has been previously published as part of*

Lai, V. H., Helmberger, D. V., Dobrosavljevic, V. V., Wu, W., Sun, D., Jackson, J. M., & Gurnis, M. (2022). Strong ULVZ and Slab Interaction at the Northeastern Edge of the Pacific LLSVP Favors Plume Generation. *Geochemistry, Geophysics, Geosystems, 23*(2). doi.org/10.1029/2021GC010020.

In this chapter, I include excerpts from the published study that describe my contributions (Sections 2-3), as well as the study's published introduction (Section 1) and a published figure showing seismic modeling results (Figure 3.2) to provide context for the mineralogical modeling.

3.1 Introduction

The northeastern margin of the Pacific Large Low Shear Velocity Province (LLSVP) is particularly interesting as many seismic modelling studies have suggested the presence of multiple structural anomalies in this lowermost mantle region. There is a strong velocity change from the interior of the Pacific LLSVP towards the margin, inferred to be a high velocity, post-perovskite lens thins towards the edge while an ultra-low velocity zone (ULVZ) layer increases in thickness (Lay et al., 2006). To et al. (2011) also proposed a localized, slow ULVZ-like anomaly embedded inside or at the margin of the LLSVP from their modeling of the anomalous S and diffracted S (Sdiff) behaviors observed with a limited number of stations.

The deployment of USArray, recording many deep earthquakes from Fiji-Tonga subduction zone, greatly increases the sampling points to study the lateral structural variation along this margin. Through deconvolution and stacking of short period ScS pre- and post-cursor energies, C. Zhao et al. (2017) proposed this region hosts several clusters of ULVZs with non-uniform thicknesses (<5 to 20 km) and with a strong velocity reduction (30%) (Fig. 3.1; Group 1). The ULVZ cluster is modelled to be the thickest inside the LLSVP and becomes thinner towards the edge of the LLSVP. Apart from the lateral variation in ULVZ thicknesses, the region towards the

edge is thought to be more complex with layers of fast and slow velocity compared to the region with the thickest ULVZ. Jenkins et al. (2021) further expanded on the ScS pre- and post-cursors study by C. Zhao et al. (2017) and suggested an asymmetric ULVZ ridge, increasing in thickness towards northeast along this margin. D. Sun et al. (2019) also showed there are strong multipathing of ScS at two distinct patches along this boundary for several earthquakes. The northern patch (Fig. 3.1, Box 2) is modeled extensively as a ULVZ structure in D. Sun et al. (2019) and Jenkins et al. (2021).

This location with a strong presence of structural anomalies is geodynamically interesting as it coincides with the proposed plume location rooted within the deep mantle that gives rise to the Hawai‘i-Emperor seamount chain (Hassan et al., 2016). Geodynamical modeling has attempted to track the evolution of the plume location which needs to fit several features of the Hawai‘i-Emperor seamount chain, including a relatively sharp bend at 47 Ma, a rapid change in migration rate of volcanic islands, and the formation of individual volcanoes at different paleolatitudes (Tarduno et al., 2009). Although global mantle flow could distort upwelling plumes and may explain the observed hotspot motion (Steinberger et al., 2004), Hassan et al. (2016) argued that the sharp bend and migration rate in Hawai‘ian hotspot can be partly explained by the migration of the plume source along the core-mantle boundary (CMB). Their mantle flow model showed that the strong and persistent subduction in the north Pacific can influence deep mantle flow, deform the Pacific Large Low Shear Velocity Province (LLSVP), and cause the southward migration of the Hawai‘ian plume to its current location at the northeastern edge of the Pacific LLSVP about 12°southeast of Hawai‘i (Fig. 3.1, Box 3). However, global tomographic models (e.g., French and Romanowicz, 2015; D. Zhao, 2004) prefer broad vertical plume-like structure directly beneath the Hawai‘ian hotspot. This apparent mismatch between geodynamical and seismological results warrants new ways to image and model the plume.

Most seismic studies focus on a single wave type, either core-reflected phases (e.g., ScS), core waves (e.g., SPdKS+SKPdS) or diffracted energy (e.g., Sdiff), which samples the CMB differently. Furthermore, these studies use 1-D waveform modeling to attribute observed waveform anomalies to a single type of structure, e.g., a ULVZ, and cannot model waveform interaction due to lateral variation of structural anomalies. However, He and Wen (2012) alluded to a complex interaction of slow and fast structures across the LLSVP margin. In this study, we combine

multiple wave types (S, ScS, and Sdiff) covering a wide distance range (75°to 105°) and present seismic evidence for a strong lateral structural variation across the north-eastern edge of Pacific LLSVP, particularly along an azimuth corridor centered at 50°(Fig. 3.1). Based on 2-D waveform-modeling, we hypothesize this rapid variation reflects a complex interaction between a ULVZ in the inner edge of the Pacific LLSVP being impinged by a subducted slab at the outer edge, which can potentially give rise to a plume. In the discussion, we present a solid-state compositional model containing iron-rich (Mg,Fe)O magnesiowüstite that can explain the observed ULVZ properties and address the trade-off between the ULVZ velocity reduction and thickness. The resulting possibility of highly conductive interconnected magnesiowüstite could provide a mechanism for increased bulk thermal conductivity and enhanced plume generation. Finally, we discuss the potential of using vertically-incident ScS and its limitation to image the Hawai‘ian plume.

3.2 Mineralogy of ULVZ

The existence of the ULVZ structure could arise through several scenarios such as (1) the partial melting of ambient mantle or subducted slab materials (J. Liu et al., 2016; Pradhan et al., 2015; Thorne et al., 2019), and/or (2) a solid-state assemblage containing iron-enriched (Mg,Fe)O magnesiowüstite (Bower et al., 2011; Finkelstein et al., 2018; Wicks et al., 2017) that may be produced by chemical interaction with the core or magma ocean solidification (Labrosse et al., 2007). Recent work has demonstrated that the modeled seismic properties of various ULVZs are compatible with a solid magnesiowüstite-bearing assemblage (Dobrosavljevic et al., 2019; Jackson & Thomas, 2021). Here, we tested the solid magnesiowüstite hypothesis for the ULVZ detected in this study with the following steps: (1) construct forward models of magnesiowüstite-bearing assemblages to calculate bulk densities of assemblages that can reproduce the observed velocity reductions, given tradeoffs in thickness and velocity reduction in the seismic models; (2) compare resulting assemblage densities for each thickness-velocity reduction combination against geodynamic simulations of thickness dependence on density for solid ULVZs; and (3) invert for best-fit mineralogy for the preferred seismic model to determine the error correlations on compositions and bulk properties.

We first calculated forward models of the proposed mineralogies for two different magnesiowüstite compositions – $(Mg_{0.06}Fe_{0.94})O$ (hereafter Mw94) and $(Mg_{0.22}Fe_{0.78})O$ (hereafter Mw78) – shown in Figure 3.3a, using elastic properties calculated at CMB conditions for iron-rich (Mg,Fe)O magnesiowüstite with coexisting $(Mg,Fe)SiO_3$

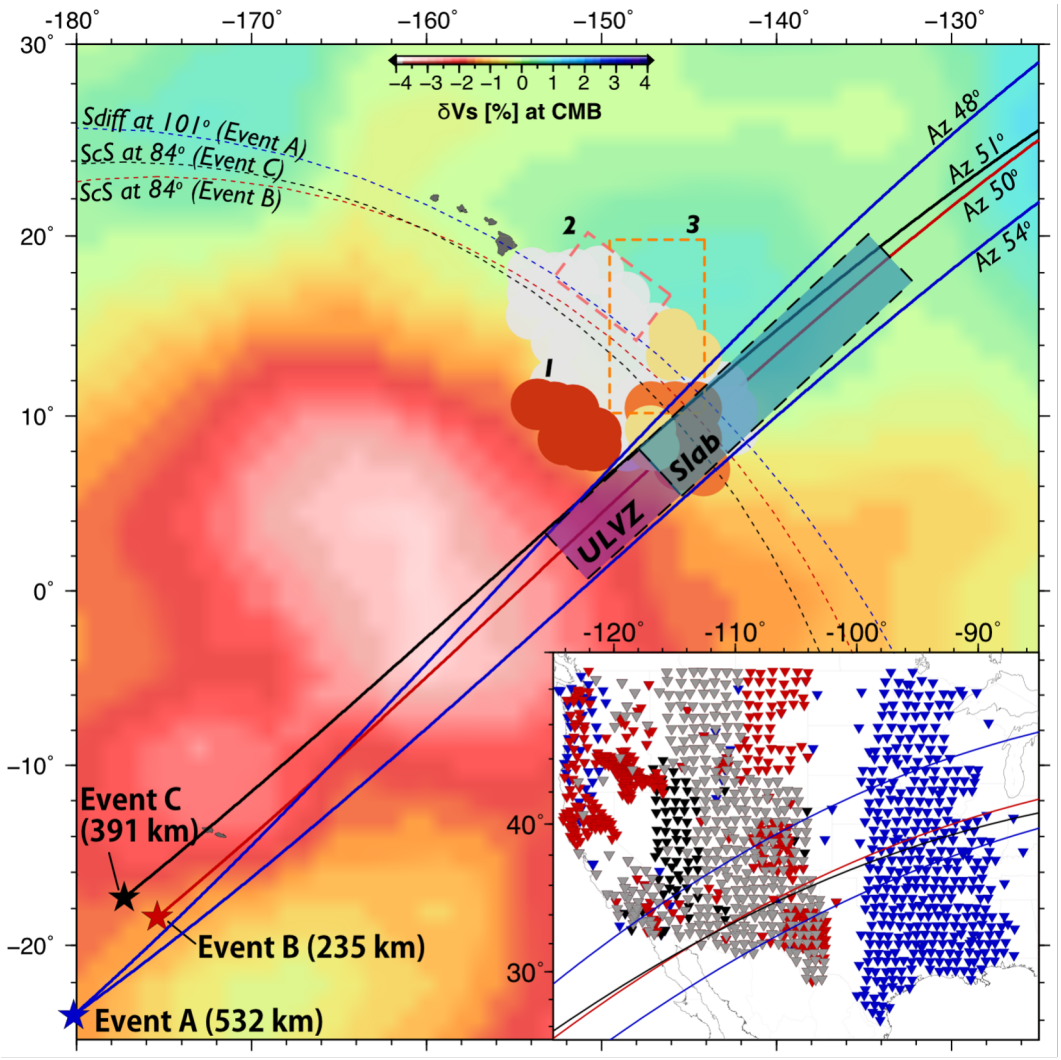

Figure 3.1: Location of the proposed ULVZ-slab structure near the northeastern edge of Pacific LLSVP. Map shows the location of the three deep Fiji events, which are Event A (2011-07-29 Mw6.7 at 532 km depth), Event B (2008-10-22 Mw6.4 at 235 km depth), and Event C (2008-07-19 Mw6.4 at 391 km depth). The background is shear wave perturbation from GyPSuM model (Simmons et al., 2010) at the core-mantle boundary. The inset shows the stations used in this study, color-coded by events. Stations used for both Event B and C are colored in grey. The color-coded thick lines in the main map and inset show the ray paths sampling the northeastern edge of the Pacific LLSVP, the Sdiff pierce point for Event A at a distance of 101°, and the ScS bounce points for Events B and C at a distance of 84°, estimated using a 1-D IASP model. Group 1 shows the thickness distribution of ULVZ identified in Zhao et al. (2017; Fig. 13) where the patches in grey, yellow, orange, and red represent a thickness of <5, 10, 14 and 20 km, respectively. Box 2 marks the location of ULVZ proposed by D. Sun et al. (2019). Box 3 is the estimated location of present-day plume by Hassan et al. (2016)at the core-mantle boundary.

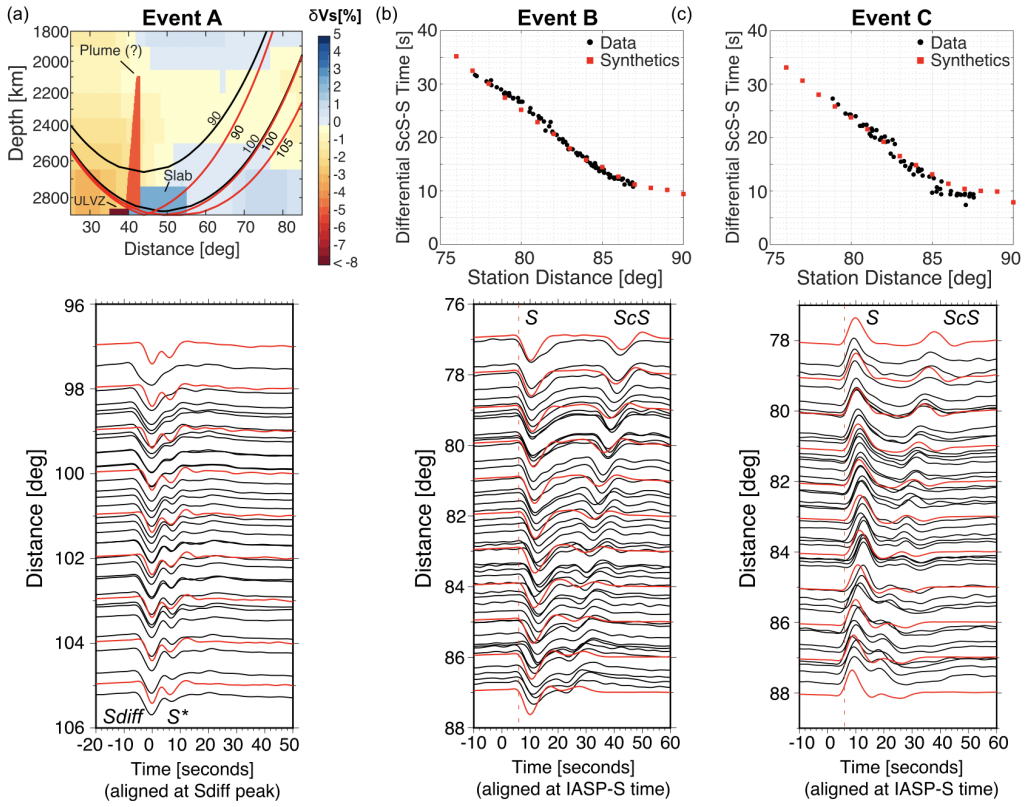

Figure 3.2: Modeling results for Event A, B and C. (a) Cross-section of the model: GyPSuM embedded with a ULVZ (30 km thick; 5°wide; δV_S = -18%), a slab (150 km thick; 15°wide; δV_S = +2.5%) , and a possible plume structure (800 km tall; 4°wide at the bottom; 1°wide at the top, δV_S = -5%). The 1-D approximate ray paths of ScS, S and Sdiff for Event A are plotted. The record section at the bottom shows the fit of S* between the synthetics (red) and the data (black) for Event A. (b+c) Top graph shows the comparison of differential ScS-S time at azimuth 49 – 51°measured from synthetics (red) and data (black) for (b) Event B at azimuth 49 – 51°and (c) Event C at azimuth 50 – 52°. Bottom plot shows the waveform comparison of S and ScS between synthetics (red) and data (black). The waveforms are aligned at the expected S arrival time based on the 1-D IASP reference model.

bridgmanite and $CaSiO_3$ calcium silicate perovskite (see Table B.1 and Fig. B.1; Dobrosavljevic et al., 2019). We varied the concentration of magnesiowüstite mixed with a constant 15:85 ratio of $CaSiO_3$ to bridgmanite. To account for uncertainty in stress distribution among the constituent phases, we calculate models using two endmember phase mixing cases – Voigt averaging (uniform strain distribution) and Reuss averaging (uniform stress distribution) (Watt et al., 1976). Because the elastic moduli of magnesiowüstite are much smaller than those of the other two constituent phases, the two mixing bounds exhibit large differences in bulk assemblage properties for a given magnesiowüstite concentration or a given bulk velocity reduction (Fig. 3.3a, Fig. B.2).

As shown in Fig. 3.3, we used the forward models to calculate bulk densities of Mw78-bearing assemblages that reproduce the best-fitting velocity reduction constrained for each thickness-velocity reduction combination in the seismic modeling, for both the Voigt and Reuss bounds, as well as for Mw94 in the case of the 30 km model. By doing so, we investigate how tradeoffs in the seismic modeling of ULVZ properties can lead to a range of possible mineralogies and ULVZ densities. Resulting density uncertainties (Fig. 3.3b) are propagated from uncertainties in the seismic velocity reduction (estimated at 3%) and uncertainties in the mineral densities (<1%). The dominant source of uncertainty in these mineralogical models comes from whether the assemblage is under conditions that are closer to the Voigt or Reuss bound. Given the very low elastic moduli of magnesiowüstite and its very low viscosity (Reali et al., 2019), these assemblages may be closer to the Reuss bound, which exactly describes the effective moduli of solid grains suspended in a fluid with zero shear modulus (Mavko et al., 2010). However, due to a lack of experimental data on the elastic and rheological properties of such iron-rich assemblages at lower mantle conditions, we consider both the Voigt and Reuss bounds in our analysis.

Next, we investigated whether the calculated mineral assemblage densities for each possible ULVZ thickness are compatible with geodynamic simulations that constrain thickness dependence on density for solid-state ULVZs (Bower et al., 2011). In these geodynamic simulations, a steady-state ULVZ morphology is derived from an initial chemically distinct dense layer between 4 km and 16 km thickness (see Fig. B.3). Given the potential dynamic complexity in this study region, we note that the result from modeling the ULVZ as steady state in the absence of dynamic upwelling or downwelling is an approximation. The ULVZ thickness (Fig.

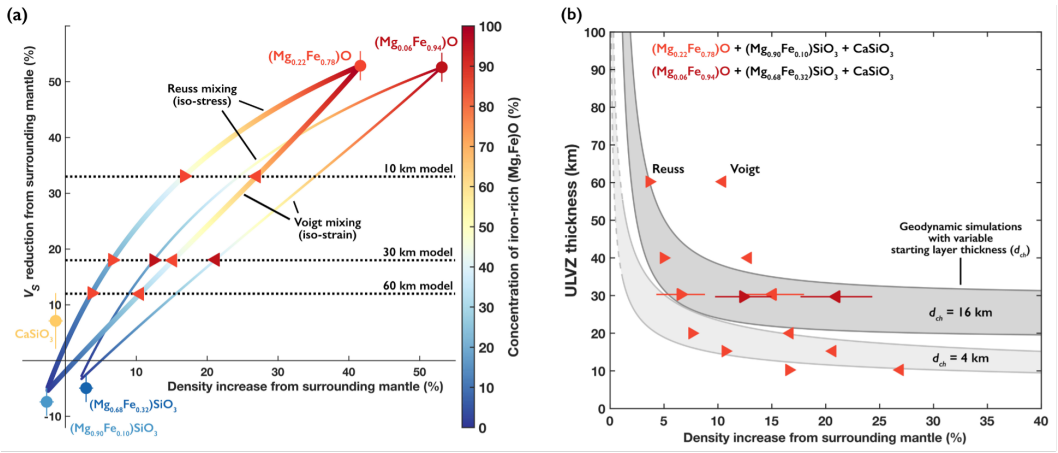

Figure 3.3: Mineralogical models of solid ULVZs containing iron-rich magnesiowüstite. (a) Forward models of velocity reductions relative to IASP at the CMB and density increases relative to PREM at the CMB for solid assemblages containing varying amounts of iron-rich (Mg,Fe)O magnesiowüstite mixed with (Mg,Fe)SiO_3 bridgmanite and $CaSiO_3$ at a constant ratio of 85:15. Thicker lines show $(Mg_{0.22}Fe_{0.78})O$ (Mw78) + $(Mg_{0.90}Fe_{0.10})SiO_3$ + $CaSiO_3$ and thinner lines show $(Mg_{0.06}Fe_{0.94})O$ (Mw94) + $(Mg_{0.68}Fe_{0.32})SiO_3$ + $CaSiO_3$. Assemblage properties are calculated for both Voigt (iso-strain) and Reuss (iso-stress) endmember mixing bounds. Dotted black lines indicate velocity reductions constrained by seismic modeling for different possible ULVZ thicknesses. Rightward (Reuss) and leftward (Voigt) triangles show resulting densities for assemblages that reproduce velocity reductions in each seismic model for Mw78 (light red) and Mw94 (dark red) bearing assemblages. Full phase elasticity information is given in Table B.1. (b) Densities for assemblages that reproduce seismically modeled velocity reductions at each ULVZ height for Reuss (right triangle) and Voigt (left triangle) mixing and for Mw78 (light red) and Mw94 (dark red) bearing assemblages. Shaded regions indicate equilibrium thickness of solid ULVZs modeled by geodynamic simulations (Fig. S12) as a function of ULVZ density, given a starting chemically distinct layer of thickness 4 km (light gray) and 16 km (dark gray).

3.3b) depends on the density of the chemically distinct ULVZ material, modeled as an assemblage containing low magnesiowüstite (Reali et al., 2019). This analysis shows that the taller ULVZ seismic models are compatible only in the case of Reuss mixing. ULVZ models thinner than 20 km are also compatible with geodynamic simulations in the case of a thinner starting chemical layer. However, these models are less preferable as they generate additional weak ripple-like arrivals after the S* pulse that are not observed (Lai et al., 2022). The 30 km model is preferred as it can be explained by a solid magnesiowüstite-bearing ULVZ for both cases of Voigt and Reuss mixing and for both Mw78 and Mw94 compositions.

Finally, using best-fit minimization, we inverted for assemblage compositions most compatible with the preferred seismic model (30 km thickness, -18% δV_S) and examined the error correlations for the modeled mineralogy (see Dobrosavljevic et al. (2019) for details of the inversion method). The inversions incorporate uncertainties from mineral physics on phase elasticity (Table B.1) as well as uncertainties on seismic velocity (estimated at 3%). As this study only constrains δV_S values for the ULVZ, we estimate density and δV_P values from the forward models for use in the inversion and assign a larger 5% uncertainty. Inversion results for Mw78 and Mw94-bearing assemblages are shown in Fig. 3.4 and Table B.2, with ellipses representing correlated uncertainties at the 1σ level for Voigt (dashed lines) and Reuss (solid lines) mixing. The concentration of magnesiowüstite is relatively tightly constrained (1-2% uncertainty), while the concentration of bridgmanite shows more uncertainty and tradeoff with the concentration of $CaSiO_3$ (Fig. 3.4a). Even for the most iron-rich assemblage (Mw94 Voigt) constrained in this analysis (Table B.2), an initial 16 km chemical layer at the CMB would produce no more than a 0.1 wt% increase in the total FeO content of the whole mantle, well within the uncertainty of the previously estimated bulk silicate earth value of 7.97 ± 0.54 wt% (Lyubetskaya & Korenaga, 2007), based on a statistical analysis. By considering the error correlations in the resulting seismic velocities of the assemblages (Fig. 3.4b), we showed that such solid magnesiowüstite-bearing assemblages can produce a range of δV_S:δV_P ratios, from 1.2 up to the 3 ratio level commonly attributed to the presence of partial melt (Berryman, 2000).

3.3 Conclusion

In short, we constructed a mineralogical model for the observed ULVZ containing solid iron-rich (Mg,Fe)O magnesiowüstite. This model is consistent with three independent constraints: (1) the seismically modeled δV_S and thickness of the ULVZ, (2) phase elasticities and viscosities from mineral physics, and (3) ULVZ morphologies from geodynamic simulations. These results together provide strong quantitative support for a solid-state magnesiowüstite-bearing ULVZ interpretation and show that partial melt is not necessary to produce the observed ULVZ properties. A possible partial melt origin is not assessed nor ruled out in this analysis but may face challenges from recent geodynamic simulations (Dannberg et al., 2021) and a lack of *in-situ* experimental data on the sound velocities of partially molten assemblages. Though the rheology of the modeled solid iron-rich phase assemblage is uncertain, recent findings have suggested the development of an interconnected

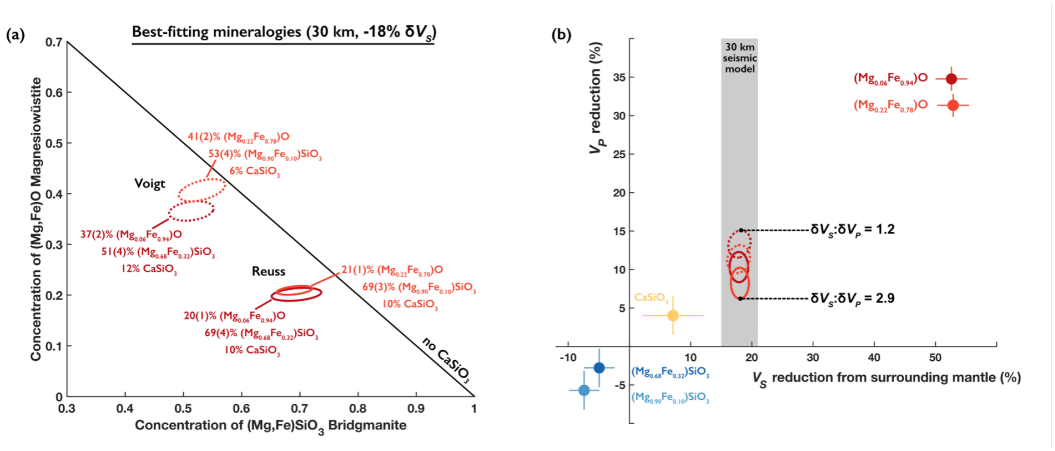

Figure 3.4: Best-fitting mineralogies for the preferred seismic ULVZ model. (a) Composition results from inversions for best-fitting mineralogical assemblages containing $(Mg_{0.22}Fe_{0.78})O$ (Mw78) (light red) and $(Mg_{0.06}Fe_{0.94})O$ (Mw94) (dark red) mixed with coexisting bridgmanite and $CaSiO_3$, calculated for both Voigt (dotted lines) and Reuss (solid lines) bounds for the preferred seismic ULVZ model (30 km thickness, -18% δV_S). The diagonal black line represents cases where the concentration of $CaSiO_3$ is zero. For the region below the diagonal black line, the concentration of $CaSiO_3$ is 1 minus the sum of the concentrations of magnesiowüstite and bridgmanite. Labels indicate relative concentrations of constituent phases with uncertainties. Ellipses indicate correlations in the concentration uncertainties at the 1σ level. Full results are given in Table B.2. (b) Aggregate velocity reductions relative to IASP at the CMB for the best-fitting assemblages shown in (a). Gray shading indicates the velocity reduction of the preferred seismic model with 3% uncertainty. Correlated velocity reduction uncertainties for Voigt (dotted lines) and Reuss (solid lines) bounds for Mw78 (light red) and Mw94 (dark red) bearing assemblages span a range of δV_P values and produce δV_S:δV_P ratios from 1.2 up to the 3 ratio level commonly attributed to the presence of partial melt. .

weak layer (IWL) of iron-poor (Mg,Fe)O ferropericlase coexisting with bridgmanite at lower mantle conditions (Chandler et al., 2021). In comparison, iron-rich (Mg,Fe)O exhibits even lower viscosities (Reali et al., 2019), which may further promote IWL formation, as well as much higher conductivities (Ohta et al., 2014). The possibility of highly conductive, interconnected magnesiowüstite in the ULVZ could lead to an increased bulk thermal conductivity of the structure and contribute to enhanced plume generation.

Chapter 4

CONSTRAINING TEMPERATURES OF EARTH'S CORE: MELTING AND PHASE RELATIONS OF Fe-Ni-Si DETERMINED BY A MULTI-TECHNIQUE APPROACH

**This chapter has been previously published as*

Dobrosavljevic, V. V., Zhang, D., Sturhahn, W., Zhao, J., Toellner, T. S., Chariton, S., Prakapenka, V. B., Pardo, O. S., & Jackson, J. M. (2022). Melting and phase relations of Fe-Ni-Si determined by a multi-technique approach. *Earth and Planetary Science Letters, 584*, 117358. doi.org/10.1016/j.epsl.2021.117358

4.1 Introduction

The metallic cores of terrestrial planets in our solar system are suggested to be composed of iron alloyed with nickel (5wt%) and candidate light elements, based on cosmochemical studies, planetary accretion models, and seismological constraints in the case of the Earth (Hirose et al., 2013; McDonough & Sun, 1995; Sohl & Schubert, 2007). Constraints on temperature profiles and thermal evolution models of terrestrial planets (e.g., Knibbe and van Westrenen, 2018) have benefited from high-pressure experimental studies on the melting curves of iron and iron alloys (e.g., Anzellini et al., 2013; Morard et al., 2011; Sinmyo et al., 2019; D. Zhang et al., 2016). Accurate constraints on core temperatures are essential for understanding major processes like inner core crystallization (Labrosse et al., 2001), magnetic field generation (Olson, 2013), and heat flow through the core-mantle boundary (Lay et al., 2008), as well as the compositions, phase relations, and dynamics of complex multiscale structures in Earth's lowermost mantle (e.g., Dannberg et al., 2021; Dobrosavljevic et al., 2019; Jackson and Thomas, 2021; M. Li, 2020). The presence of moderate amounts of light elements such as Si, O, C, S, and H has consistently been shown to depress the melting temperatures of iron alloys, though their effects on the temperatures and shapes of melting curves remain challenging to constrain due to disagreements across the range of studies and experimental techniques (reviewed by Fischer, 2016).

Silicon has commonly been proposed as a candidate light element for several terrestrial planetary cores. Its suggested presence in Earth's core has been inferred

from its abundance in the silicate mantle, its solubility in liquid iron (Ozawa et al., 2009), and discrepancies between its isotopic composition in meteorites and the bulk silicate Earth (Hin et al., 2014; Shahar et al., 2009). Concentration estimates are generally placed between 1 to 11wt%Si (e.g., Javoy et al., 2010; Morrison et al., 2018; Ricolleau et al., 2011). In the case of Mercury's core, the presence of silicon has been inferred from analyses of magnetic field and surface chemistry data collected by the recent MESSENGER mission (Knibbe & van Westrenen, 2018; Steenstra & van Westrenen, 2020), with suggested concentrations ranging from 1 to 20wt%Si dependent on the presence of carbon or sulfur (Knibbe et al., 2021).

Very few studies, however, have investigated the combined effects of silicon and nickel on the high-pressure and temperature phase boundaries of iron. For the melting of Fe-Ni-Si, experimental studies are limited to one static compression study (Morard et al., 2011) and one shock compression study (Y. Zhang et al., 2018). The few melting studies on Fe-Si compositions without nickel show discrepant results, with some suggestion of elevated melting temperatures relative to iron, and are limited to relatively large Si concentrations (>9wt%) (Asanuma et al., 2010; Fischer et al., 2012; Fischer et al., 2013; Lord et al., 2010). Solid-solid phase boundaries, which also affect high-pressure melting and the location of solid-solid-liquid triple points, are dependent on Si concentration (Fischer et al., 2013; Wicks et al., 2018) and the presence of nickel (Torchio et al., 2020), further complicating interpretations of melting results. The only study on solid phase boundaries of Fe-Ni-Si measured a flattening of the *hcp-fcc* boundary relative to Fe that could not be predicted from separate measurements of Fe-Ni and Fe-Si (Komabayashi, Pesce, Sinmyo, et al., 2019).

In this work we develop a multi-technique approach for measuring the high-pressure melting and solid phase relations of iron alloys. We compress samples from an identical source in laser-heated diamond anvil cells using identical preparation procedures. Melting is detected with two independent *in-situ* atomic-level techniques: synchrotron Mössbauer spectroscopy (SMS), sensitive exclusively to the dynamics of solid-bound ^{57}Fe nuclei, and synchrotron x-ray diffraction (XRD), sensitive to the loss of long-range crystalline order due to melting. SMS measurements feature a high-frequency temperature readout system (D. Zhang et al., 2015) that monitors rapid temporal fluctuations to improve precision on temperature measurements. XRD measurements constrain the *hcp-fcc* phase boundary and thermal pressure evolution of the samples, and are conducted using a burst heating

with reference background updating method to quantify changes to the reference background during heating. We apply this multi-technique approach to studying the phase diagram of $Fe_{0.8}Ni_{0.1}Si_{0.1}$ (Fe-11wt%Ni-5.3wt%Si), a candidate composition for planetary cores that has been shown to satisfy seismic observational constraints of the density, bulk modulus, and bulk sound speed of Earth's outermost inner core (Morrison et al., 2018).

4.2 Methods

4.2.1 Sample preparation

Samples of $Fe_{0.8}Ni_{0.1}Si_{0.1}$, previously studied by Morrison et al. (2018), Morrison et al. (2019), were cut into rectangular sections with lateral dimensions of 30 to 100 μm and thickness of 10 μm and loaded in diamond anvil cells (DACs) with rhenium gaskets serving as sample chambers. Samples were sandwiched inside the sample chamber between flakes of dehydrated KCl with a minimum thickness of 10 μm that served as both thermal insulation and a pressure transmitting medium. At least one ruby sphere was loaded into the sample chamber without contact with the sample. Once loaded, each DAC was heated in a vacuum oven for 12 to 24 hours in order to minimize oxygen and moisture in the sample chamber, then subsequently sealed and compressed to its target pressure. Starting pressures were estimated from ruby fluorescence and measured by XRD (see Section 4.3.3). All samples for both sets of experiments were cut from the same bulk material and prepared using identical methods (see Text C.1 for further details).

4.2.2 Phase detection techniques

Synchrotron Mössbauer spectroscopy

Synchrotron Mössbauer spectroscopy (SMS) is a nuclear resonant forward scattering technique that involves the excitation of the first excited state of the ^{57}Fe nucleus, characterized by a transition energy of 14.4 keV and an excitation lifetime of 141 ns (Jackson et al., 2013; Sturhahn, 2000; Sturhahn, 2004). In the scattering process, most photons from the incident synchrotron x-ray beam are scattered by the sample's electrons in femtoseconds. Some photons, however, excite the ^{57}Fe nucleus and are re-emitted as the nucleus decays back to its ground state. A finite fraction of excitation events results in recoil-free absorption and emission of photons by the sample with no transfer of momentum between the photons and the iron nuclei, known as the Mössbauer effect. Nuclear resonant forward scattering is a coherent, elastic scattering process that is proportional to the Lamb-Mössbauer factor f_{LM} =

$e^{-k^2\langle u^2\rangle}$, where f_{LM} is the probability of recoil-free excitation events, k is the wavenumber of the incident photon (1.161×10^8 cm^{-1}), and $\langle u^2\rangle$ is the mean-square displacement of the nucleus. By measuring forward scattered, time-delayed photons, one can isolate the Mössbauer signal that originates exclusively from the solid-bound ^{57}Fe nuclei. The Mössbauer signal has been demonstrated to be an effective probe for detecting melting in Fe and Fe-Ni (Jackson et al., 2013; D. Zhang et al., 2016). As the sample is heated to its melting temperature, a loss of signal intensity indicates a loss of coherence in the scattering process, meaning that the iron atoms are no longer bound by the solid sample within the lifetime of the nuclear excitation. As the finite displacement of the solid-bound nucleus becomes very large upon melting, the measured signal and the Lamb-Mössbauer factor begin dropping off to zero, giving a signature of melting that can be fit with an experiment-specific scattering intensity model. The SMS technique thus directly probes the dynamic behavior of the iron atoms in order to detect melting. Because the Mössbauer signal originates exclusively from solid-bound iron nuclei, no other components in the sample assemblage or experimental setup contribute to the signal, resulting in negligible background and allowing for clear demarcation of the first onset of melt.

X-ray diffraction

Synchrotron X-ray diffraction (XRD) is an *in-situ* technique sensitive to atomic positions, with the electronic scattering process occurring at extremely fast timescales (on the order of 10^{-19} seconds). The presence of melt in the sample is revealed by the appearance of a diffuse scattering signal, originating from atomic disorder in the liquid state. This particular signal, termed liquid diffuse scattering, is characterized by a discontinuous increase in background intensity. The appearance of a liquid diffuse scattering signal has been used in previous studies for detecting melting at high pressures in iron and iron alloys (e.g., Anzellini et al., 2013; Boehler et al., 2008; Morard et al., 2011). XRD measurements additionally provide several other valuable pieces of information. Structural information is used to constrain the *hcp-fcc* phase boundary and monitor signals of chemical contamination. Unit-cell volumes measured at each temperature are used to calculate *in-situ* sample pressure evolution through the heating run using previously published thermal equations of state for the sample and the surrounding KCl, thus reducing a large source of uncertainty in constructing the phase boundaries at high-*P, T* conditions. Finally, changes in sample pressure during the XRD heating run can be fit and applied to the SMS measurements, where sample preparations are essentially identical but pre-melting

information on the sample's unit-cell volume (and thus pressure) is unavailable.

4.2.3 Experimental procedures

Synchrotron Mössbauer spectroscopy

The SMS experiments are conducted at beamline 3-ID-B of the Advanced Photon Source, which features resonant scattering techniques coupled with double-sided laser heating, the high-frequency FasTeR temperature measurement system (D. Zhang et al., 2015), conventional CCD-based upstream and downstream spectrometers, and x-ray diffraction (XRD). These experiments are conducted in top-up mode with 24 photon bunches separated by 153 ns. X-rays are prepared with a bandwidth of 1 meV at the 14.4125 keV nuclear resonance of ^{57}Fe using a silicon high-resolution monochromator (Toellner, 2000). The signal is recorded using an avalanche photodiode detector (APD) in forward scattering geometry. Ionization chambers are placed proximal to the DAC (upstream and downstream) to record fluctuations in the incident x-ray intensity and x-ray intensity absorption through the DAC assemblage, to monitor the thickness of the sample chamber during heating.

The shape and full-width half-maximum (FWHM ~16x16 μm^2) of the x-ray beam are measured by knife-edge scans using tungsten rods. Upstream and downstream cameras are optically aligned to the DAC position, while the DAC is aligned to the x-ray position using delay count intensities measured by horizontal and vertical scans of the sample chamber. Alignment of the laser hotspot (FWHM ~35x35 μm^2) and the x-ray beam are visually verified immediately before and after each heating run with cameras, and small changes in hotspot position due to thermal expansion of laser optics are monitored during heating runs and fit during data analysis (Section 4.3.2). XRD images are collected immediately before and after each heating run using a movable high resolution MAR345 image plate (Marresearch GmbH). Due to the meV bandwidth and the 14.4 keV incident energy, the exposure time required for a reasonable quality diffraction image is about 20 minutes. A CeO_2 standard is used to calibrate the sample and image plate geometry. Samples are initially heated to ~1500 K for at least 5 minutes in order to anneal the sample heating location and adjust the upstream and downstream laser powers to achieve similar CCD readout temperatures on both sides and a uniformly heated sample. A high-statistical quality SMS time spectrum is collected at the elevated annealing temperature in order to constrain a starting effective thickness of the sample heating location (D. Zhang et al., 2016). We refrained from collecting XRD images at high

temperatures due to requisite long XRD exposure times.

Each heating run consists of a computer-controlled acquisition sequence, in which every 3 seconds the laser power is ramped up incrementally and various parameters are recorded, including the laser power, the time-integrated Mössbauer signal intensity (delayed counts), x-ray intensities from the ionization chambers, and temperature readouts from the FasTeR system and CCD spectrometer. The FasTeR system measures the downstream sample temperature and is characterized by a high sampling frequency, recording ~300 samplings for every 3 second interval, while the CCD-based spectrometer measures the upstream and downstream temperatures and performs one measurement at the start of every 3 second interval. The total time for each heating run is around 2 to 4 minutes following the start of the acquisition sequence. Once the heating run is completed, laser power is quenched, and an SMS spectrum is collected, followed by an XRD image.

X-ray diffraction

The XRD experiments are conducted at beamline 13-ID-D of the Advanced Photon Source, using a Pilatus CdTe 1M x-ray detector and incident x-rays of energy 37 keV focused to a spot size of ~3x3 μm^2, measured by knife-edge scans using tungsten rods. A LaB6 standard is used to calibrate the sample and image plate geometry. Double-sided infrared lasers produce a flat-top heating spot with diameter ~10 μm (V. B. Prakapenka et al., 2008). Temperatures are measured on the upstream and downstream sides of the sample using a PIMAX 3 detector (Princeton Instruments) that records 1 to 10 measurements for every 4 second x-ray exposure window, with exposure time and measurement frequency adjusted for varying emission intensity. X-ray induced fluorescence on the sample is used to align the x-ray beam with the location of the laser heating spot and temperature measurements. Sample heating locations are annealed for at least 5 minutes at ~1500 K.

For most XRD measurements, we use a burst heating method that involves alternating pairs of high-temperature ("hot") and quenched ("cold") measurements. The laser power is set to an initial low power to begin each heating run at a sample temperature of 1200 K. Laser shutters open to heat the sample and a 4 second "hot" XRD collection is triggered. Laser shutters are then immediately closed to quench the sample, and an ambient temperature "cold" XRD measurement is immediately collected, also for 4 seconds. Once a measurement pair is recorded, the laser power is increased to the next step in order to target a higher temperature for the next XRD

measurement pair. Laser powers are adjusted to maintain upstream and downstream temperature balance and minimize axial thermal gradients in the sample. The total heating time for a single heating location is around 1 to 4 minutes, spread over the series of intermittent laser bursts. The short durations of continuous heating time in burst mode help to minimize hotspot drift and improve precision on x-ray and hotspot alignment. We additionally conduct two heating runs using a continuous heating method where laser power is manually increased during heating without intermittent quenching in an otherwise identical procedure that also uses 4 second XRD exposure times.

4.3 Results

4.3.1 Determination of the hcp-fcc phase boundary

X-ray diffraction images are integrated using the software DIOPTAS (Prescher & Prakapenka, 2015). All 300 K patterns confirm the presence of *hcp*-$Fe_{0.8}Ni_{0.1}Si_{0.1}$ and *B*2-KCl at ambient temperature, while high-temperature patterns reveal the transformation of the sample to *fcc* symmetry (Fig. 4.1a). Some ambient temperature patterns show remnant *fcc* reflections from crystal grains that do not transform back to the *hcp* phase during the rapid laser quench (Figs. 4.1b, 4.2c). The sluggish nature of this back-transformation has been previously observed for iron alloys (Komabayashi et al., 2012; Komabayashi, Pesce, Morard, et al., 2019). Additionally, some high-temperature patterns exhibit small remnant *hcp* peaks that persist after the bulk sample has transformed to the *fcc* phase, likely stemming from the radial tails of the x-ray beam that traverse colder parts of the sample. No other phases are identified from the patterns, suggesting no evidence of carbon contamination or other chemical reactions within detection limits. The temperatures used for further analysis of the high-temperature patterns are the mean of the upstream and downstream temperatures, with uncertainties represented by the standard error of the mean. The dependence of sample temperature on the incident laser power cannot be reliably used to identify the onset of melting in this study (see Text C.2, Fig. C.1).

For all heating runs, we observe smooth continuous diffraction rings for high temperature *hcp* reflections and spotty diffraction rings for high temperature *fcc* reflections, as well as for remnant *fcc* reflections in quenched measurements (Fig. 4.2b-c). We interpret these observations as the onset of grain growth (texture development) concurrent with the *hcp-fcc* transition. With subsequent heating at temperatures above the transition, we observe changes in diffraction spot positions

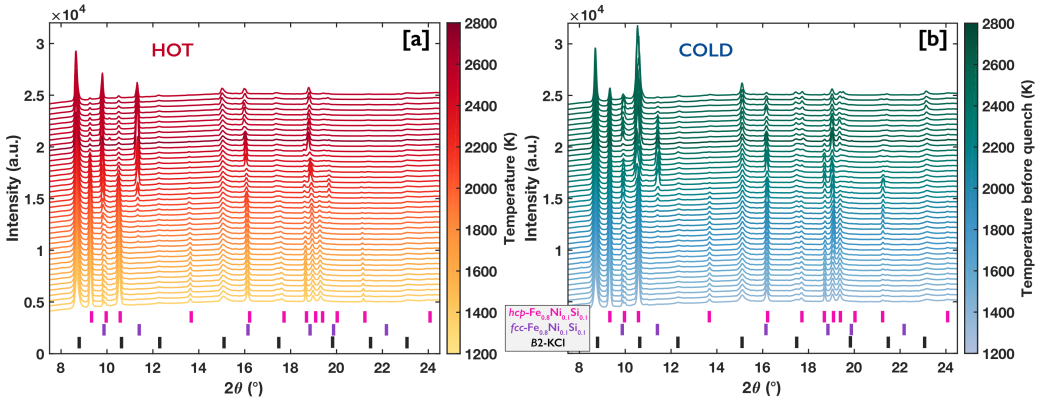

Figure 4.1: High temperature ("hot") [a] and quenched ("cold") [b] integrated XRD patterns from burst heating run D1P2S3 (49-56 GPa), color-coded by temperature. Colored ticks below patterns identify reflections from *hcp*-$Fe_{0.8}Ni_{0.1}Si_{0.1}$ (pink), *fcc*-$Fe_{0.8}Ni_{0.1}Si_{0.1}$ (purple), and KCl (black). The sluggish *fcc* to *hcp* back-reaction can result in reflections from remnant *fcc* grains in patterns quenched from temperatures above the *hcp-fcc* transition (see also Fig. 4.2).

and in *fcc* reflection intensities (Fig. 4.3) with each heating step and XRD measurement, which we interpret as recrystallization of the *fcc* phase at high temperatures. We observe similar behavior during burst heating mode in the quenched *hcp* reflections, which transition from continuous to spotty diffraction rings (grain growth) (Fig. 4.2d) at the *hcp-fcc* transition and similarly exhibit changes in diffraction spot positions (recrystallization) with subsequent heating steps.

We constrain the temperature of the *hcp-fcc* phase boundary using multiple non-overlapping sample reflections from the high-temperature XRD patterns, choosing two to five individual reflections from both phases for all heating runs (listed in Figs. 4.3, C.2-C.10). We integrate reflection intensities, subtract the integrated background intensity at each reflection, and normalize by the starting intensity. This procedure collapses all reflection intensities onto the same range of arbitrary intensity units, allowing for direct comparison and simultaneous fitting of all selected reflections for each phase. The loss of the *hcp* reflection intensities with increasing temperature is fit using a sigmoid function, whose finite width, generally ~400 K (Fig. 4.3, Figs. C.2-C.10), results from two phenomena. A coexistence region (~100-200 K) is expected for the *hcp* and *fcc* phases, as observed previously for iron-silicon alloys (e.g., Komabayashi, Pesce, Morard, et al., 2019). However, the likely presence of an axial temperature gradient in the sample (e.g., Sinmyo et al., 2019) could lead to overestimation of an *hcp*-out temperature, due to the

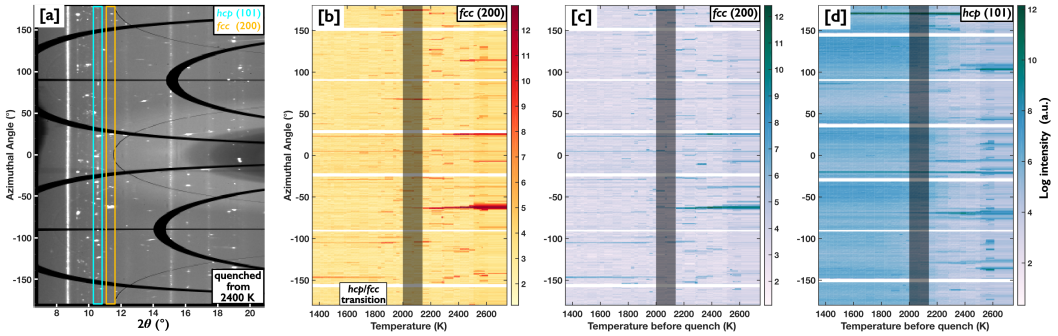

Figure 4.2: Evolution of sample grain growth and recrystallization (texture) during heating run D1P2S3 (49-56 GP). Panel [a] shows a raw 2D XRD image for a 300 K measurement quenched from 2400 K. Panels [b] and [c] show hot and cold azimuthal intensities of the *fcc* (200) reflection (yellow box in [a]) as a function of sample temperature and temperature before quench, respectively. Hot measurements ([b]) show grain growth and recrystallization of the *fcc* phase above the *hcp-fcc* transition (gray bar). Quenched measurements ([c]) capture "snapshots" of recrystallization effects due to the sluggish back transformation from *fcc* to *hcp* during rapid quench. Panel [d] shows 300 K intensities of the *hcp* (101) reflection (cyan bar in [a]). Texture of the quenched *hcp* phase evolves from fine-grained to coarse-grained as the sample is heated above the *hcp-fcc* transition.

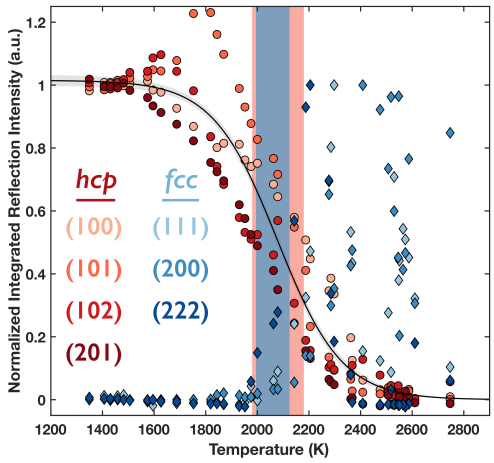

Figure 4.3: Changes in normalized integrated intensities from multiple *hcp*- and *fcc*-$Fe_{0.8}Ni_{0.1}Si_{0.1}$ reflections during heating run D1P2S3 (49-56 GPa). Transition temperature is calculated as an average of *hcp*-out (red bar) and *fcc*-in (blue bar) temperatures. Recrystallization of *fcc* grains (Fig. 4.2) produces fluctuations in *fcc* reflection intensities.

presence of the *hcp* phase in the cooler sample interior even as the hotter sample surface has fully transformed to the *fcc* phase. To account for these effects, we calculate the *hcp*-out temperature as the 50% intensity value from the sigmoid fit, with uncertainty estimated from the scatter of individual reflection intensities around the sigmoid fit. The onset of *fcc* reflections with increasing temperature is not fit due to significant scatter in intensities, resulting from recrystallization of the *fcc* phase. Instead, the *fcc*-in temperature is estimated at around 20% of the maximum intensities with reasonable uncertainty. The temperature of the phase boundary is calculated as an average of the *hcp*-out and *fcc*-in temperatures, with total uncertainty as the root-mean-square of the difference in these temperatures and their individual uncertainties.

4.3.2 Detection of melting

Synchrotron Mössbauer spectroscopy

Determining the melting temperature of $Fe_{0.8}Ni_{0.1}Si_{0.1}$ from SMS experiments involves fitting the intensity of the Mössbauer signal as a function of the sample temperature, calculated as an average of the upstream and downstream CCD temperatures. We additionally bin the high-frequency FasTeR temperatures to match the 3 second measurement intervals of the CCD temperatures and SMS intensities. The standard deviation of the FasTeR temperatures within each 3 second interval provides a higher temporal estimate of the sample temperature fluctuations (averaging around 30-50 K) than the CCD measurements. Temperature uncertainties are calculated as a quadrature sum of the upstream and downstream CCD temperature difference and the FasTeR temperature fluctuations. FasTeR temperatures show excellent agreement with the downstream CCD temperatures during all heating runs.

We use the CONUSS software package (Sturhahn, 2000) to fit the high-temperature SMS time spectrum collected before the start of the acquisition sequence in order to constrain the effective thickness of the sample at the start of the heating run (Fig. 4.4a). Effective thickness is dimensionless and is the product of the numerical density of the ^{57}Fe atoms, the physical thickness of the sample, the nuclear resonant cross-section (2.56×10^{-22} m^2 for ^{57}Fe), and the Lamb-Mössbauer factor (probability of recoil-free scattering events). We then calculate the Mössbauer signal intensity for each 3 second collection interval of the heating run (Fig. 4.4b) as the integral of delayed counts over the timing window. We normalize integrated counts by the x-ray intensity ratio measured by the upstream and down-

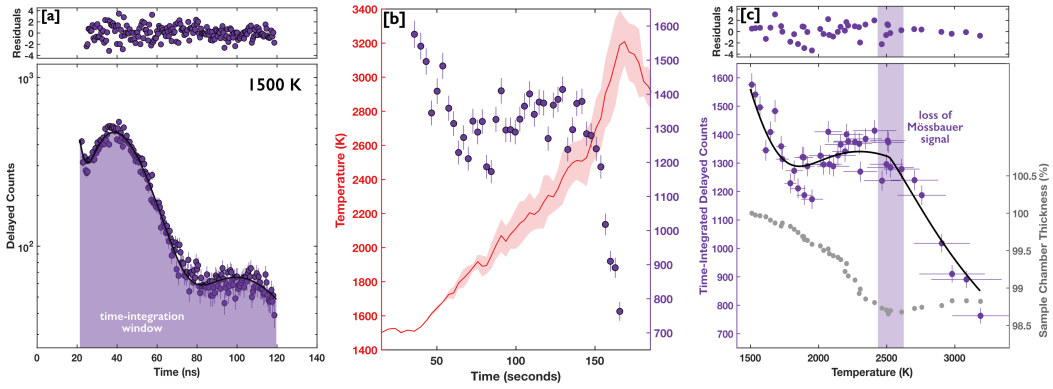

Figure 4.4: Typical SMS measurement of melting (heating run D1S1, 43-47 GPa). Panel [a]: High-statistical quality Mössbauer time spectrum is collected for ~5 minutes while annealing at ~1500 K. Spectra are fit with CONUSS (Sturhahn, 2000) to calculate the sample starting thickness. Panel [b]: Temperature (red line, left axis) and time-integrated delayed counts (purple shading in [a]) are collected over a series of 3-second intervals as laser power is gradually increased in an automatic acquisition sequence. Sudden drop-off in counts occurs at the onset of melting. Panel [c]: Scattering intensity model (solid black line) is fit to the count-temperature profile (purple points, left axis) in MINUTI (Sturhahn, 2021) to constrain the melting temperature (purple bar). Changes in sample chamber thickness (gray points, right axis) are calculated from total x-ray transmission intensity changes and are limited to less than 2% for all heating runs. Residuals from the fits are shown in units of standard deviation.

stream ionization chambers, in order to remove the effects of fluctuations in incident x-ray intensity and changes in the sample chamber thickness. Changes in the sample chamber thickness, as measured by the upstream and downstream ionization chambers, never exceed 2% for any heating runs (Figs. C.11-C.14).

The starting effective thickness, along with the sizes and shapes of the x-ray beam and laser hot spot incident on the sample surface, are inputs into the MINUTI software SIMX module (Sturhahn, 2021), which models the temperature evolution of the normalized delayed counts as a function of temperature and fits the measured data to constrain the melting temperature (Fig. 4.4c) (see D. Zhang et al., 2016). We illustrate the effects of x-ray beam size and starting thickness on the Mössbauer intensity profiles as a function of temperature in a series of forward models (Fig. C.15). We additionally show effects of a small offset between the x-ray beam and the laser hotspot, which is a fit parameter in all heating runs (reported in Table C.1) and is in good agreement with offset magnitudes visually estimated with CCD cameras during heating. By incorporating experiment-specific details with an underlying

physical basis for the temperature evolution of scattering events, this approach provides a meaningful and quantitative basis for interpreting the presence of melt.

X-ray diffuse scattering

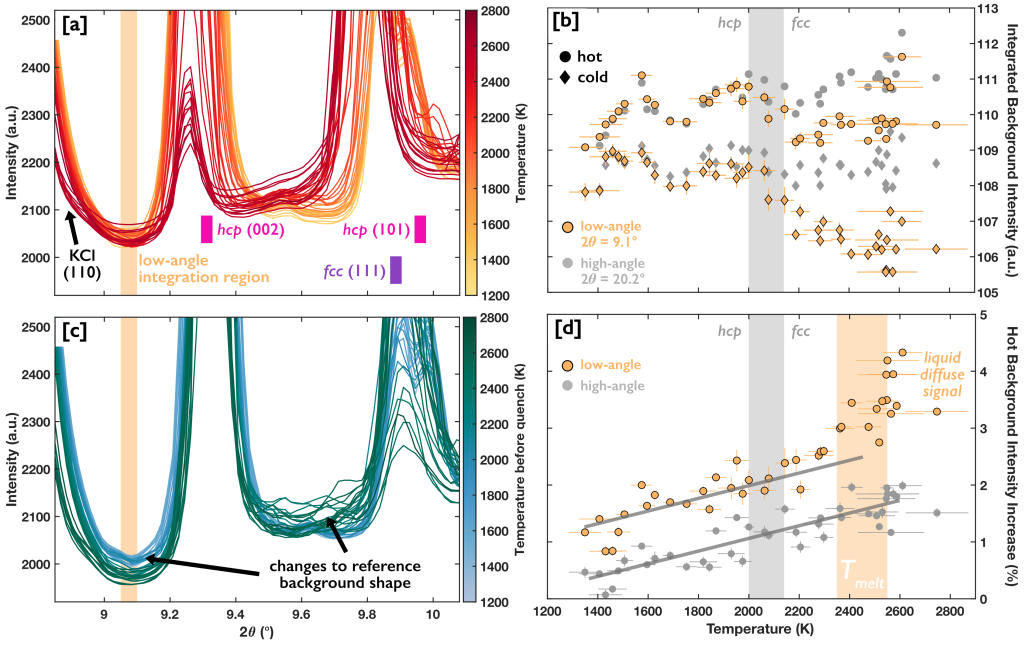

Figure 4.5: Background intensity analysis for heating run D1P2S3 (49-56 GPa). Panels [a] and [c] show high temperature ("hot") and quenched ("cold") integrated XRD patterns, respectively, in the region expected to exhibit the strongest liquid diffuse scattering signal. Quenched patterns show noisy fluctuations in the reference background shape, especially above the *hcp-fcc* transition (2070 ± 70 K) due to recrystallization of the sample. Low-angle integration region (orange bar) is selected due to relative isolation from reflections and smaller fluctuations due to recrystallization. Panel [b] shows integrated intensities at low-angle (orange) and high-angle (gray) regions for both hot (circle) and cold (diamond) patterns. Shaded gray bar represents the *hcp-fcc* transition. Panel [d] shows normalized hot background intensities after the background updating procedure (Section 4.3.2) that reveals a liquid diffuse scattering signal from the melt and allows for constraining the melting temperature (shaded orange bar). Gray lines are guides for the eye to demonstrate the presence and absence of the diffuse signal at the low-angle (orange) and high-angle (gray) regions, respectively.

Melting is revealed in XRD measurements by a liquid diffuse scattering signal, whose intensity must overcome a relatively large baseline background to be statistically detectable and may be difficult to identify solely from visual inspection of diffraction patterns. To quantify background intensity changes, we select a narrow

background near the lowest 2θ sample reflections (Fig. 4.5a,c), an area relatively isolated from Bragg reflections and consistently shown to produce the strongest diffuse signal (e.g., Anzellini et al., 2013), and integrate this region for both the "hot" high-temperature and "cold" quenched patterns (Fig. 4.5b). The cold patterns in burst heating mode produce "snapshots" of the baseline reference background shape as it evolves during heating. Most heating runs exhibit noisy fluctuations in the reference background, likely caused by recrystallization above the *hcp-fcc* transition, that lead to the diffuse signal being difficult or impossible to detect in the hot patterns (Figs. C.2-C.8) (e.g., Asanuma et al., 2010). The two continuous heating runs similarly exhibit background fluctuations and no obvious diffuse signal, indicating that the effect of recrystallization on background intensities is independent of heating mode (Figs. C.9-C.10). Background fluctuations behave differently at different reflection angles (Fig. 4.5b), making it difficult to detect a diffuse signal by only comparing hot intensities at different angles.

We introduce a background updating method to quantify changes in the reference background level and facilitate the determination of the liquid diffuse signal onset. This method involves normalizing each hot intensity by the corresponding cold intensity, essentially updating the shape of the reference background with each heating step and removing the noisy fluctuations caused by recrystallization (Fig. 4.5d). For all burst heating runs, this procedure reveals the onset of a statistically significant discontinuous increase in background intensity that we interpret as the onset of a liquid diffuse signal. The gentle increase in background intensity before melting may be attributed to thermal diffuse scattering of the solid sample. We explore the effect of integrating different background regions, including fits to full 2θ backgrounds (Text C.3, Figs. C.16-C.17), and find that the strongest sensitivity to a liquid diffuse signal is achieved with integration of the narrow low-angle region and use of the reference background updating method.

Unit-cell volumes

Lattice parameters and unit cell volumes for $Fe_{0.8}Ni_{0.1}Si_{0.1}$ and KCl phases are determined from fits of the XRD patterns using the GSAS-II software package (Toby & Von Dreele, 2013) for a sampling of measurements from each heating run (Fig. 4.6). For most runs, the melting temperature as determined by the liquid diffuse scattering signal seems to generally align with the onset of a volume plateau (Anzellini et al., 2013), though scatter in the volume data poses a challenge to place

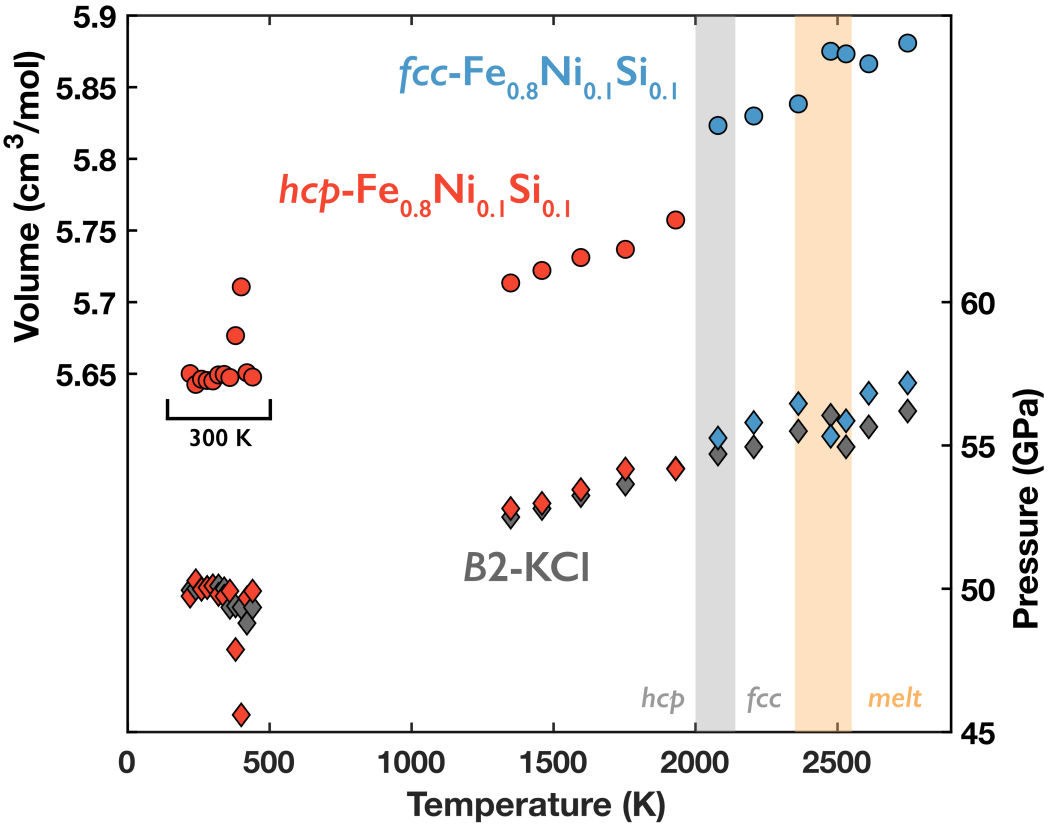

Figure 4.6: Unit-cell volumes and pressures for burst heating run D1P2S3. Volumes (left y-axis, circles) for *hcp*- (red) and *fcc*-$Fe_{0.8}Ni_{0.1}Si_{0.1}$ (blue) are constrained from fits to integrated XRD patterns using GSAS-II (Toby & Von Dreele, 2013). *In-situ* pressures (right y-axis, diamonds) for the sample and the KCl pressure medium (gray) are calculated from volumes using previously published thermal equations of state (see Section 4.3.3). 300 K measurement results are spaced out for ease of viewing in the order of acquisition sequence, from first (leftmost) to last (rightmost) heat and quench step. Onset of a plateau in volumes aligns with the melting temperature determined from the liquid diffuse scattering signal (orange bar). The shaded gray bar represents the *hcp-fcc* transition.

precise constraints on the melting temperature. For the two continuous heating runs, where no diffuse signal can be detected, we can estimate a melting temperature from the onset of a volume plateau (Figs. C.9-C.10). We additionally calculate c/a ratios of the *hcp* phase for all measurements (Fig. C.18) and find excellent agreement with previous reports (Komabayashi, Pesce, Sinmyo, et al., 2019; Morrison et al., 2018).

4.3.3 *In-situ* pressure determination and thermal pressure calculation

Previously published thermal equations of state (Edmund et al., 2020; Komabayashi, 2014; Komabayashi, Pesce, Sinmyo, et al., 2019; Morrison et al., 2018; Tateno et al., 2019) are used to calculate *in-situ* pressures of *B*2-KCl, *hcp*-$Fe_{0.8}Ni_{0.1}Si_{0.1}$, and *fcc*-$Fe_{0.8}Ni_{0.1}Si_{0.1}$ for high-temperature and quenched XRD measurements (Table C.2 and Text C.4). These equations of state result in excellent agreement between $Fe_{0.8}Ni_{0.1}Si_{0.1}$ and KCl pressures, consistently within 1-2 GPa, for both ambient and high temperatures (Fig. 4.6), though *fcc* pressures exhibit more scatter likely due to recrystallization effects. Final XRD pressures used for phase boundary location are an average of $Fe_{0.8}Ni_{0.1}Si_{0.1}$ and KCl pressures, with uncertainties calculated as the difference in pressures.

Using the *in-situ* pressures calculated for the XRD measurements, we can constrain the thermal contribution to pressures in the sample chamber as a function of temperature. We calculate thermal pressures of the $Fe_{0.8}Ni_{0.1}Si_{0.1}$ sample by compiling all hot pressure increases relative to pressures of the corresponding quenched measurement. A linear fit to all sample thermal pressures constrains a slope of 2.9±0.9 GPa per 1000 K, in excellent agreement with the fit to all KCl thermal pressures (2.9±0.1 GPa per 1000 K) (Fig. 4.7). Based on these *in-situ* measurements, we report a thermal pressure model for $Fe_{0.8}Ni_{0.1}Si_{0.1}$ in a KCl pressure medium: 2.9 GPa per 1000 K with an added uncertainty of 3 GPa on pressures at melting. This thermal pressure model accounts for uncertainties in KCl temperatures, while showing agreement with published *in-situ* measurements on Fe and $Fe_{0.9}Ni_{0.1}$ in a KCl pressure medium (see Text C.5 and Figs. C.20-C.21 for details). We apply this thermal pressure model to all SMS measurements in this study, with starting cold pressures calculated from the XRD measurements taken before and after each SMS heating run.

4.3.4 Phase diagram of $Fe_{0.8}Ni_{0.1}Si_{0.1}$

We present a summary of all measurements conducted in this study in Figure 4.8, spanning a range from 20 to 83 GPa and 1200 to 3500 K, with *P-T* conditions

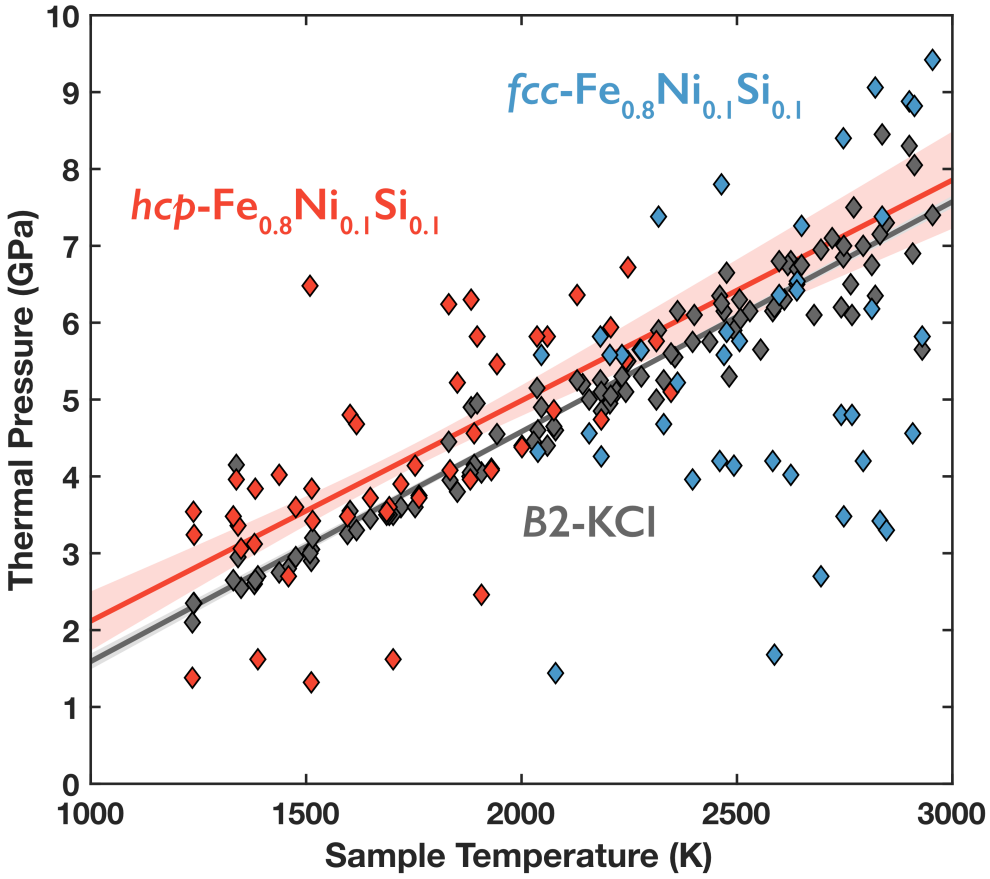

Figure 4.7: Compilation of all thermal pressures of all XRD measurements in this study, calculated as the difference between hot and corresponding quenched cold pressures, for *hcp*- (red) and *fcc*-$Fe_{0.8}Ni_{0.1}Si_{0.1}$ (blue) and *B*2-KCl (gray). Linear fits of thermal pressure slopes (solid lines) for *hcp*-$Fe_{0.8}Ni_{0.1}Si_{0.1}$ [2.9±0.9 GPa per 1000 K] and *B*2-KCl [2.9±0.1 GPa per 1000 K] show excellent agreement. Onset of scatter in pressure for the *fcc* phase corresponds to the onset of melting in the XRD measurements. For further details on the thermal pressure model constructed from these data, see Section 4.3.3, Text C.5, and Figs. C.19-C.21.

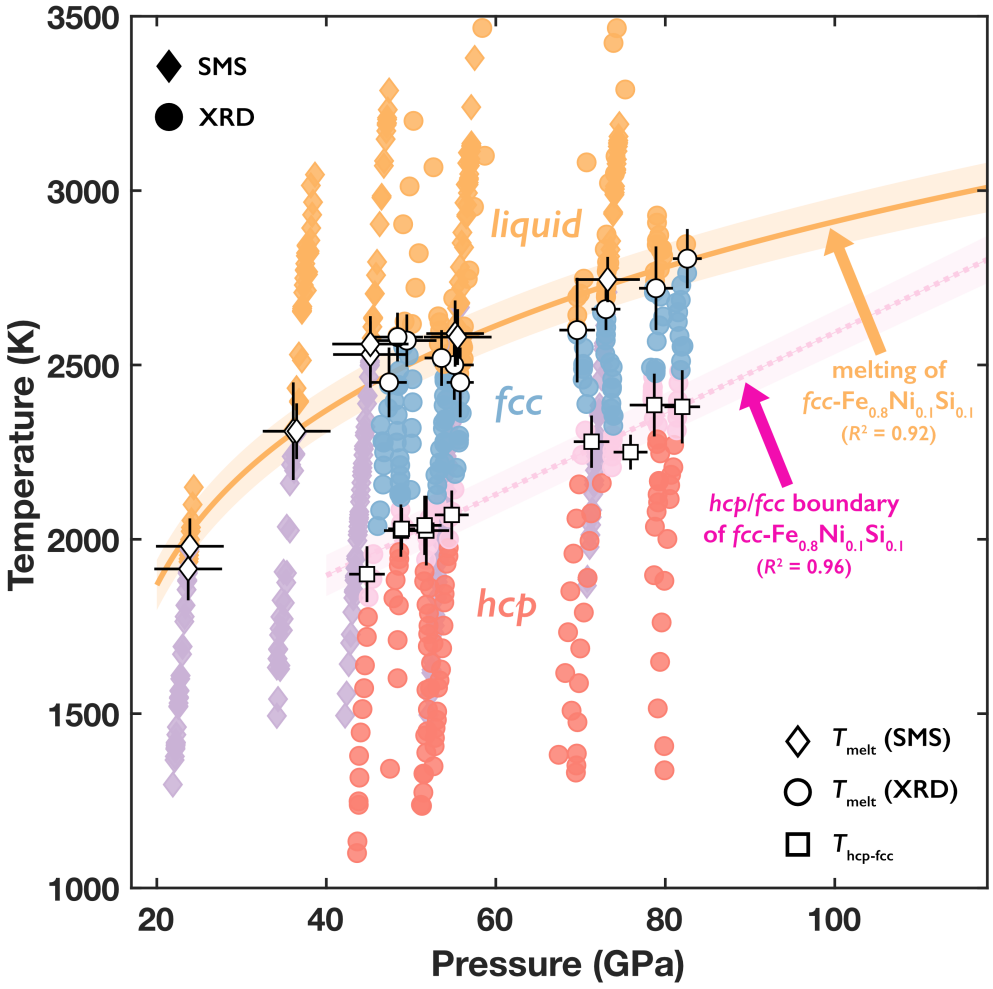

Figure 4.8: Compilation of pressure, temperature, and phase conditions of all measurements (color points) in this study for SMS (diamonds) and XRD (circles) heating runs. White points represent phase boundaries as determined in Sections 4.3.1 and 4.3.2 (reported in Table C.1). Melting temperatures from SMS and XRD techniques exhibit excellent agreement and reproducibility within uncertainties: liquid (orange), solid (purple, SMS; blue, XRD). XRD runs additionally constrain the solid *hcp-fcc* transition (*hcp* – red, *fcc* – blue, transition range – pink). Solid lines are fits to phase boundaries with shaded uncertainties. See Section 4.3.4 and Text C.6 for fitting details.

of measured phase boundaries reported in Table C.1. Melting temperatures demonstrate both strong reproducibility for each individual melt detection technique as well as excellent agreement within mutual uncertainties between the two independent techniques. We calculate a fit to all melting points with the commonly used empirical Simon-Glatzel formulation (Simon & Glatzel, 1929)

$$T_m = T_{m0}\left(\frac{P_m - P_{m0}}{x} + 1\right)^y$$

where the melting points (T_m, P_m) are related to a reference melting point (T_{m0}, P_{m0}) and x, y are adjustable, material-specific fit parameters. For $Fe_{0.8}Ni_{0.1}Si_{0.1}$, we find best-fit values T_{m0} = 1990±50 K, P_{m0} = 23±1 GPa, x = 10±5 GPa, and y = 0.18±0.05, resulting in the melting curve shown in Figure 4.8 with fit quality R^2=0.92. For the *hcp-fcc* boundary, we calculate a linear fit with slope 11.6±0.9 K/GPa and 0 GPa intercept 1430±55 K, resulting in the phase boundary shown in Figure 4.8 with R^2=0.96. The intersection of these two phase boundaries is calculated to constrain the location of the *hcp-fcc-liquid* quasi-triple point at 147±14 GPa and 3140±90 K. In reality, melting of an alloy should be described by a solidus and liquidus. Within our experimental resolution however, the solidus and liquidus are indistinguishable and are addressed simply as the melting curve of $Fe_{0.8}Ni_{0.1}Si_{0.1}$, in accordance with previous studies on Fe-Ni and Fe-Si systems (e.g., Asanuma et al., 2010; D. Zhang et al., 2016). Treatment of uncertainties and error propagation is discussed in Text C.6.

4.4 Discussion

4.4.1 Comparison with previous studies

In order to compare with previous studies and discuss the effects of silicon on the melting temperatures of Fe and Fe-Ni, we first conduct a systematic analysis to determine the relative effects from similar measurements. To do so, we apply our new thermal pressure model to previous SMS melting data on Fe and $Fe_{0.9}Ni_{0.1}$ (Jackson et al., 2013; D. Zhang et al., 2016), which were collected at the same beamline using identical experimental techniques as this study. Using these recalculated pressures, we fit updated SMS melting curves for *fcc*-Fe and *fcc*-$Fe_{0.9}Ni_{0.1}$ (Fig. 4.9, Text C.7). We now consider how the recalculated SMS data on Fe and $Fe_{0.9}Ni_{0.1}$ compare with other recent melting studies and find that discrepancies remain.

We therefore examine a recently proposed hypothesis (Morard et al., 2018) suggesting that differences in pressure metrology alone explain discrepancies in *fcc*-Fe melting temperatures among various techniques. To do so, we compile recent mea-

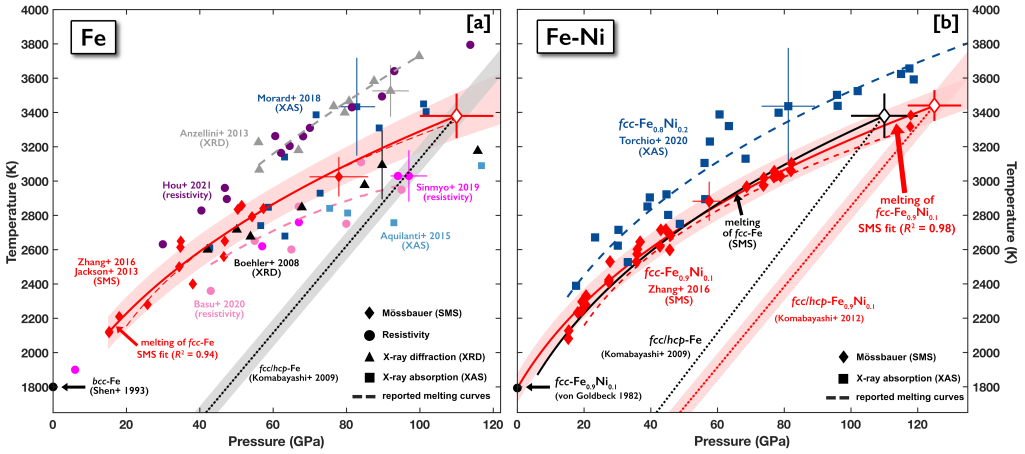

Figure 4.9: Melting points from a variety of experimental techniques. Panel [a]: melting of Fe as measured by SMS (red – pressures recalculated from Jackson et al., 2013; D. Zhang et al., 2016), resistivity changes (dark purple– Hou et al., 2021; magneta– Sinmyo et al., 2019; light pink– Basu et al., 2020), XAS (dark blue– Morard et al., 2018; light blue – Aquilanti et al., 2015), and XRD without burst heating and background updating (gray– Anzellini et al., 2013; black – Boehler et al., 2008). Representative uncertainties are shown for one data point from each study. An updated melting curve for *fcc*-Fe (solid red line) is fit to the SMS data. The *hcp-fcc-liquid* triple point (open red diamond) is calculated from the intersection of the melting curve with the previously determined *hcp-fcc* boundary (dotted line - Komabayashi et al., 2009). Previously reported melting curves are shown with dashed lines (red – D. Zhang et al., 2016, pink – Basu et al., 2020, gray – Anzellini et al., 2013). The 0 GPa melting point for *bcc*-Fe is taken from Shen et al. (1993). Panel [b]: melting of *fcc*-$Fe_{0.9}Ni_{0.1}$ as measured by SMS (red – pressures recalculated from D. Zhang et al., 2016) and of *fcc*-$Fe_{0.8}Ni_{0.2}$ as measured by XAS (dark blue – Torchio et al., 2020). An updated melting curve for *fcc*-$Fe_{0.9}Ni_{0.1}$ is shown with the solid red line. The *hcp-fcc-liquid* quasi-triple point (open red diamond) is calculated from the intersection of the melting curve with the previously determined *hcp-fcc* boundary (dotted red line – Komabayashi et al., 2012). The 0 GPa melting point for *fcc*-$Fe_{0.9}Ni_{0.1}$ is taken from von Goldbeck (1982). See Text C.7 for details.

surements of Fe melting from a range of *in-situ* techniques (Fig. 4.9a). The highest melting temperatures are from Anzellini et al. (2013) and Hou et al. (2021), while the lowest are reported by Aquilanti et al. (2015), Sinmyo et al. (2019), and Basu et al. (2020), spanning a range of ~700 K at 100 GPa. SMS results (Jackson et al., 2013; D. Zhang et al., 2016), fall in between these two bounds and are generally compatible with Sinmyo et al. (2019) and Basu et al. (2020) within mutual uncertainties. Results from Boehler et al. (2008) are in excellent agreement with SMS

results, while results from Morard et al. (2018) display better agreement with lower bound temperatures at lower pressures and general agreement with upper bound temperatures at higher pressures. This compilation shows disagreements among studies that are significantly larger than measurement uncertainties. Important for the discussion here, Anzellini et al. (2013) and Sinmyo et al. (2019) report nearly identical thermal pressures (Figs. C.20-C.21, Text C.5), while displaying up to 700 K difference in melting temperatures.

The above comparisons suggest that pressure metrology alone cannot resolve discrepancies in *fcc*-Fe melting data. They also cannot necessarily be attributed to the specific *in-situ* diagnostics used to determine the onset of melting. This can be seen from the fact that similar diagnostic methods for melt detection, such as sample resistivity (Basu et al., 2020; Hou et al., 2021; Sinmyo et al., 2019), changes in x-ray absorption spectra (XAS) (Aquilanti et al., 2015; Morard et al., 2018), and appearance of a liquid diffuse x-ray scattering signal (XRD) (Anzellini et al., 2013; Boehler et al., 2008), have all given results at both the upper and lower temperature bounds (Fig. 4.9a). Our study examines independent experimental datasets, from XRD with a background updating method and from SMS, finding excellent agreement in melting temperatures. Therefore, identical diagnostic methods may still involve different interpretations of the onset of melting.

The apparent discrepancies may also result from other experimental factors. One possibility is carbon contamination from the diamond anvils (V. Prakapenka et al., 2003), which could lead to underestimated melting temperatures due to the formation and melting of Fe_3C, as suggested by Morard et al. (2018). However, this explanation is difficult to apply to the measurements of Boehler et al. (2008) and Sinmyo et al. (2019), both of whom observed the loss of Fe reflections upon melting and no Fe_3C reflections in their XRD data. Another possibility is variable thickness of samples and differing heating methods (one-sided or two-sided laser heating, and electrical heating), which could produce temperature gradients in the sample and potentially lead to overestimated melting temperatures, as suggested by Sinmyo et al. (2019). However, such axial temperature gradients are unlikely to be larger than ~250 K for typical sample thicknesses (~5 μm) and would be negligible for thin samples (~1 μm) (Sinmyo et al., 2019). Another factor could involve temperature determination from Planck fits of thermal emission spectra, which could lead to both overestimation and underestimation of melting temperatures, as suggested by Hou et al. (2021). We note that the temperature measurement system at beamline 3-ID-B

(APS) was calibrated using the temperature asymmetry of the NRIXS spectra (Lin et al., 2004; Sturhahn & Jackson, 2007), which is independent of the optical path. Aquilanti et al. (2015) also suggested that misalignments of the x-ray beam and laser hotspot could lead to overestimation of melting temperatures.

For Fe-Ni, results from Torchio et al. (2020) on the melting of *fcc*-$Fe_{0.8}Ni_{0.2}$ using x-ray absorption spectroscopy (XAS) show systematically higher temperatures than SMS results on *fcc*-$Fe_{0.9}Ni_{0.1}$ (D. Zhang et al., 2016), but are compatible within mutual reported uncertainties, spanning a range of ~300 K at 100 GPa (Fig. 4.9b), and both studies reach similar conclusions. Specifically, when comparing with XAS results on Fe (Morard et al., 2018), Torchio et al. (2020) found negligible effect of nickel on melting temperatures, in excellent agreement with the relative effect of nickel determined by SMS measurements (D. Zhang et al., 2016). These conclusions lend confidence that the relative effect of alloyed-Ni and Si on iron's melting curve can be well-constrained, despite open questions about the accuracy of various *fcc*-Fe melting curves.

4.4.2 Effect of nickel and silicon on phase relations in planetary cores

A recent compilation of melting studies on silicon-bearing iron alloys measured by XRD without burst heating and background updating (Fischer 2016) illustrates the challenge of interpreting the effect of silicon on the melting temperatures of iron due to sparsity and scatter of data (reproduced in Fig. 4.10). When compared to the melting curve of pure Fe measured by XRD (Anzellini et al., 2013), $Fe_{0.84}Si_{0.16}$ (9wt%Si) shows a decrease in melting temperature below 50 GPa and a possible increase above 90 GPa (Fischer et al., 2013), while $Fe_{0.74}Si_{0.27}$ (16wt%Si) shows a decrease of variable magnitude from 20 to 140 GPa (Fischer et al., 2012) and $Fe_{0.70}Si_{0.30}$ (18wt%Si) shows negligible effect below 60 GPa and a growing decrease from 60 to 120 GPa (Asanuma et al., 2010). For nickel-bearing compositions, the only prior static compression melting study on such alloys shows that the melting curves of $Fe_{0.78}Ni_{0.04}Si_{0.18}$ (10wt%Si) and $Fe_{0.70}Ni_{0.04}Si_{0.26}$ (15wt%Si) measured by XRD (Morard et al., 2011) exhibit lower temperatures and greater curvature relative to Fe (Anzellini et al., 2013). Two measurements of $Fe_{0.75}Ni_{0.07}Si_{0.18}$ (10wt%Si) from a shock compression study (Y. Zhang et al., 2018) may be compatible with results from Morard et al. (2011), though the studied pressure ranges do not overlap, and significant uncertainty may exist in the thermal conductivity values used to model the measured raw interfacial temperatures. Importantly, no melting studies exist on alloys with more moderate concentrations of Si (<9wt%).

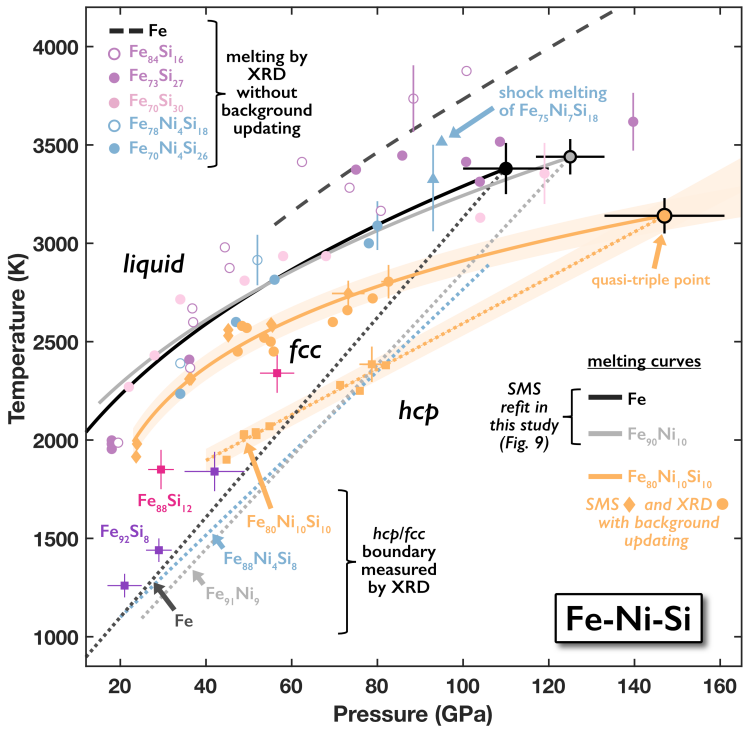

Figure 4.10: Phase boundaries of $Fe_{80}Ni_{10}Si_{10}$ measured in this study (orange lines; see Fig. 4.8 for orange symbol shapes), with the calculated *hcp-fcc-liquid* quasi triple point (black outlined orange circle) and a Simon-Glatzel model for the melting curve (Text C.7). Solid black and gray curves are SMS melting of Fe and $Fe_{90}Ni_{10}$, respectively, as refit in this study (Fig.]4.9, Text C.7). Dashed black line is the melting of Fe determined by XRD without burst heating and background updating (Anzellini et al., 2013). Dotted lines show the *hcp-fcc* boundary previously determined by XRD (in a resistive-heated DAC) for Fe (black, Komabayashi et al., 2009), $Fe_{91}Ni_9$ (gray, Komabayashi et al., 2012), and $Fe_{88}Ni_4Si_8$ (blue, Komabayashi, Pesce, Morard, et al., 2019), while squares show the *hcp-fcc* boundary for $Fe_{92}Si_8$ (purple) and $Fe_{88}Si_{12}$ (pink) (Komabayashi, Pesce, Sinmyo, et al., 2019). Melting temperatures of Fe(-Ni)-Si from previous studies using XRD without burst heating and background updating (in a laser-heated DAC) are plotted as an average of reported lower and upper bounds (empty purple circles: Fischer et al., 2013; filled purple circles: Fischer et al., 2012; filled pink circles: Asanuma et al., 2010; blue circles: Morard et al., 2011). Shock melting of $Fe_{75}Ni_7Si_{18}$ is shown in blue triangles (Y. Zhang et al., 2018), with an asymmetric error bar encompassing the raw interfacial temperature measurement value (-150 K) and uncertainty (121 K). Error bars are plotted for at least one representative data point for each melting study.

Interpretation is challenging in part because Fe crystallizes in the *fcc* structure from the melt below 100 GPa and *hcp* above 100 GPa, while alloys with relatively high Si concentration (≥9wt%) can exhibit phase mixtures like *B*2+*fcc*+*hcp* or the presence of *bcc*-like phases (Asanuma et al., 2010; Fischer et al., 2013; Wicks et al., 2018). Morard et al. (2011) similarly observed a mix of *fcc* and *bcc* phases present at melting for $Fe_{0.78}Ni_{0.04}Si_{0.18}$ (10wt%Si) in the studied pressure range (20-80 GPa). In contrast, lower Si concentrations such as $Fe_{0.92}Si_{0.08}$ (4wt%Si) and $Fe_{0.88}Si_{0.12}$ (6.5wt%Si) have been shown to exhibit *fcc* and *hcp* stability fields similar to Fe, albeit with the *hcp-fcc* transition boundary shifted to higher temperatures (Komabayashi, Pesce, Morard, et al., 2019). Komabayashi, Pesce, Sinmyo, et al. (2019) showed that $Fe_{0.88}Ni_{0.04}Si_{0.08}$ (4wt%Si) exhibits *fcc* and *hcp* stability fields similar to Fe but with a flatter transition boundary relative to Fe (Komabayashi et al., 2009) (Fig. 4.10), in agreement with an earlier study on $Fe_{0.88}Ni_{0.04}Si_{0.08}$ (4wt%Si) that observed the *hcp* phase at Earth's inner core conditions (Sakai et al., 2011)).

Using the updated SMS melting curves of *fcc*-Fe and *fcc*-$Fe_{0.9}Ni_{0.1}$, we systematically evaluate the effect of silicon. We find that the addition of 10mol% Si reduces the melting temperature of $Fe_{0.9}Ni_{0.1}$ by ~250 K at low pressures (<60 GPa) and up to 500 K at conditions of Earth's outermost core (Fig. 4.10). These findings are in qualitative agreement with results from Morard et al. (2011), who found a similar reduction in temperature and increase in curvature of the melting boundary for $Fe_{0.70}Ni_{0.04}Si_{0.26}$ relative to pure Fe (Anzellini et al., 2013). While the relative effect is consistent, we note the systematically larger melting temperatures in these aforementioned XRD studies compared to results from this study. These offsets could be caused by several experimental factors discussed above for pure Fe, some of which may explain the findings of Asanuma et al. (2010), who identified melting of $Fe_{0.70}Si_{0.30}$ from temperature discontinuities and recovered sample textures but could not detect liquid diffuse signals.

Regarding subsolidus phase relations, we find that $Fe_{0.8}Ni_{0.1}Si_{0.1}$ exhibits *fcc* and *hcp* stability fields similar to Fe but with a transition boundary featuring a much shallower slope and higher temperatures at low pressure. This combined effect of Ni and Si is in qualitative agreement with the previous study on $Fe_{0.88}Ni_{0.04}Si_{0.08}$ (Komabayashi, Pesce, Sinmyo, et al., 2019), with a more pronounced flattening effect on the boundary in this study due to greater concentrations of both Ni and Si. The reduction in melting temperatures and flattening of the *hcp-fcc* boundary leads to an *hcp-fcc-liquid* quasi-triple point for $Fe_{0.8}Ni_{0.1}Si_{0.1}$ at higher pressures

and lower temperatures relative to Fe and Fe-Ni. The resulting melting temperature of $Fe_{0.8}Ni_{0.1}Si_{0.1}$ is 400 K lower than that of *fcc*-$Fe_{0.9}Ni_{0.1}$ at 125 GPa and 500 K lower than that of *hcp*-$Fe_{0.9}Ni_{0.1}$ at 150 GPa, if the *hcp*-$Fe_{0.9}Ni_{0.1}$ melting curve has the same shape as the *hcp*-Fe melting curve (Sinmyo et al., 2019).

4.5 Conclusion

In this study, we present a multi-technique approach for probing the dynamics and spatial positions of atoms in iron-bearing materials to measure solid phase relations and melting curves at extreme conditions. Specifically, we apply synchrotron Mössbauer spectroscopy and x-ray diffraction methods to $Fe_{0.8}Ni_{0.1}Si_{0.1}$, a composition compatible with recent estimates for the cores of Earth and Mercury, to clarify the combined effects of nickel and silicon on planetary cores. To our knowledge, this study represents the first combined use of these two techniques, sensitive to different atomic-level properties at different time and length scales, to detect melt. The introduction of a burst heating and background updating method for the XRD measurements leads to excellent agreement in the melting temperatures determined independently by the two techniques. Using a thermal pressure model constructed in this study, we present updated SMS melting curves for *fcc*-Fe and *fcc*-$Fe_{0.9}Ni_{0.1}$ to systematically evaluate the relative effect of silicon.

We find that the addition of 10mol% Si to $Fe_{0.9}Ni_{0.1}$ reduces melting temperatures by 250 K at low pressures (<60 GPa) and flattens the *hcp-fcc* boundary. These pressures are relevant to small terrestrial-type cores like in Mercury (<35 GPa), and if silicon is the major light element in Mercury's core, the lower melting temperatures imply lower core temperatures and/or a smaller inner core (Knibbe & van Westrenen, 2018). We find that silicon extends the *hcp-fcc-liquid* quasi-triple point of $Fe_{0.9}Ni_{0.1}$ to higher pressures and lower temperatures, resulting in a decrease in melting temperature at Earth's outermost core pressures by 500 K. If one assumes an identical curvature of the *hcp* melting boundary for $Fe_{0.8}Ni_{0.1}Si_{0.1}$ as for Fe (D. Zhang et al., 2016) and no effect on the shape of the core adiabat, then 10mol% (5.3wt%) silicon would suggest that the core-side temperature of the core-mantle boundary (CMB) is around 3500 K. This temperature is below the lowest estimates for solidus temperatures of lower mantle assemblages at the CMB (Nomura et al., 2014) and lends support for solid-state interpretations of seismic heterogeneities like ultralow velocity zones (Dobrosavljevic et al., 2019; Jackson & Thomas, 2021; Wicks et al., 2017).

Chapter 5

MELTING AND VACANCY STRUCTURE TRANSITIONS IN $Fe_{0.94}O$ UP TO 140 GPa

5.1 Introduction

$Fe_{1-x}O$ wüstite has long been recognized as central to the properties and evolution of Earth and other rocky planetary bodies (Coppari et al., 2021; Fischer, Campbell, Lord, et al., 2011; Hazen & Jeanloz, 1984; Labrosse et al., 2007; H.-k. Mao et al., 1996). It represents an end-member phase in Earth's major mineralogical systems, with its melting point representing an essential parameter for constructing models of the deep interior. In the FeO-MgO-SiO_2 system of the mantle, it controls crystallization sequences of Earth's primordial magma ocean (Boukaré et al., 2015; Labrosse et al., 2007; Miyazaki & Korenaga, 2019). Extensive study has been devoted to the Fe-FeO system in assessing the viability of oxygen as a major light element in Earth's outer core (Frost et al., 2010; Komabayashi, 2014; Ohtani & Ringwood, 1984; Seagle et al., 2008). FeO has further been implicated in chemical and heat exchanges between the core and mantle (Brodholt & Badro, 2017; Knittle & Jeanloz, 1991a; Manga & Jeanloz, 1996; Ozawa et al., 2009) and in the deep mantle hydrogen cycle (Ohtani, 2020) over geologic time.

In the last decade, the properties of $Fe_{1-x}O$ have received renewed attention in the context of ultralow velocity zones, enigmatic regions dispersed across Earth's heterogeneous mantle base (Garnero & Helmberger, 1998) located at edges of large thermochemical piles and at roots of major mantle plumes that source volcanic hotspots like Hawai'i, Iceland, and Yellowstone (e.g., French and Romanowicz, 2015; McNamara et al., 2010; Rost et al., 2005; Yu and Garnero, 2018). Recent work has suggested that these structures, originally posited to consist of partial melt (Williams & Garnero, 1996), can be explained by the presence of solid (Mg,Fe)O with high concentrations of FeO (Bower et al., 2011; Brown et al., 2015; Dobrosavljevic et al., 2019; Jackson & Thomas, 2021; Lai et al., 2022; M. Li et al., 2017; Reiss et al., 2019; Wicks et al., 2010; Wicks et al., 2017), leading to remarkably low seismic velocities, high seismic anisotropy (Finkelstein et al., 2018), and high conductivity (Ohta et al., 2014).

Precise determination of the high-pressure melting curve of $Fe_{1-x}O$ thus repre-

sents a key necessity for understanding Earth's early evolution and various present-day phenomena in its deep interior. However, the melting curve remains highly uncertain, especially at pressures of the deep lower mantle and core. Experimental measurements at high pressures have relied on proxy phenomena, like changes in sample resistivity or emissivity, and extend to just above 70 GPa, where they disagree by more than 700 K (Fischer & Campbell, 2010; Knittle & Jeanloz, 1991b). Recent extrapolations to lowermost mantle pressure (136 GPa) from experimental work and thermodynamic calculations exhibit a similarly extreme uncertainty range (Komabayashi, 2014) that partially overlaps with possible core-mantle boundary temperatures (e.g., D. Zhang et al., 2016). This makes it impossible to determine the viability of solid FeO-rich structures in the region and introduces large uncertainties into models of Earth's thermochemical evolution.

Investigation of the $Fe_{1-x}O$ phase diagram is further complicated by the presence of iron vacancies. Studies at ambient pressure have observed the formation of short-range ordered vacancy clusters, consisting of Fe^{2+} vacancies and interstitial Fe^{3+} atoms, which can in turn develop into long-range periodic superstructures within the $Fe_{1-x}O$ lattice (Gavarri & Carel, 2019; Hazen & Jeanloz, 1984; Koch & Cohen, 1969; Manenc, 1968; Roth, 1960; Welberry et al., 2014). Details of possible cluster sizes and superstructure spacings have been debated, but studies generally agree that superstructures develop at moderately elevated temperatures. At higher temperatures, but below melting, some studies suggest a vacancy order-disorder transition could occur in $Fe_{1-x}O$ (Fender & Riley, 1969; Hazen & Jeanloz, 1984), as well as in related materials like $Fe_{1-x}S$ (Koulialias et al., 2021; Nakazawa & Morimoto, 1971; H. Wang & Salveson, 2005) and $Fe_{1-x}Se$ (T. K. Chen et al., 2014; Okazaki, 1959) with implications for superconductivity (Fang et al., 2016; McQueen et al., 2009; C. H. Wang et al., 2018). However, no studies have explored such iron vacancy transitions at simultaneous high pressures and temperatures nor investigated possible consequences of such phenomena for precise determination of melting temperatures.

In this study, we study the behavior of $Fe_{0.94}O$ at simultaneous high pressures and temperatures using a multi-technique approach that combines results from two *in-situ* techniques – synchrotron x-ray diffraction, sensitive to atomic positions, and synchrotron Mössbauer spectroscopy, sensitive to dynamics of the iron atoms. This multi-technique approach was recently developed to study phase relations of $Fe_{0.8}Ni_{0.1}Si_{0.1}$, resulting in precise melting temperature determination and excellent

agreement between the two independent techniques (Dobrosavljevic et al., 2022). A total of 1,020 x-ray diffraction patterns with 105 synchrotron Mössbauer measurements are collected over 22 separate heating runs, covering a range of 30 to 140 GPa and 300 to 4500 K.

5.2 Methods

5.2.1 Sample preparation

Sample material $Fe_{1-x}O$ wüstite was synthesized using 95% enriched ^{57}Fe in a gas-mixing furnace at ambient pressure (B. Chen et al., 2012). The sample pellet was equilibrated at ~1575 K for two runs of 20 hours each just above the iron-wüstite fugacity buffer (an oxygen potential of $10^{-9.6}$ atm) (Wicks, 2013). Sample homogeneity was confirmed using a JEOL JXA-8200 electron microprobe. The ambient pressure lattice parameter was determined to be $a = 4.306(1)$ Åusing x-ray diffraction (Wicks et al., 2017). The precise chemical composition of the material was computed using the lattice parameter and the relationship reported by McCammon and Liu (1984) ($a = 3.856 + 0.478x$ for $Fe_{1-x}O$), giving a composition of $Fe_{0.941(2)}O$. Samples in this study were taken from the same material batch studied previously by Wicks et al. (2017), who reported the sound velocities of the material up to 94 GPa.

High pressure was achieved using diamond anvil cells (DACs) with diamond culet diameters ranging from 100 to 400 μm. Seats holding the anvils were composed of tungsten carbide on the upstream side of the DAC and carbon boron nitride on the downstream side in order to maximize the accessible 2θ scattering angle range for the XRD measurements. Rhenium gaskets serving as sample chambers were pre-indented to thicknesses of 30-50 μm from a starting thickness of 250 μm. Each gasket was drilled with an electron discharge machine to produce sample chambers ranging from 35 to 165 μm, depending on the diamond culet size. Samples of starting thickness 10 μm were sandwiched between flakes of dehydrated KCl with a minimum thickness of 10 μm that served as both thermal insulation and a pressure transmitting medium. At least one ruby sphere was loaded inside the sample chamber without contact with the sample.

Once loaded, each DAC was heated in a vacuum oven for 24 hours to minimize moisture in the sample chamber and subsequently sealed and compressed to its target pressure. Sample chamber pressures were estimated before and after each heating run from the fluorescence spectrum of the ruby spheres (Shen et al., 2020)

and measured during the heating cycle for the XRD measurements. Sample heating locations were laser annealed at ~1500 K before the heating run to relax possible deviatoric stresses in the sample induced during synthesis and to determine sample coupling behavior with the infrared lasers. For XRD measurements, annealing time was ~1-2 minutes, while for SMS measurements, we annealed for ~5 minutes to allow for collection of a high-quality SMS time spectrum.

5.2.2 Experimental procedures

The melting of $Fe_{0.94}O$, hereafter referred to as FeO, is detected using a multi-technique approach that combines results from two *in-situ* methods: synchrotron x-ray diffraction (XRD) and synchrotron Mössbauer spectroscopy (SMS). XRD measurements are conducted at beamline 13-ID-D of the Advanced Photon Source (APS) using incident x-rays of energy 37 keV focused to a spot size of ~3x3 μm^2. We use double sided heating with infrared lasers (flat-top heating spot diameter ~10 μm (V. B. Prakapenka et al., 2008)) in a burst heating mode that collects alternating pairs of high-temperature ("hot") and 300 K ("quenched") measurements with exposure times between 1 and 4 seconds. SMS measurements are conducted at beamline 3-ID-B of the APS using incident x-rays prepared with a bandwidth of 1 meV at the 14.4125 keV energy of the nuclear resonance of ^{57}Fe (Toellner, 2000) (full-width half-maximum FWHM ~16x16 μm^2). Double sided heating with infrared lasers (FWHM ~35x35 μm^2) is controlled by a computer acquisition sequence that features an incremental ramp of laser power and collection of time-integrated Mössbauer signal intensity every 3 seconds. *In-situ* pressures are determined in the XRD heating runs from fits to integrated XRD patterns, while pressures before and after SMS heating runs are determined from the fluorescence spectrum of the ruby spheres (Shen et al., 2020). The experimental techniques and measurement procedures are discussed in full detail in Dobrosavljevic et al. (2022).

5.3 Data analysis

5.3.1 X-ray diffraction measurements

We analyze a total of 1,020 x-ray diffraction images in 19 separate heating runs over a pressure range of 30 to 140 GPa. XRD images are first azimuthally integrated using the software DIOPTAS (Prescher & Prakapenka, 2015). We perform fits to the integrated patterns with the GSAS-II software package (Toby & Von Dreele, 2013) for at least 6 measurements in each heating run in order to index the observed Bragg reflections and constrain unit-cell volumes of the two materials, allowing for *in-situ*

determination of pressure using published equations of state (Section 5.4.4). We fit an additional ~160 measurements from four representative heating runs in order to assess sample pressure dependence on temperature during heating, referred to as thermal pressure (Section 5.4.4). All 1,020 integrated patterns are further analyzed as follows.

For all heating runs across the entire pressure range, all reflections observed at the start of heating can be indexed by $B1$-FeO at high temperatures (>1500 K, up to 140 GPa), $rB1$-FeO at 300 K (up to 128 GPa), and $B2$-KCl at all temperatures. As the heating temperature increases during each run, we systematically observe the emergence of additional reflections for both hot and quenched measurements (Fig. 5.1). These are observed in both the integrated patterns and the raw XRD images, located at identical azimuthal angles as $B1$ and $rB1$-FeO reflections with small offsets in the 2θ scattering angle. The positions of these additional reflections, often referred to as satellite reflections, have been consistently observed in previous studies on $Fe_{1-x}O$) and attributed to long-range ordering of iron vacancy clusters at ambient (Gavarri & Carel, 2019; Hazen & Jeanloz, 1984) and high pressure (Jacobsen et al., 2005). We analyze the evolution of sample and satellite reflection intensities during heating by integrating the area under all detectable reflections in each diffraction pattern, using a minimum of four sample and six satellite reflections. For the subsequent analysis, we consider the total sum of all satellite reflection intensities, as well as the total sum of sample reflection intensities normalized by that of the first measurement in the heating run.

We additionally analyze background intensities of each diffraction pattern to identify melting by detecting liquid diffuse scattering signals, shown consistently to appear most strongly in low-angle regions around the low-order sample reflections (e.g., Anzellini et al., 2013; Dobrosavljevic et al., 2022. We quantify background changes by selecting and integrating multiple background regions around the low-order sample reflections (Fig. 5.1-5.2) where diffuse scattering is expected to be strongest ("low-angle region"), as well as a "high-angle region" ($2\theta \sim 25°$) where no diffuse scattering is expected (Fig. 5.2). This approach was shown by Dobrosavljevic et al. (2022) to produce the strongest sensitivity to liquid diffuse signals in $Fe_{0.8}Ni_{0.1}Si_{0.1}$. Background regions are chosen to be as far removed from Bragg reflections as possible. For subsequent analysis, we normalize low-angle background intensities by high-angle intensities for both hot and quenched patterns to analyze relative changes in the low-angle diffuse scattering region. This allows

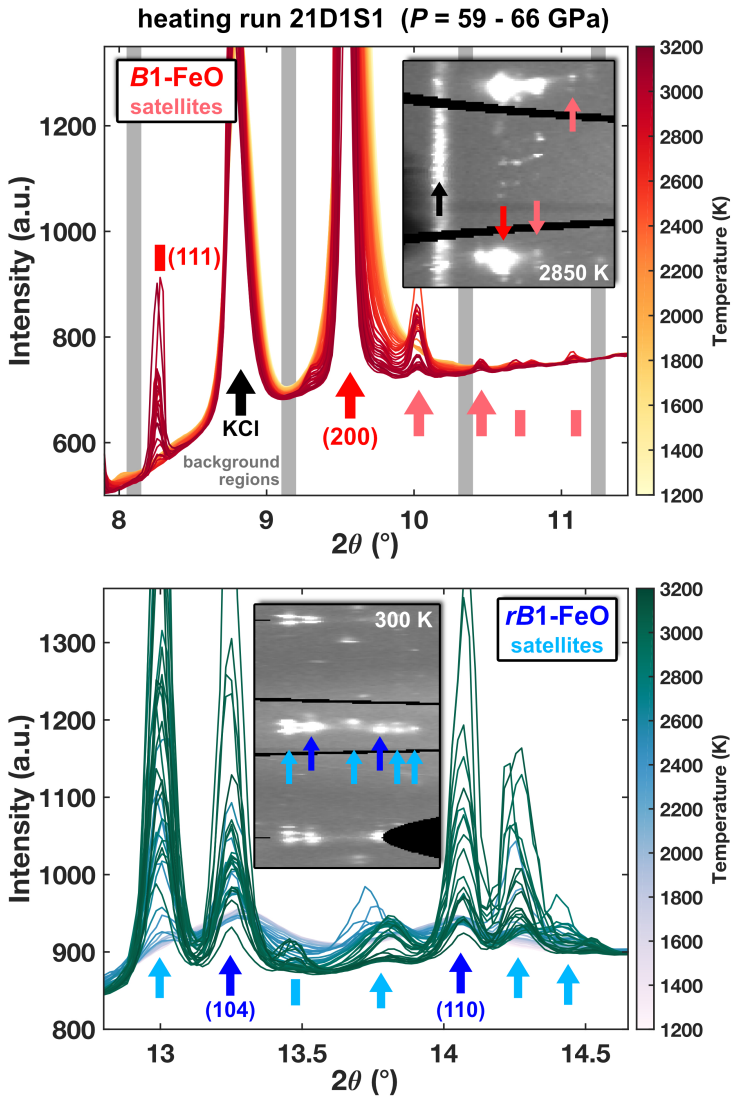

Figure 5.1: Integrated diffraction patterns from heating run 21D1S1 at high temperatures (top panel) and quenched (bottom panel). Colored bars and arrows indicate FeO sample (darker) and satellite (lighter) reflections. Insets show portions of caked 2D diffraction images from representative measurements in the heating run. Caked images plot scattering intensity as a function of scattering angle 2θ (horizontal) and azimuthal angle ψ (vertical), showing the same satellite and sample reflections indicated by arrows in the integrated patterns. Gray bars indicate integration regions for background intensity analysis.

for independent analysis of hot and quenched diffuse signal intensities as they evolve during each heating run.

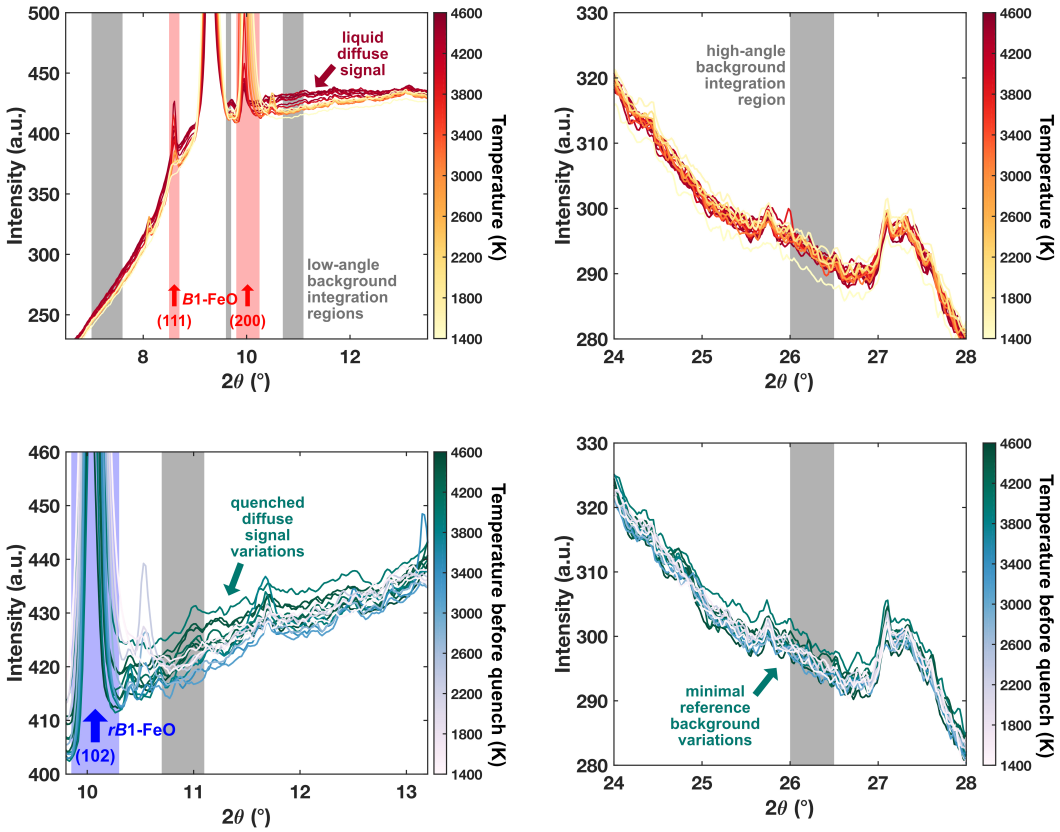

Figure 5.2: XRD heating run 21D8S1. Top panels show high-temperature integrated patterns. Shaded bars indicate FeO reflections (red) and background integration regions (gray). Bottom panels show quenched integrated patterns. Background intensities at low angles relative to high angles vary during the heating run, as shown for this run in Fig. 5.3.

5.3.2 Synchrotron Mössbauer measurements

Synchrotron Mössbauer spectroscopy (SMS) is sensitive to the nuclear resonant signal produced exclusively by solid-bound ^{57}Fe atoms as their nucleus is excited by incident x-rays and subsequently decays from its first excitation state, characterized by a transition energy of 14.4 keV and an excitation lifetime of 141 ns. Signal intensity is proportional to the temperature-dependent Lamb-Mössbauer factor $f_{LM} = e^{-k^2\langle u^2\rangle}$, where k is the wavenumber of the incident photon (1.161×10^8 cm^{-1}) and $\langle u^2\rangle$ is the mean-square displacement of the nucleus. As the sample is heated, a characteristic loss of signal intensity occurs when the mean-square dis-

placement becomes very large within the excitation lifetime, associated with the onset of melting.

We conduct three synchrotron Mössbauer heating runs at beamline 3-ID-B. The starting pressures at 300 K are determined from the ruby fluorescence spectrum (Shen et al., 2020), while the pressure increase at high temperature is determined from thermal pressures constrained by XRD measurements (Section 5.4.4, Table D.3). We begin each heating run by collecting a high-quality Mössbauer time spectrum while annealing the sample at ~1500 K for around 5 minutes (Dobrosavljevic et al., 2022; D. Zhang et al., 2016). We fit the time spectra using the software CONUSS (Sturhahn, 2000) to constrain the sample thickness at the start of the heating run. For the fits, we use estimates of the Lamb-Mössbauer factor based on previous measurements of $(Mg_{0.06}Fe_{0.94})O$ (Wicks, 2013) and the temperature dependence of the f_{LM} determined for iron by D. Zhang et al. (2022). In the heating runs, we then incrementally ramp up laser power on the sample over a series of 3-second intervals, while measuring the sample temperature using two different spectrometers (Dobrosavljevic et al., 2022; D. Zhang et al., 2015) and total integrated intensities of the SMS signal within a particular time window. Temperature uncertainties for each 3-second collection are estimated from fluctuations in the high-frequency (~100 Hz) measurements from the FasTeR spectrometer (Dobrosavljevic et al., 2022; D. Zhang et al., 2015).

5.4 Results and interpretations

5.4.1 XRD measurement observations

We identify several key trends that consistently appear across the set of XRD heating runs (Fig. 5.3, D.1). Firstly, we see strong anti-correlation in the intensities of the satellite reflections and of the diffuse scattering, for both hot and quenched measurements. Specifically, with increasing temperature in the hot measurements, we observe the onset of satellite reflections, which increase in intensity before dropping off at a temperature T_1. Simultaneously, the hot diffuse signal gradually decreases from its starting value before exhibiting a small increase in intensity at the same temperature T_1. In the quenched measurements, we observe a similar increase in satellite reflections that plateau at large intensities at T_1. Again showing strong anti-correlation, the diffuse scattering signal in quenched measurements gradually decreases and reaches a minimum at T_1. In many heating runs, sample temperatures additionally exhibit plateau-like behavior in their dependence on laser power as the sample reaches T_1.

In more than half of the heating runs, the sample is heated above the T_1 plateau and reaches a temperature T_2. Here, hot measurements continue to show no satellite intensities, but the hot diffuse signal now increases discontinuously to much larger values, up to 5% above the starting background intensity. Meanwhile, quenched measurements show a loss of satellite intensity and an increase in quenched diffuse signal intensity back to its starting value. The intensities of the FeO reflections also show distinct behavior at T_1 and T_2. $B1$ (hot) and $rB1$ (quenched) intensities exhibit fluctuations associated with the onset of satellite reflections and scattering around the starting intensity at T_1. Above T_2, $B1$ intensities drop to negligible but non-zero values (<20% of the starting intensity), while $rB1$ intensities remain large. Quenched samples in all heating runs exhibit the $rB1$ structure except in the two highest pressure runs, where quenching from T_2 preserves the $B1$ structure at 125 GPa. We do not observe evidence of the $B8$ structure at any of the P-T conditions explored in this study. The hottest sample temperature measured for each heating

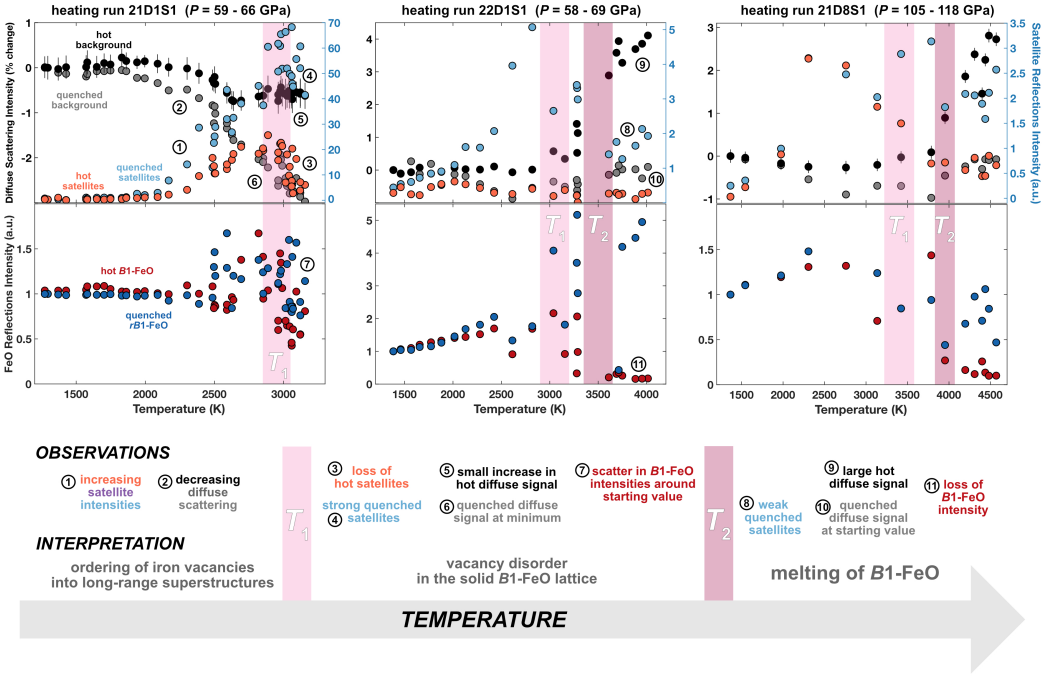

Figure 5.3: Three representative XRD heating runs (top and middle panels) showing temperature dependence of intensities of diffuse signals, satellite reflections, and FeO reflections. Shaded bars indicate vacancy disorder transition (light, T_1) and melting (dark, T_2). Schematic (bottom) highlights key observations for each portion of the heating runs with resulting interpretation.

step is used in these analyses, with uncertainties estimated at ~150 K from the scatter around the melting curve fit to XRD and SMS results 5.4.5. Reasonable transition temperature uncertainties are estimated from scatter in the data (Fig. 5.3).

5.4.2 Interpretation of XRD heating runs

We interpret the observed trends as consequences of iron vacancy clusters arranged in long-range ordered superstructures at moderate temperature, a vacancy order-disorder transition in the solid sample at T_1, and melting of the $B1$-FeO lattice at T_2. Specifically, we suggest that the sample initially features disordered vacancies which then progressively develop long-range ordering with increasing temperatures, leading to the anti-correlated increase of satellite reflections and the loss of the initial diffuse signal in both hot and quenched samples. At T_1, the iron vacancies lose their long-range ordering and transition to a disordered state, leading to a loss of satellite intensities and small increase in diffuse intensity. Importantly, the sample remains solid at T_1, evidenced by $B1$-FeO intensities scattering around their initial intensity and a negligible diffuse signal. Only above T_2 do we see clear evidence for melting – significant diffuse scattering and a loss of intensity from the sample's Bragg reflections. Further, samples quenched from below melting temperatures (T_2) show evidence of retained superstructures with anti-correlated strong satellite intensities and weak diffuse intensities, while samples quenched from above T_2 show weak or absent satellite reflections and a return of diffuse intensities to starting values, suggesting that vacancies are again disordered as in the starting sample. We note that the intensities of the diffuse signals show no correlation with the intensity of the sample's Bragg reflections except above T_2, where we interpret the correlated large hot diffuse signals and loss of sample reflections as evidence of melting.

The observed trends and suggested interpretation in this study mirror similar observations and interpretations for the high-temperature behavior of $Fe_{1-x}O$ at ambient pressure. Satellite reflections in $Fe_{1-x}O$ have been extensively studied at ambient pressure and consistently attributed to long-range ordered vacancy superstructures, while diffuse scattering has been commonly understood as long-range disorder and possible short-range clustering of defects (e.g., Welberry et al., 2014). In particular, the development of long-range vacancy structures at moderate temperatures and the transformation to a disordered state at high temperatures several hundred kelvin below melting have been suggested for $Fe_{1-x}O$ at ambient pressure (Hazen & Jeanloz, 1984) but never studied at high pressures. The findings in this study provide evidence for similar behavior at simultaneous high pressures and

temperatures.

5.4.3 Synchrotron Mössbauer measurements

We fit the Mössbauer integrated signal intensity versus temperature to constrain a melting temperature with high fit quality (Fig. 5.4, Table D.3). Fits are performed using the SIMX module in the software MINUTI (Sturhahn, 2021), which models the Lamb-Mössbauer factor and thus signal intensity as a function of temperature given various experiment-specific parameters: the sample's effective thickness at the start of the heating run, constrained from fits to the Mössbauer time spectra (Section 5.3.2), and the sizes and shapes of the x-ray beam and laser hotspot (Dobrosavljevic et al., 2022). Effective thickness is the dimensionless product of the numerical density of ^{57}Fe atoms, the physical thickness of the sample, the nuclear resonant cross-section ($2.56\text{x}10^{-22}$ m^2 for ^{57}Fe), and the Lamb-Mössbauer factor. Influence of the sample's effective thickness at the start of the heating run is discussed in previous SMS melting studies (Dobrosavljevic et al., 2022; Jackson et al., 2013; D. Zhang et al., 2016). The melting temperature is constrained by the fitting procedure, with uncertainties calculated as the root-mean-square of uncertainty from the fit and the average temperature uncertainty for each measurement. Changes in the sample chamber thickness, estimated from upstream and downstream ionization chambers monitoring total transmitted x-rays (Dobrosavljevic et al., 2022), never exceed 2% before the onset of melting.

5.4.4 *In-situ* pressure determination and thermal pressures

For the XRD heating runs, we determine *in-situ* pressures of the vacancy order-disorder and melting transitions for all heating runs by first fitting diffraction patterns collected at the onset of each transition (Section 5.3.1). From the refined unit-cell volumes of FeO and KCl, we calculate pressures of both materials using previously published thermal equations of state (Fischer, Campbell, Shofner, et al., 2011; Ono et al., 2007; Tateno et al., 2019). Transition pressures are calculated as the average of pressures given by the two materials, which consistently agree within 2-3 GPa (Tables D.1-D.2), with uncertainty estimated from the difference in the pressures and uncertainty in the equations of state. Using pressure calculations from ~160 patterns across four heating runs, we calculate thermal pressures for FeO and KCl as the difference of each hot pressure both from the pressure of its corresponding quenched measurement and from the quenched pressure at the start of the heating run. We fit each of the resulting four thermal pressure data sets to determine a linear

dependence of thermal pressure on temperature. We find good agreement between the two materials and the two calculation methods and note that larger scatter of FeO thermal pressures at high temperature are caused by the onset of the phase transitions (Fig. 5.5). We determine a thermal pressure model of 2.8 ± 0.2 GPa per 1000 K and apply it to predict the transition pressures in the SMS heating runs, using starting pressures from ruby fluorescence measurements (Shen et al., 2020) and a transition pressure uncertainty of 3 GPa.

5.4.5 Phase diagram of $Fe_{0.94}O$

We present a summary of all results from this study on melting temperatures and order-disorder transition temperatures for $Fe_{0.94}O$ in Figure 5.6 and Tables D.1-D.3. We find excellent agreement on melting temperatures between the XRD and SMS measurements within mutual uncertainties. We calculate a fit to all melting points using the Simon-Glatzel formulation (Simon & Glatzel, 1929)

$$T_m = T_{m0}\left(\frac{P_m - P_{m0}}{x} + 1\right)^y$$

where the melting points (T_m, P_m) are related to a reference melting point (T_{m0}, P_{m0}) and x, y are adjustable, material-specific fit parameters. With a fixed reference melting point of 1650 K at 0 GPa (Darken & Gurry, 1946; Lindsley, 1966; Shen et al., 1993), we use a weighted least squares method, where weights are calculated

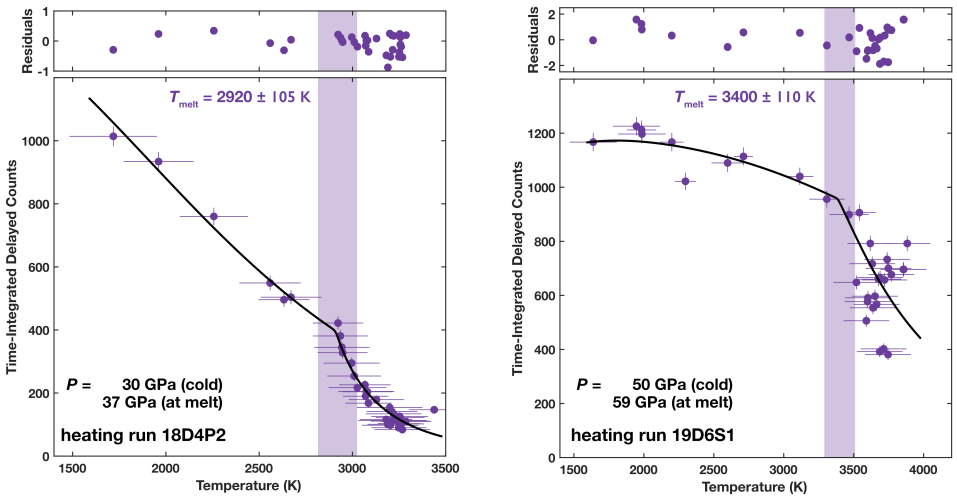

Figure 5.4: Two SMS heating runs showing Mössbauer signal intensity (time-integrated delayed counts) as a function of pressure. Fits to the data (solid black lines) constrain the melting temperature (shaded bar). Residuals are plotted in units of standard deviation.

as the squared inverse of the temperature uncertainty on each melting point, and find best-fit values x = 6.6 ± 2.3 and y = 0.30 ± 0.04. The resulting high-precision (R^2 = 0.98) melting curve constrains a melting temperature of 4140 ± 110 K for $Fe_{0.94}O$ at the core-mantle boundary pressure of 135.8 GPa. The uncertainties on melting curve temperatures (shaded bounds in Figure 5.6) are calculated as the root-mean-square of the uncertainty in the melting curve shape from the fit at the 1-σ level and the average temperature uncertainty for the melting points.

5.5 Discussion

5.5.1 Comparison to previous studies

The melting curve determined in this study agrees with melting temperatures reported by two previous experimental studies: low-pressure measurements by Lindsley (1966), using the sinking of iron particles through a molten wüstite sample to determine melting from quenched sample analysis, and a 50 GPa measurement by Seagle et al. (2008), using the disappearance of $B1$-FeO reflections in x-ray diffraction measurements on the Fe-FeO system. Agreement is also found with two previous studies that constructed melting curves using thermodynamic calculations of Gibbs free energies for solid and liquid states (Frost et al., 2010; Komabayashi,

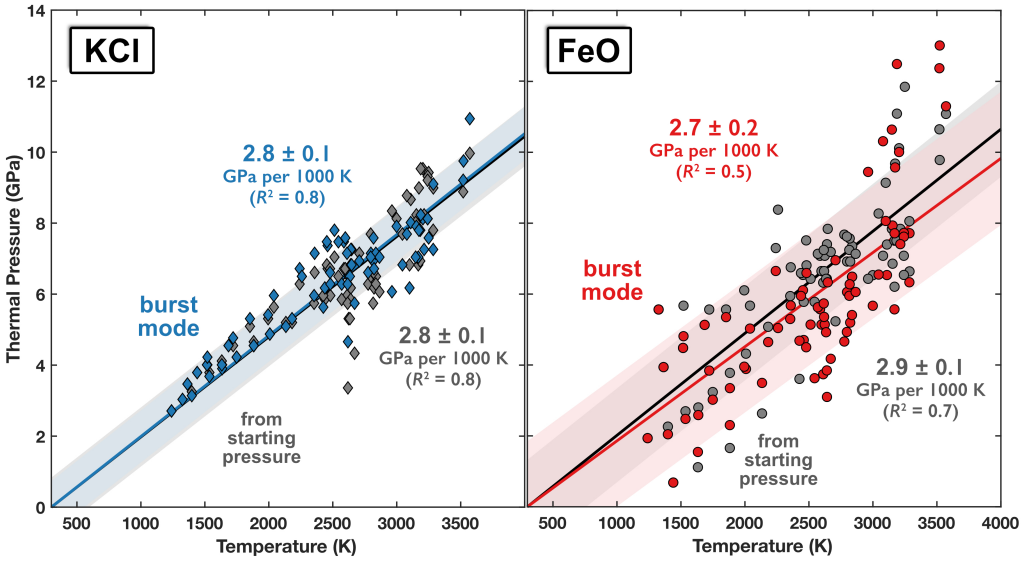

Figure 5.5: Thermal pressures from four representative XRD heating runs (starting 300 K pressures: 32 GPa, 59 GPa, 66 GPa, 86 GPa), calculated as described in Section 5.4.4.

2014). Our extrapolated melting curve shows compatibility with reports by Ozawa et al. (2011) of solid $B1$-$Fe_{0.96}O$ (up to 240 GPa and 4900 K). One experimental study using changes in quenched sample texture reported considerably higher melting temperatures for $Fe_{0.94}O$ with extreme (up to 1000 K) differences between the hottest solid and coolest liquid measurements (Knittle & Jeanloz, 1991b).

In contrast, three previous experimental studies reported lower melting temperatures (by ~350 K at 50 GPa), using visual observation of "fluid like motion" in sample surface texture ($Fe_{0.96}O$ – Boehler, 1992; $Fe_{0.94}O$ – Shen et al., 1993), and emissivity – temperature discontinuities ($Fe_{0.94}O$ – Fischer and Campbell, 2010). These techniques are sensitive to discontinuous changes in the sample's emissive properties during phase transitions but provide no structural information. We ob-

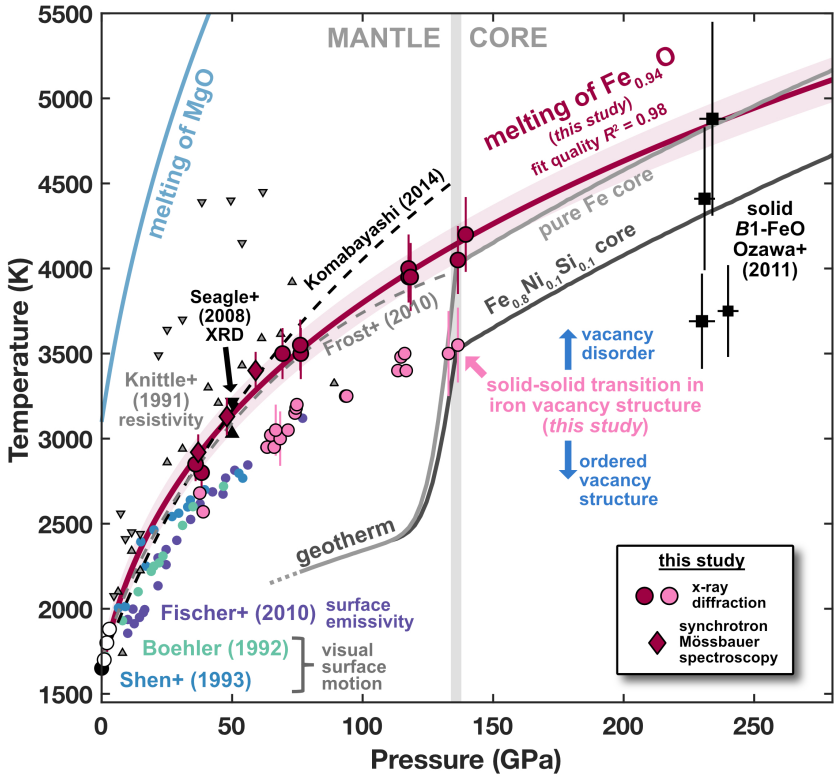

Figure 5.6: Phase diagram of $Fe_{0.94}O$. Crimson and pink points indicate melting and vacancy disorder transitions, respectively, measured in this study. Melting points for FeO from previous studies are shown with references indicated by labels. Core geotherms constructed from results by D. Zhang et al. (2016) and Dobrosavljevic et al. (2022). Mantle geotherm is from Wolf et al. (2015). Melting curve of MgO is from Kimura et al. (2017).

serve that the melting temperatures from these studies fall on the same trendline as the vacancy order-disorder transition determined in this study. We suggest the possibility that these studies in fact detected the order-disorder transition, rather than a signature of melting. In particular, in our study we generally observe plateaus in temperature – laser power profiles at the vacancy disorder transition, suggesting discontinuous changes in properties like sample absorptivity or heat capacity. Interestingly, Shen et al. (1993) reported larger changes in surface texture "several hundred degrees" above the initial small changes at the reported melting temperatures, and further observed typical melt textures in quenched samples only when quenching from the higher transition temperatures. The authors may have detected both the vacancy disorder and the melting transitions but assigned the former as the latter. In contrast, data shown by Fischer and Campbell (2010) suggest the samples may not have been heated to high enough temperatures to reach the melting temperatures measured in this study.

5.5.2 Geophysical implications

The melting curve determined in this study affects models of magma ocean crystallization (e.g., Boukaré et al., 2015; Miyazaki and Korenaga, 2019), which have relied on previous FeO melting temperature estimates (Fischer & Campbell, 2010) that were lower by ~350 K at 50 GPa and ~500 K at 136 GPa. Higher melting temperatures for FeO, the final end-member phase to crystallize during mantle solidification, imply a faster timescale for crystallization and the possibility of a fully solid present-day mantle. We evaluate this possibility and the viability of proposed solid FeO-rich ultralow velocity zones (ULVZs) at Earth's mantle base by comparing the updated FeO melting curve with CMB temperature estimates from previous work. Melting of FeO represents a lower bound on the solidus of the (Mg,Fe)O solid solution, as addition of magnesium should raise the melting temperature (Kimura et al., 2017; L. Zhang & Fei, 2008). Using core temperature profiles determined from recent melting studies of iron alloys using the same techniques as in this study (Dobrosavljevic et al., 2022; Jackson et al., 2013; D. Zhang et al., 2016), we see that the melting curve of iron predicts a CMB temperature of 4000 ± 200 K (D. Zhang et al., 2016) and represents a moderate value across the range of recently reported iron melting curves (reviewed by Dobrosavljevic et al., 2022). The presence of 10mol% each of nickel and silicon in the core, compatible with seismic constraints (Javoy et al., 2010; Morrison et al., 2018; Ricolleau et al., 2011), could lower the CMB temperature to 3500 K (Dobrosavljevic et al., 2022). The melting

temperature of FeO at the CMB (4140 ± 110 K from this study) falls well above these estimates, suggesting that FeO-rich ULVZs, such as those containing iron-rich (Mg,Fe)O, can exist as solid structures in the present-day lowermost mantle (Dobrosavljevic et al., 2019; Jackson & Thomas, 2021; Lai et al., 2022; Wicks et al., 2010). Given reports of high conductivity and possible metallic behavior for FeO (Ohta et al., 2012) and iron-rich (Mg,Fe)O (Ohta et al., 2014), such proposed solid FeO-rich ULVZs may exhibit higher bulk conductivity than the surrounding mantle (Knittle & Jeanloz, 1991a; Manga & Jeanloz, 1996). This could provide a mechanism for plume generation in the lowermost mantle without the need to invoke the hypothesis of partially molten ULVZs, as previously done to explain the seismic detection of ULVZs at the roots of major plumes (e.g., Yuan and Romanowicz, 2017). An elevated electrical conductivity for FeO-rich solid ULVZs relative to the surrounding mantle could also produce a heterogeneous conductive layer at the CMB as proposed to explain observations of nutations in Earth's rotation axis and decadal variations in the length of day (Buffett, 2015).

Chapter 6

CONCLUSION

In this thesis, I have used multi-technique experimental approaches and interdisciplinary collaboration to investigate Earth's heterogeneous core-mantle boundary region. Specifically, I studied compositions of ultralow velocity zones, the most extreme and perhaps least understood structures in the lowermost mantle, and measured the melting temperatures of core-forming and ULVZ-forming materials. Through this work, I demonstrated that the presence of solid iron-rich (Mg,Fe)O magnesiowüstite is compatible with seismic and geodynamic constraints on ULVZs, finding that partial melt is not a necessary explanation for these structures. As part of this effort, we developed a best-fit minimization approach for quantitative constraints on ULVZ compositions and applied our approach to a region underneath Hawai'i in collaboration with seismologists and geodynamicists.

I then investigated whether these proposed FeO-rich assemblages could indeed exist as solid chemically distinct structures in the lowermost mantle. To do so, I placed new constraints on the temperature of the core-mantle boundary region and on the melting temperature of FeO, the solidus phase of such assemblages. For these investigations, we developed a multi-technique approach for measuring melting and solid phase relations of iron-bearing materials, combining two *in-situ* synchrotron-based methods – synchrotron Mössbauer spectroscopy, sensitive to dynamics of the iron nuclei, and synchrotron x-ray diffraction, sensitive to average atomic positions. I applied this approach to $Fe_{0.8}Ni_{0.1}Si_{0.1}$, a proposed composition of Earth's core compatible with seismic constraints, and found that the presence of silicon reduces core temperatures by around 500 K, suggesting a CMB temperature of 3500 K. I further applied this approach to $Fe_{0.94}O$ and measured its melting temperature up to an outermost core pressure of 140 GPa, almost double the pressure range achieved in previous experiments. I determined a melting temperature of 4140 K at CMB pressure, giving strong support to the viability of solid FeO-rich ULVZ structures in the present-day lowermost mantle. These studies show excellent agreement in melting temperatures determined by the two independent techniques, giving insight into possible sources of large discrepancies in previous melting studies. I note that the ULVZ compositions constrained in Chapters 2 and 3 contain small amounts of magnesium in the (Mg,Fe)O solid solution, and that the addition of Mg is likely to

raise the melting temperature relative to the FeO end-member (Deng & Lee, 2017; Du et al., 2015), further supporting the likelihood that such proposed assemblages would be solid in the present-day lowermost mantle.

The work in this thesis further helps to identify a number of open questions and sources of uncertainty in the study of ultralow velocity zones and the core-mantle boundary. In quantifying viable compositions of ULVZs, we have shown that the dominant source of uncertainty lies in the rheological state of such proposed magnesiowüstite-bearing assemblages (see also Bower et al., 2011; Reali et al., 2019). Specifically, because the elastic moduli are so much lower for iron-rich (Mg,Fe)O relative to coexisting bridgmanite and calcium silicate perovskite, the Voigt and Reuss mixing bounds produce large differences in possible concentrations of magnesiowüstite for a given bulk velocity reduction (Dobrosavljevic et al., 2019; Lai et al., 2022; Wicks et al., 2017). This uncertainty cannot be reduced without improved knowledge of how stress and strain partition among the constituent phases in the assemblage, requiring experimental and theoretical efforts to address these challenges.

The rheology of the proposed assemblages has consequence not just for the bulk velocities of ULVZ but also for the distribution of the seismically slow magnesiowüstite phase within the assemblage. In particular, there may exist a critical concentration of magnesiowüstite above which the phase forms an interconnected network throughout the ULVZ structure, and below which the phase exists as isolated pockets. These may represent fundamentally different regimes for the bulk ULVZ, especially given reports of very high conductivities for FeO and iron-rich (Mg,Fe)O at lowermost mantle conditions (Ohta et al., 2014; Ohta et al., 2012). In that context, the possible interconnection of magnesiowüstite could have significant effect on the bulk transport properties of a ULVZ, with major implications for heterogeneous heat flow through the core-mantle boundary and for how plumes are generated and sustained in the lowermost mantle over geologic time. Exploring this possibility requires experimental study of transport properties, as well as more detailed theoretical investigations of the phase diagrams of FeO and iron-rich (Mg,Fe)O phases. To that end, the author has initiated an interdisciplinary collaboration with theoretical condensed matter physicists to apply advanced computational methods for studying high-pressure insulator-metal transitions in FeO and consequences for its transport properties at deep Earth conditions, the details of which are in progress and beyond the scope of this thesis.

This thesis has further highlighted the necessity of interdisciplinary study for advancing our understanding of highly inaccessible regions like the core-mantle boundary and poorly understood features like ultralow velocity zones. Placing further constraints on ULVZs, and investigating the possibility that ULVZs in fact represent multiple distinct phenomena in the lowermost mantle, will benefit from bringing in additional angles of investigation and types of data. Possibilities include further geodynamic study on the entrainment of material into plumes and consequences for geochemical signatures in ocean island basalts and large igneous provinces. In addition, the use of normal modes of the Earth may present a path forward for placing further constraints on lowermost mantle density, a property often difficult to precisely constrain through study of seismic body waves. Investigating the consequences of potentially highly conductive FeO in the lowermost mantle for heterogeneous heat flow out of the core and for Earth's magnetic field may provide further promising avenues of study.

In conclusion, many uncertainties remain regarding Earth's core-mantle boundary region and the heterogeneous structures across its complex landscape. At the same time, deep Earth science is rapidly progressing, with many exciting advances achieved every year in terms of high-pressure experimental capabilities, seismic observations, geodynamic simulations, and many other related areas of research. With these rapid advances, prospects for research on the deep interior over the next several decades look extremely promising and hold potential for major discoveries around basic Earth and planetary processes.

BIBLIOGRAPHY

Akahama, Y., & Kawamura, H. (2010). Pressure calibration of diamond anvil Raman gauge to 410 GPa. *Journal of Physics: Conference Series*, *215*. https://doi.org/10.1088/1742-6596/215/1/012195

Andrault, D., Pesce, G., Bouhifd, M. A., Bolfan-Casanova, N., Heńot, J. M., & Mezouar, M. (2014). Melting of subducted basalt at the core-mantle boundary. *Science*. https://doi.org/10.1126/science.1250466

Anzellini, S., Dewaele, A., Mezouar, M., Loubeyre, P., & Morard, G. (2013). Melting of iron at earth's inner core boundary based on fast X-ray diffraction. *Science*, *340*(6131), 464–466. https://doi.org/10.1126/science.1233514

Aquilanti, G., Trapananti, A., Karandikar, A., Kantor, I., Marini, C., Mathon, O., Pascarelli, S., & Boehler, R. (2015). Melting of iron determined by X-ray absorption spectroscopy to 100 GPa. *Proceedings of the National Academy of Sciences*, *112*(39), 12042–12045. https://doi.org/10.1073/pnas.1502363112

Asanuma, H., Ohtani, E., Sakai, T., Terasaki, H., Kamada, S., Kondo, T., & Kikegawa, T. (2010). Melting of iron–silicon alloy up to the core–mantle boundary pressure: implications to the thermal structure of the Earth's core. *Physics and Chemistry of Minerals*, *37*(6), 353–359. https://doi.org/10.1007/s00269-009-0338-7

Basu, A., Field, M. R., McCulloch, D. G., & Boehler, R. (2020). New measurement of melting and thermal conductivity of iron close to outer core conditions. *Geoscience Frontiers*, *11*(2), 565–568. https://doi.org/10.1016/j.gsf.2019.06.007

Berryman, J. G. (2000). Seismic velocity decrement ratios for regions of partial melt in the lower mantle. *Geophysical Research Letters*, *27*(3), 421–424. https://doi.org/10.1029/1999GL008402

Boehler, R. (1992). Melting of the FeFeO and the FeFeS systems at high pressure: Constraints on core temperatures. *Earth and Planetary Science Letters*, *111*(2-4), 217–227. https://doi.org/10.1016/0012-821X(92)90180-4

Boehler, R., Santamaría-Pérez, D., Errandonea, D., & Mezouar, M. (2008). Melting, density, and anisotropy of iron at core conditions: new x-ray measurements to 150 GPa. *Journal of Physics: Conference Series*, *121*(2), 022018. https://doi.org/10.1088/1742-6596/121/2/022018

Boukaré, C., Ricard, Y., Fiquet, G., Lyon, L. D. G. D., Lyon, U. D., Umr, C., Minéralogie, I. D., & Physique, D. (2015). Journal of Geophysical Research : Solid Earth Thermodynamics of the MgO-FeO-SiO 2 system up to 140 GPa : Application to the crystallization of Earth ' s magma ocean, 6085–6101. https://doi.org/10.1002/2015JB011929.Received

Bower, D. J., Gurnis, M., & Seton, M. (2013). Lower mantle structure from paleogeographically constrained dynamic Earth models. *Geochemistry, Geophysics, Geosystems*, *14*(1), 44–63. https://doi.org/10.1029/2012GC004267

Bower, D. J., Wicks, J. K., Gurnis, M., & Jackson, J. M. (2011). A geodynamic and mineral physics model of a solid-state ultralow-velocity zone. *Earth and Planetary Science Letters*, *303*(3-4), 193–202. https://doi.org/10.1016/j.epsl.2010.12.035

Brodholt, J., & Badro, J. (2017). Composition of the low seismic velocity E layer at the top of Earth's core. *Geophysical Research Letters*, *44*(16), 8303–8310. https://doi.org/10.1002/2017GL074261

Brown, S. P., Thorne, M. S., Miyagi, L., & Rost, S. (2015). A compositional origin to ultralow-velocity zones. *Geophysical Research Letters*, *42*(4), 1039–1045. https://doi.org/10.1002/2014GL062097

Buffet, B. A., Edward, J., & Jeanloz, R. (2000). Sediments at the top of the Earth ' s core What is a sediment ? *Science*, *668*(1151), 1338–1343.

Buffett, B. (2015). Core–Mantle Interactions. *Treatise on geophysics* (pp. 213–224). Elsevier. https://doi.org/10.1016/B978-0-444-53802-4.00148-2

Campbell, A. J., Danielson, L., Righter, K., Seagle, C. T., Wang, Y., & Prakapenka, V. B. (2009). High pressure effects on the iron–iron oxide and nickel–nickel oxide oxygen fugacity buffers. *Earth and Planetary Science Letters*, *286*(3-4), 556–564. https://doi.org/10.1016/j.epsl.2009.07.022

Caracas, R., & Cohen, R. E. (2006). Theoretical determination of the Raman spectra of MgSiO 3 perovskite and post-perovskite at high pressure. *Geophysical Research Letters*, *33*(12), L12S05. https://doi.org/10.1029/2006GL025736

Chandler, B., Bernier, J., Diamond, M., Kunz, M., & Wenk, H.-R. (2021). Exploring microstructures in lower mantle mineral assemblages with synchrotron x-rays. *Science Advances*, *7*(1), eabd3614. https://doi.org/10.1126/sciadv.abd3614

Chen, B., Jackson, J. M., Sturhahn, W., Zhang, D., Zhao, J., Wicks, J. K., & Murphy, C. A. (2012). Spin crossover equation of state and sound velocities of (Mg 0.65Fe0.35)O ferropericlase to 140 GPa. *Journal of Geophysical Research: Solid Earth*, *117*(8), 1–9. https://doi.org/10.1029/2012JB009162

Chen, T. K., Chang, C. C., Chang, H. H., Fang, A. H., Wang, C. H., Chao, W. H., Tseng, C. M., Lee, Y. C., Wu, Y. R., Wen, M. H., Tang, H. Y., Chen, F. R., Wang, M. J., Wu, M. K., & Van Dyck, D. (2014). Fe-vacancy order and superconductivity in tetragonal -Fe 1-xSe. *Proceedings of the National Academy of Sciences of the United States of America*, *111*(1), 63–68. https://doi.org/10.1073/pnas.1321160111

Cobden, L., Thomas, C., & Trampert, J. (2015). Seismic detection of post-perovskite inside the earth. *The earth's heterogeneous mantle: A geophysical, geodynamical, and geochemical perspective* (pp. 391–440). https://doi.org/10.1007/978-3-319-15627-9_13

Coppari, F., Smith, R. F., Wang, J., Millot, M., Kim, D., Rygg, J. R., Hamel, S., Eggert, J. H., & Duffy, T. S. (2021). Implications of the iron oxide phase transition on the interiors of rocky exoplanets. *Nature Geoscience*, *14*(3), 121–126. https://doi.org/10.1038/s41561-020-00684-y

Dannberg, J., Myhill, R., Gassmöller, R., & Cottaar, S. (2021). The morphology, evolution and seismic visibility of partial melt at the core-mantle boundary: Implications for ULVZs. *Geophysical Journal International*, 1028–1059. https://doi.org/10.1093/gji/ggab242

Darken, L. S., & Gurry, R. W. (1946). The System Iron—Oxygen. II. Equilibrium and Thermodynamics of Liquid Oxide and Other Phases. *Journal of the American Chemical Society*, *68*(5), 798–816. https://doi.org/10.1021/ja01209a030

Deng, J., & Lee, K. K. (2017). Viscosity jump in the lower mantle inferred from melting curves of ferropericlase. *Nature Communications*, *8*(1). https://doi.org/10.1038/s41467-017-02263-z

Dewaele, A., Datchi, F., Loubeyre, P., & Mezouar, M. (2008). High pressure-high temperature equations of state of neon and diamond. *Physical Review B - Condensed Matter and Materials Physics*, *77*(9). https://doi.org/10.1103/PhysRevB.77.094106

Dobrosavljevic, V. V., Sturhahn, W., & Jackson, J. M. (2019). Evaluating the Role of Iron-Rich (Mg,Fe)O in Ultralow Velocity Zones. *Minerals*, *9*(12), 762. https://doi.org/10.3390/min9120762

Dobrosavljevic, V. V., Zhang, D., Sturhahn, W., Zhao, J., Toellner, T. S., Chariton, S., Prakapenka, V. B., Pardo, O. S., & Jackson, J. M. (2022). Melting and phase relations of Fe-Ni-Si determined by a multi-technique approach. *Earth and Planetary Science Letters*, *584*, 117358. https://doi.org/10.1016/j.epsl.2021.117358

Dobson, D. P., & Brodholt, J. P. (2005). Subducted banded iron formations as a source of ultralow-velocity zones at the core-mantle boundary. *Nature*, *434*(7031), 371–374. https://doi.org/10.1038/nature03430

Dorfman, S. M., Meng, Y., Prakapenka, V. B., & Duffy, T. S. (2013). Effects of Fe-enrichment on the equation of state and stability of (Mg,Fe)SiO3 perovskite. *Earth and Planetary Science Letters*, *361*, 249–257. https://doi.org/10.1016/j.epsl.2012.10.033

Dorfman, S. M., Nabiei, F., Boukaré, C. E., Prakapenka, V. B., Cantoni, M., Badro, J., & Gillet, P. (2021). Composition and pressure effects on partitioning of ferrous iron in iron-rich lower mantle heterogeneities. *Minerals*, *11*(5), 1–20. https://doi.org/10.3390/min11050512

Du, Z., Gu, T., Dobrosavljevic, V., Weir, S. T., Falabella, S., & Lee, K. K. (2015). Using stepped anvils to make even insulation layers in laser-heated diamond-anvil cell samples. *Review of Scientific Instruments*, *86*(9), 095103. https://doi.org/10.1063/1.4929667

Duffy, T. S., & Anderson, D. L. (1989). Seismic velocities in mantle minerals and the mineralogy of the upper mantle. *Journal of Geophysical Research*, *94*(B2), 1895–1912. https://doi.org/10.1029/JB094iB02p01895

Dziewonski, A. M., & Anderson, D. L. (1981). Preliminary reference Earth model. *Physics of the Earth and Planetary Interiors*, *25*(4), 297–356. https://doi.org/10.1016/0031-9201(81)90046-7

Edmund, E., Miozzi, F., Morard, G., Boulard, E., Clark, A., Decremps, F., Garbarino, G., Svitlyk, V., Mezouar, M., & Antonangeli, D. (2020). Axial Compressibility and Thermal Equation of State of Hcp Fe–5wt% Ni–5wt% Si. *Minerals*, *10*(2), 98. https://doi.org/10.3390/min10020098

Fang, Y., Xie, D. H., Zhang, W., Chen, F., Feng, W., Xie, B. P., Feng, D. L., Lai, X. C., & Tan, S. Y. (2016). Tunable Fe-vacancy disorder-order transition in FeSe thin films. *Physical Review B*, *93*(18), 1–7. https://doi.org/10.1103/PhysRevB.93.184503

Fei, Y., Ricolleau, A., Frank, M., Mibe, K., Shen, G., & Prakapenka, V. (2007). Toward an internally consistent pressure scale. *Proceedings of the National Academy of Sciences*, *104*(22), 9182–9186. https://doi.org/10.1073/pnas.0609013104

Fender, B., & Riley, F. (1969). Thermodynamic properties of Fe1xO. Transitions in the single phase region. *Journal of Physics and Chemistry of Solids*, *30*(4), 793–798. https://doi.org/10.1016/0022-3697(69)90273-X

Finkelstein, G. J., Jackson, J. M., Said, A., Alatas, A., Leu, B. M., Sturhahn, W., & Toellner, T. S. (2018). Strongly Anisotropic Magnesiowüstite in Earth's Lower Mantle. *Journal of Geophysical Research: Solid Earth*, *123*(6), 4740–4750. https://doi.org/10.1029/2017JB015349

Finkelstein, G. J., Jackson, J. M., Sturhahn, W., Zhang, D., Ercan Alp, E., & Toellner, T. S. (2017). Single-crystal equations of state of magnesiowüstite at high pressures. *American Mineralogist*, *102*(8), 1709–1717. https://doi.org/10.2138/am-2017-5966

Fischer, R. A. (2016). Melting of Fe Alloys and the Thermal Structure of the Core. https://doi.org/https://doi.org/10.1002/9781118992487.ch1 https://doi.org/10.1002/9781118992487.ch1

Fischer, R. A., & Campbell, A. J. (2010). High-pressure melting of wustite. *American Mineralogist*, *95*(10), 1473–1477. https://doi.org/10.2138/am.2010.3463

Fischer, R. A., Campbell, A. J., Caracas, R., Reaman, D. M., Dera, P., & Prakapenka, V. B. (2012). Equation of state and phase diagram of Fe–16Si alloy as a candidate component of Earth's core. *Earth and Planetary Science Letters*, *357-358*, 268–276. https://doi.org/10.1016/j.epsl.2012.09.022

Fischer, R. A., Campbell, A. J., Lord, O. T., Shofner, G. A., Dera, P., & Prakapenka, V. B. (2011). Phase transition and metallization of FeO at high pressures and temperatures. *Geophysical Research Letters*, *38*(24), n/a–n/a. https://doi.org/10.1029/2011GL049800

Fischer, R. A., Campbell, A. J., Reaman, D. M., Miller, N. A., Heinz, D. L., Dera, P., & Prakapenka, V. B. (2013). Phase relations in the Fe–FeSi system at high pressures and temperatures. *Earth and Planetary Science Letters*, *373*, 54–64. https://doi.org/10.1016/j.epsl.2013.04.035

Fischer, R. A., Campbell, A. J., Shofner, G. A., Lord, O. T., Dera, P., & Prakapenka, V. B. (2011). Equation of state and phase diagram of FeO. *Earth and Planetary Science Letters*, *304*(3-4), 496–502. https://doi.org/10.1016/j.epsl.2011.02.025

French, S. W., & Romanowicz, B. (2015). Broad plumes rooted at the base of the Earth's mantle beneath major hotspots. *Nature*, *525*(7567), 95–99. https://doi.org/10.1038/nature14876

Frost, D. J., Asahara, Y., Rubie, D. C., Miyajima, N., Dubrovinsky, L. S., Holzapfel, C., Ohtani, E., Miyahara, M., & Sakai, T. (2010). Partitioning of oxygen between the Earth's mantle and core. *Journal of Geophysical Research*, *115*(B2), B02202. https://doi.org/10.1029/2009JB006302

Garnero, E. J., & Helmberger, D. V. (1998). Further structural constraints and uncertainties of a thin laterally varying ultralow-velocity layer at the base of the mantle. *Journal of Geophysical Research: Solid Earth*, *103*(B6), 12495–12509. https://doi.org/10.1029/98JB00700

Gavarri, J.-R., & Carel, C. (2019). The complex nonstoichiometry of wüstite Fe1-O: Review and comments. *Progress in Solid State Chemistry*, *53*(October), 27–49. https://doi.org/10.1016/j.progsolidstchem.2018.10.001

Geballe, Z. M., & Jeanloz, R. (2012). Origin of temperature plateaus in laser-heated diamond anvil cell experiments. *Journal of Applied Physics*, *111*(12), 123518. https://doi.org/10.1063/1.4729905

Gréaux, S., Irifune, T., Higo, Y., Tange, Y., Arimoto, T., Liu, Z., & Yamada, A. (2019). Sound velocity of CaSiO3 perovskite suggests the presence of basaltic crust in the Earth's lower mantle. *Nature*, *565*(7738), 218–221. https://doi.org/10.1038/s41586-018-0816-5

Gülcher, A. J. P., Ballmer, M. D., & Tackley, P. J. (2020). Coupled dynamics and evolution of primordial and recycled heterogeneity in Earth's lower mantle. *Solid Earth Discussions*, 1–43. https://doi.org/10.5194/se-2020-205

Gurnis, M. (1988). Large-scale mantle convection and the aggregation and dispersal of supercontinents. *Nature*, *332*(6166), 695–699. https://doi.org/10.1038/332695a0

Hassan, R., Müller, R. D., Gurnis, M., Williams, S. E., & Flament, N. (2016). A rapid burst in hotspot motion through the interaction of tectonics and deep mantle flow. *Nature*, *533*(7602), 239–242. https://doi.org/10.1038/nature17422

Hazen, R. M., & Jeanloz, R. (1984). Wüstite (Fe 1-x O): A review of its defect structure and physical properties. *Reviews of Geophysics*, *22*(1), 37. https://doi.org/10.1029/RG022i001p00037

He, Y., & Wen, L. (2012). Geographic boundary of the "Pacific Anomaly" and its geometry and transitional structure in the north. *Journal of Geophysical Research: Solid Earth*, *117*(B9), 1–16. https://doi.org/10.1029/2012JB009436

Hernlund, J. W., & Jellinek, A. M. (2010). Dynamics and structure of a stirred partially molten ultralow-velocity zone. *Earth and Planetary Science Letters*, *296*(1-2), 1–8. https://doi.org/10.1016/j.epsl.2010.04.027

Hernlund, J. W., & Tackley, P. J. (2007). Some dynamical consequences of partial melting in Earth's deep mantle. *Physics of the Earth and Planetary Interiors*, *162*(1-2), 149–163. https://doi.org/10.1016/j.pepi.2007.04.005

Hin, R. C., Fitoussi, C., Schmidt, M. W., & Bourdon, B. (2014). Experimental determination of the Si isotope fractionation factor between liquid metal and liquid silicate. *Earth and Planetary Science Letters*, *387*, 55–66. https://doi.org/10.1016/j.epsl.2013.11.016

Hirose, K., Labrosse, S., & Hernlund, J. (2013). Composition and State of the Core. *Annual Review of Earth and Planetary Sciences*, *41*(1), 657–691. https://doi.org/10.1146/annurev-earth-050212-124007

Hirose, K., Sinmyo, R., & Hernlund, J. (2017). Perovskite in Earth's deep interior. *Science*, *358*(6364), 734–738. https://doi.org/10.1126/science.aam8561

Hoffman, P. F., Kaufman, A. J., Halverson, G. P., & Schrag, D. P. (1998). A Neoproterozoic Snowball Earth. *Science*, *281*(5381), 1342–1346. https://doi.org/10.1126/science.281.5381.1342

Holland, H. D. (2002). Volcanic gases, black smokers, and the great oxidation event. *Geochimica et Cosmochimica Acta*, *66*(21), 3811–3826. https://doi.org/10.1016/S0016-7037(02)00950-X

Hosseini, K., Sigloch, K., Tsekhmistrenko, M., Zaheri, A., Nissen-Meyer, T., & Igel, H. (2020). Global mantle structure from multifrequency tomography using P, PP and P-diffracted waves. *Geophysical Journal International*, *220*(1), 96–141. https://doi.org/10.1093/gji/ggz394

Hou, M., Liu, J., Zhang, Y., Du, X., Dong, H., Yan, L., Wang, J., Wang, L., & Chen, B. (2021). Melting of Iron Explored by Electrical Resistance Jump up to 135 GPa. *Geophysical Research Letters*, *48*(20), 1–10. https://doi.org/10.1029/2021GL095739

Hu, J., Gurnis, M., Rudi, J., Stadler, G., & Müller, R. D. (2022). Dynamics of the abrupt change in Pacific Plate motion around 50 million years ago. *Nature Geoscience*, *15*(1), 74–78. https://doi.org/10.1038/s41561-021-00862-6

Jackson, J. M., Sturhahn, W., Lerche, M., Zhao, J., Toellner, T. S., Alp, E. E., Sinogeikin, S. V., Bass, J. D., Murphy, C. A., & Wicks, J. K. (2013). Melting of compressed iron by monitoring atomic dynamics. *Earth and Planetary Science Letters*, *362*, 143–150. https://doi.org/10.1016/j.epsl.2012.11.048

Jackson, J. M., & Thomas, C. (2021). Seismic and Mineral Physics Constraints on the D Layer. https://doi.org/10.1002/9781119528609.ch8

Jacobsen, S. D., Lin, J.-F., Angel, R. J., Shen, G., Prakapenka, V. B., Dera, P., Mao, H.-k., & Hemley, R. J. (2005). Single-crystal synchrotron X-ray diffraction study of wüstite and magnesiowüstite at lower-mantle pressures. *Journal of Synchrotron Radiation*, *12*(5), 577–583. https://doi.org/10.1107/S0909049505022326

Javoy, M., Kaminski, E., Guyot, F., Andrault, D., Sanloup, C., Moreira, M., Labrosse, S., Jambon, A., Agrinier, P., Davaille, A., & Jaupart, C. (2010). The chemical composition of the Earth: Enstatite chondrite models. *Earth and Planetary Science Letters*, *293*(3-4), 259–268. https://doi.org/10.1016/j.epsl.2010.02.033

Jellinek, A. M., & Manga, M. (2002). The influence of a chemical boundary layer on the fixity, spacing and lifetime of mantle plumes. *Nature*, *418*(6899), 760–763. https://doi.org/10.1038/nature00979

Jellinek, A. M., & Manga, M. (2004). Links between long-lived hot spots, mantle plumes, D, and plate tectonics. *Reviews of Geophysics*, *42*(3), 1–35. https://doi.org/10.1029/2003RG000144

Jenkins, J., Mousavi, S., Li, Z., & Cottaar, S. (2021). A high-resolution map of Hawaiian ULVZ morphology from ScS phases. *Earth and Planetary Science Letters*, *563*, 116885. https://doi.org/10.1016/j.epsl.2021.116885

Kimura, T., Ohfuji, H., Nishi, M., & Irifune, T. (2017). Melting temperatures of MgO under high pressure by micro-texture analysis. *Nature Communications*, *8*(1), 15735. https://doi.org/10.1038/ncomms15735

Knibbe, J. S., Rivoldini, A., Luginbuhl, S. M., Namur, O., Charlier, B., Mezouar, M., Sifre, D., Berndt, J., Kono, Y., Neuville, D. R., van Westrenen, W., & Van Hoolst, T. (2021). Mercury's Interior Structure Constrained by Density and P-Wave Velocity Measurements of Liquid Fe-Si-C Alloys. *Journal of Geophysical Research: Planets*, *126*(1), 1–26. https://doi.org/10.1029/2020JE006651

Knibbe, J. S., & van Westrenen, W. (2018). The thermal evolution of Mercury's Fe–Si core. *Earth and Planetary Science Letters*, *482*, 147–159. https://doi.org/10.1016/j.epsl.2017.11.006

Knittle, E., & Jeanloz, R. (1991a). Earth's Core-Mantle Boundary: Results of Experiments at High Pressures and Temperatures. *Science*, *251*(5000), 1438–1443. https://doi.org/10.1126/science.251.5000.1438

Knittle, E., & Jeanloz, R. (1991b). The high-pressure phase diagram of Fe 0.94 O: A possible constituent of the Earth's core. *Journal of Geophysical Research*, *96*(B10), 16169. https://doi.org/10.1029/90JB00653

Koch, F., & Cohen, J. B. (1969). The defect structure of Fe1xO. *Acta Crystallographica Section B Structural Crystallography and Crystal Chemistry*, *25*(2), 275–287. https://doi.org/10.1107/s0567740869002111

Komabayashi, T. (2014). Thermodynamics of melting relations in the system Fe-FeO at high pressure: Implications for oxygen in the Earth's core. *Journal of Geophysical Research: Solid Earth*, *119*(5), 4164–4177. https://doi.org/10.1002/2014JB010980

Komabayashi, T., Fei, Y., Meng, Y., & Prakapenka, V. (2009). In-situ X-ray diffraction measurements of the γ-ϵ transition boundary of iron in an internally-heated diamond anvil cell. *Earth and Planetary Science Letters*, *282*(1-4), 252–257. https://doi.org/10.1016/j.epsl.2009.03.025

Komabayashi, T., Hirose, K., & Ohishi, Y. (2012). In situ X-ray diffraction measurements of the fcc–hcp phase transition boundary of an Fe–Ni alloy in an internally heated diamond anvil cell. *Physics and Chemistry of Minerals*, *39*(4), 329–338. https://doi.org/10.1007/s00269-012-0490-3

Komabayashi, T., Pesce, G., Morard, G., Antonangeli, D., Sinmyo, R., & Mezouar, M. (2019). Phase transition boundary between fcc and hcp structures in Fe-Si alloy and its implications for terrestrial planetary cores. *American Mineralogist*, *104*(1), 94–99. https://doi.org/10.2138/am-2019-6636

Komabayashi, T., Pesce, G., Sinmyo, R., Kawazoe, T., Breton, H., Shimoyama, Y., Glazyrin, K., Konôpková, Z., & Mezouar, M. (2019). Phase relations in the system Fe–Ni–Si to 200 GPa and 3900 K and implications for Earth's core. *Earth and Planetary Science Letters*, *512*, 83–88. https://doi.org/10.1016/j.epsl.2019.01.056

Kopp, R. E., Kirschvink, J. L., Hilburn, I. A., & Nash, C. Z. (2005). The Paleoproterozoic snowball Earth: A climate disaster triggered by the evolution of oxygenic photosynthesis. *Proceedings of the National Academy of Sciences*, *102*(32), 11131–11136. https://doi.org/10.1073/pnas.0504878102

Koppers, A. A. P., Becker, T. W., Jackson, M. G., Konrad, K., Müller, R. D., Romanowicz, B., Steinberger, B., & Whittaker, J. M. (2021). Mantle plumes and their role in Earth processes. *Nature Reviews Earth Environment*, *2*(6), 382–401. https://doi.org/10.1038/s43017-021-00168-6

Koulialias, D., Schawe, J. E., Löffler, J. F., & Gehring, A. U. (2021). Structural relaxation in layered, non-stoichiometric Fe7S8. *Physical Chemistry Chemical Physics*, *23*(2), 1165–1171. https://doi.org/10.1039/d0cp04445h

Krier, J., Thorne, M. S., Leng, K., & Nissen-Meyer, T. (2021). A Compositional Component to the Samoa Ultralow-Velocity Zone Revealed Through 2- and 3-D Waveform Modeling of SKS and SKKS Differential Travel-Times and Amplitudes. *Journal of Geophysical Research: Solid Earth*, *126*(7), 1–20. https://doi.org/10.1029/2021JB021897

Kuwayama, Y., Morard, G., Nakajima, Y., Hirose, K., Baron, A. Q., Kawaguchi, S. I., Tsuchiya, T., Ishikawa, D., Hirao, N., & Ohishi, Y. (2020). Equation of State of Liquid Iron under Extreme Conditions. *Physical Review Letters*, *124*(16), 165701. https://doi.org/10.1103/PhysRevLett.124.165701

Labrosse, S., Hernlund, J. W., & Coltice, N. (2007). A crystallizing dense magma ocean at the base of the Earth's mantle. *Nature*, *450*(7171), 866–869. https://doi.org/10.1038/nature06355

Labrosse, S., Poirier, J. P., & Le Mouël, J. L. (2001). The age of the inner core. *Earth and Planetary Science Letters*, *190*(3-4), 111–123. https://doi.org/10.1016/S0012-821X(01)00387-9

Lai, V. H., Helmberger, D. V., Dobrosavljevic, V. V., Wu, W., Sun, D., Jackson, J. M., & Gurnis, M. (2022). Strong ULVZ and Slab Interaction at the Northeastern Edge of the Pacific LLSVP Favors Plume Generation. *Geochemistry, Geophysics, Geosystems*, *23*(2). https://doi.org/10.1029/2021GC010020

Lay, T. (2015). Deep Earth Structure: Lower Mantle and D. *Treatise on geophysics: Second edition* (pp. 683–723). https://doi.org/10.1016/B978-0-444-53802-4.00019-1

Lay, T., & Helmberger, D. V. (1983). A lower mantle S-wave triplication and the shear velocity structure of D. *Geophysical Journal of the Royal Astronomical Society*, *75*(3), 799–837. https://doi.org/10.1111/j.1365-246X.1983.tb05010.x

Lay, T., Hernlund, J., & Buffett, B. A. (2008). Core-mantle boundary heat flow. *Nature Geoscience*, *1*(1), 25–32. https://doi.org/10.1038/ngeo.2007.44

Lay, T., Hernlund, J., Garnero, E. J., & Thorne, M. S. (2006). A Post-Perovskite Lens and D" Heat Flux Beneath the Central Pacific. *Science*, *314*(5803), 1272–1276. https://doi.org/10.1126/science.1133280

Li, B., & Zhang, J. (2005). Pressure and temperature dependence of elastic wave velocity of MgSiO3 perovskite and the composition of the lower mantle. *Physics of the Earth and Planetary Interiors*, *151*(1-2), 143–154. https://doi.org/10.1016/j.pepi.2005.02.004

Li, M. (2020). The Formation of Hot Thermal Anomalies in Cold Subduction-Influenced Regions of Earth's Lowermost Mantle. *Journal of Geophysical Research: Solid Earth*, *125*(6), 1–23. https://doi.org/10.1029/2019JB019312

Li, M., McNamara, A. K., Garnero, E. J., & Yu, S. (2017). Compositionally-distinct ultra-low velocity zones on Earth's core-mantle boundary. *Nature Communications*, *8*(1). https://doi.org/10.1038/s41467-017-00219-x

Lin, J. F., Sturhahn, W., Zhao, J., Shen, G., Mao, H. K., & Hemley, R. J. (2004). Absolute temperature measurement in a laser-heated diamond anvil cell. *Geophysical Research Letters*, *31*(14), L14611. https://doi.org/10.1029/2004GL020599

Lindsley, D. H. (1966). Pressure-temperature relations in the system FeO-SiO2. *Year Book Carnegie Inst. Washington*, 226–230.

Liu, J., Li, J., Hrubiak, R., & Smith, J. S. (2016). Origins of ultralow velocity zones through slab-derived metallic melt. *Proceedings of the National Academy of Sciences*, *113*(20), 5547–5551. https://doi.org/10.1073/pnas.1519540113

Liu, J., Hu, Q., Bi, W., Yang, L., Xiao, Y., Chow, P., Meng, Y., Prakapenka, V. B., Mao, H.-K., & Mao, W. L. (2019). Altered chemistry of oxygen and iron under deep Earth conditions. *Nature Communications*, *10*(1), 153. https://doi.org/10.1038/s41467-018-08071-3

Liu, J., Hu, Q., Young Kim, D., Wu, Z., Wang, W., Xiao, Y., Chow, P., Meng, Y., Prakapenka, V. B., Mao, H.-K., & Mao, W. L. (2017). Hydrogen-bearing iron peroxide and the origin of ultralow-velocity zones. *Nature*, *551*(7681), 494–497. https://doi.org/10.1038/nature24461

Lord, O. T., Walter, M. J., Dobson, D. P., Armstrong, L., Clark, S. M., & Kleppe, A. (2010). The FeSi phase diagram to 150 GPa. *Journal of Geophysical Research*, *115*(B6), B06208. https://doi.org/10.1029/2009JB006528

Lyubetskaya, T., & Korenaga, J. (2007). Chemical composition of Earth's primitive mantle and its variance: 1. Method and results. *Journal of Geophysical Research: Solid Earth*, *112*(3), 1–21. https://doi.org/10.1029/2005JB004223

Manenc, J. (1968). Structure du protoxyde de fer, résultats récents. *Bulletin de la Société française de Minéralogie et de Cristallographie*, *91*(6), 594–599. https://doi.org/10.3406/bulmi.1968.6160

Manga, M., & Jeanloz, R. (1996). Implications of a metal-bearing chemical boundary layer in D" for mantle dynamics. *Geophysical Research Letters*, *23*(22), 3091–3094. https://doi.org/10.1029/96GL03021

Mao, H.-k., & Mao, W. L. (2020). Key problems of the four-dimensional Earth system. *Matter and Radiation at Extremes*, *5*(3), 038102. https://doi.org/10.1063/1.5139023

Mao, H.-k., Shu, J., Fei, Y., Hu, J., & Hemley, R. J. (1996). The wüstite enigma. *Physics of the Earth and Planetary Interiors*, *96*(2-3), 135–145. https://doi.org/10.1016/0031-9201(96)03146-9

Mao, W. L., Mao, H. K., Sturhahn, W., Zhao, J., Prakapenka, V. B., Meng, Y., Shu, J., Fei, Y., & Hemley, R. J. (2006). Iron-rich post-perovskite and the origin of ultralow-velocity zones. *Science*, *312*(5773), 564–565. https://doi.org/10.1126/science.1123442

Matas, J., Bass, J., Ricard, Y., Mattern, E., & Bukowinski, M. S. (2007). On the bulk composition of the lower mantle: Predictions and limitations from generalized inversion of radial seismic profiles. *Geophysical Journal International*. https://doi.org/10.1111/j.1365-246X.2007.03454.x

Mavko, G., Mukerji, T., & Dvorkin, J. (2010). *The rock physics handbook*. Cambridge University Press.

McCammon, C. A., & Liu, L.-g. (1984). The effects of pressure and temperature on nonstoichiometric wstite, FexO: The iron-rich phase boundary. *Physics and Chemistry of Minerals*, *10*(3), 106–113. https://doi.org/10.1007/BF00309644

McDonough, W., & Sun, S.-s. (1995). The composition of the Earth. *Chemical Geology*, *120*(3-4), 223–253. https://doi.org/10.1016/0009-2541(94)00140-4

McKenzie, D. P., & Parker, R. L. (1967). The North Pacific: an Example of Tectonics on a Sphere. *Nature*, *216*(5122), 1276–1280. https://doi.org/10.1038/2161276a0

McNamara, A. K. (2019). A review of large low shear velocity provinces and ultra low velocity zones. *Tectonophysics*, *760*(April), 199–220. https://doi.org/10.1016/j.tecto.2018.04.015

McNamara, A. K., Garnero, E. J., & Rost, S. (2010). Tracking deep mantle reservoirs with ultra-low velocity zones. *Earth and Planetary Science Letters*, *299*(1-2), 1–9. https://doi.org/10.1016/j.epsl.2010.07.042

McQueen, T. M., Huang, Q., Ksenofontov, V., Felser, C., Xu, Q., Zandbergen, H., Hor, Y. S., Allred, J., Williams, A. J., Qu, D., Checkelsky, J., Ong, N. P., & Cava, R. J. (2009). Extreme sensitivity of superconductivity to stoichiometry in Fe1+δ Se. *Physical Review B - Condensed Matter and Materials Physics*, *79*(1), 1–7. https://doi.org/10.1103/PhysRevB.79.014522

Mitchell, R. N., Zhang, N., Salminen, J., Liu, Y., Spencer, C. J., Steinberger, B., Murphy, J. B., & Li, Z. X. (2021). The supercontinent cycle. *Nature Reviews Earth and Environment*, *2*(5), 358–374. https://doi.org/10.1038/s43017-021-00160-0

Miyazaki, Y., & Korenaga, J. (2019). On the Timescale of Magma Ocean Solidification and Its Chemical Consequences: 2. Compositional Differentiation Under Crystal Accumulation and Matrix Compaction. *Journal of Geophysical Research: Solid Earth*, *124*(4), 3399–3419. https://doi.org/10.1029/2018JB016928

Morard, G., Andrault, D., Guignot, N., Siebert, J., Garbarino, G., & Antonangeli, D. (2011). Melting of Fe–Ni–Si and Fe–Ni–S alloys at megabar pressures: implications for the core–mantle boundary temperature. *Physics and Chemistry of Minerals*, *38*(10), 767–776. https://doi.org/10.1007/s00269-011-0449-9

Morard, G., Boccato, S., Rosa, A. D., Anzellini, S., Miozzi, F., Henry, L., Garbarino, G., Mezouar, M., Harmand, M., Guyot, F., Boulard, E., Kantor, I., Irifune, T., & Torchio, R. (2018). Solving Controversies on the Iron Phase Diagram Under High Pressure. *Geophysical Research Letters*, *45*(20), 11, 074–11, 082. https://doi.org/10.1029/2018GL079950

Morrison, R. A., Jackson, J. M., Sturhahn, W., Zhang, D., & Greenberg, E. (2018). Equations of State and Anisotropy of Fe-Ni-Si Alloys. *Journal of Geophysical Research: Solid Earth*, *123*(6), 4647–4675. https://doi.org/10.1029/2017JB015343

Morrison, R. A., Jackson, J. M., Sturhahn, W., Zhao, J., & Toellner, T. S. (2019). High pressure thermoelasticity and sound velocities of Fe-Ni-Si alloys. *Physics of the Earth and Planetary Interiors*, *294*(October 2018), 106268. https://doi.org/10.1016/j.pepi.2019.05.011

Murphy, C. A., Jackson, J. M., Sturhahn, W., & Chen, B. (2011). Melting and thermal pressure of hcp-Fe from the phonon density of states. *Physics of the Earth and Planetary Interiors*, *188*(1-2), 114–120. https://doi.org/10.1016/j.pepi.2011.07.001

Nakazawa, H., & Morimoto, N. (1971). Phase relations and superstructures of pyrrhotite, Fe1xS. *Materials Research Bulletin*, *6*(5), 345–357. https://doi.org/10.1016/0025-5408(71)90168-1

Ni, S., Tan, E., Gurnis, M., & Helmberger, D. (2002). Sharp sides to the African superplume. *Science*, *296*(5574), 1850–1852. https://doi.org/10.1126/science.1070698

Nomura, R., Hirose, K., Uesugi, K., Ohishi, Y., Tsuchiyama, A., Miyake, A., & Ueno, Y. (2014). Low Core-Mantle Boundary Temperature Inferred from the Solidus of Pyrolite. *Science*, *343*(6170), 522–525. https://doi.org/10.1126/science.1248186

Ohta, K., Fujino, K., Kuwayama, Y., Kondo, T., Shimizu, K., & Ohishi, Y. (2014). Highly conductive iron-rich (Mg,Fe)O magnesiowüstite and its stability in the Earth's lower mantle. *Journal of Geophysical Research: Solid Earth*, *119*(6), 4656–4665. https://doi.org/10.1002/2014JB010972

Ohta, K., Cohen, R. E., Hirose, K., Haule, K., Shimizu, K., & Ohishi, Y. (2012). Experimental and Theoretical Evidence for Pressure-Induced Metallization in FeO with Rocksalt-Type Structure. *Physical Review Letters*, *108*(2), 026403. https://doi.org/10.1103/PhysRevLett.108.026403

Ohtani, E., & Ringwood, A. (1984). Composition of the core, I. Solubility of oxygen in molten iron at high temperatures. *Earth and Planetary Science Letters*, *71*(1), 85–93. https://doi.org/10.1016/0012-821X(84)90054-2

Ohtani, E. (2020). The role of water in Earth's mantle. *National Science Review*, *7*(1), 224–232. https://doi.org/10.1093/nsr/nwz071

Ohtani, E., & Maeda, M. (2001). Density of basaltic melt at high pressure and stability of the melt at the base of the lower mantle. *Earth and Planetary Science Letters*. https://doi.org/10.1016/S0012-821X(01)00505-2

Okazaki, A. (1959). The Variation of Superstructure in Iron Selenide Fe 7 Se 8. *Journal of the Physical Society of Japan*, *14*(1), 112–113. https://doi.org/10.1143/JPSJ.14.112

Olson, P. (2013). The new core paradox. *Science*, *342*(6157), 431–432. https://doi.org/10.1126/science.1243477

Ono, S., Ohishi, Y., & Kikegawa, T. (2007). High-pressure study of rhombohedral iron oxide, FeO, at pressures between 41 and 142 GPa. *Journal of Physics: Condensed Matter*, *19*(3), 036205. https://doi.org/10.1088/0953-8984/19/3/036205

Ozawa, H., Hirose, K., Mitome, M., Bando, Y., Sata, N., & Ohishi, Y. (2009). Experimental study of reaction between perovskite and molten iron to 146 GPa and implications for chemically distinct buoyant layer at the top of the core. *Physics and Chemistry of Minerals*, *36*(6), 355–363. https://doi.org/10.1007/s00269-008-0283-x

Ozawa, H., Takahashi, F., Hirose, K., Ohishi, Y., & Hirao, N. (2011). Phase Transition of FeO and Stratification in Earth's Outer Core. *Science*, *334*(6057), 792–794. https://doi.org/10.1126/science.1208265

Parisiades, P., Cova, F., & Garbarino, G. (2019). Melting curve of elemental zirconium. *Physical Review B*, *100*(5), 054102. https://doi.org/10.1103/PhysRevB.100.054102

Pradhan, G. K., Fiquet, G., Siebert, J., Auzende, A.-L., Morard, G., Antonangeli, D., & Garbarino, G. (2015). Melting of MORB at core–mantle boundary. *Earth and Planetary Science Letters*, *431*, 247–255. https://doi.org/10.1016/j.epsl.2015.09.034

Prakapenka, V. B., Kubo, A., Kuznetsov, A., Laskin, A., Shkurikhin, O., Dera, P., Rivers, M. L., & Sutton, S. R. (2008). Advanced flat top laser heating system for high pressure research at GSECARS: application to the melting

behavior of germanium. *High Pressure Research*, *28*(3), 225–235. https://doi.org/10.1080/08957950802050718

Prakapenka, V., Shen, G., & Dubrovinsky, L. (2003). Carbon transport in diamond anvil cells. *High Temperatures-High Pressures*, *35/36*(2), 237–249. https://doi.org/10.1068/htjr098

Prescher, C., & Prakapenka, V. B. (2015). DIOPTAS: A program for reduction of two-dimensional X-ray diffraction data and data exploration. *High Pressure Research*, *35*(3), 223–230. https://doi.org/10.1080/08957959.2015.1059835

Reali, R., Jackson, J. M., Van Orman, J., Bower, D. J., Carrez, P., & Cordier, P. (2019). Modeling viscosity of (Mg,Fe)O at lowermost mantle conditions. *Physics of the Earth and Planetary Interiors*, *287*(June 2018), 65–75. https://doi.org/10.1016/j.pepi.2018.12.005

Reiss, M. C., Long, M. D., & Creasy, N. (2019). Lowermost Mantle Anisotropy Beneath Africa From Differential SKS - SKKS Shear-Wave Splitting. *Journal of Geophysical Research: Solid Earth*, *124*(8), 8540–8564. https://doi.org/10.1029/2018JB017160
-anisotropy is generally observed at the margins of the African LLSVP, with the interior appearing mostly isotropic -however, all studies are limited in spatial coverage of the African LLSVP as a whole

Ricolleau, A., Fei, Y., Corgne, A., Siebert, J., & Badro, J. (2011). Oxygen and silicon contents of Earth's core from high pressure metal-silicate partitioning experiments. *Earth and Planetary Science Letters*, *310*(3-4), 409–421. https://doi.org/10.1016/j.epsl.2011.08.004

Rost, S., Garnero, E. J., & Williams, Q. (2006). Fine-scale ultralow-velocity zone structure from high-frequency seismic array data. *Journal of Geophysical Research*, *111*(B9), B09310. https://doi.org/10.1029/2005JB004088

Rost, S., Garnero, E. J., Williams, Q., & Manga, M. (2005). Seismological constraints on a possible plume root at the core–mantle boundary. *Nature*, *435*(7042), 666–669. https://doi.org/10.1038/nature03620

Roth, W. L. (1960). Defects in the crystal and magnetic structures of ferrous oxide. *Acta Crystallographica*, *13*(2), 140–149. https://doi.org/10.1107/S0365110X60000297

Sakai, T., Ohtani, E., Hirao, N., & Ohishi, Y. (2011). Stability field of the hcp-structure for Fe, Fe-Ni, and Fe-Ni-Si alloys up to 3 Mbar. *Geophysical Research Letters*, *38*(9), 2–6. https://doi.org/10.1029/2011GL047178

Santosh, M., Maruyama, S., & Yamamoto, S. (2009). The making and breaking of supercontinents: Some speculations based on superplumes, super downwelling and the role of tectosphere. *Gondwana Research*, *15*(3-4), 324–341. https://doi.org/10.1016/j.gr.2008.11.004

Schmidt, A., Skeffington, R. A., Thordarson, T., Self, S., Forster, P. M., Rap, A., Ridgwell, A., Fowler, D., Wilson, M., Mann, G. W., Wignall, P. B., & Carslaw, K. S. (2016). Selective environmental stress from sulphur emitted by continental flood basalt eruptions. *Nature Geoscience*, *9*(1), 77–82. https://doi.org/10.1038/ngeo2588

Seagle, C., Heinz, D., Campbell, A., Prakapenka, V., & Wanless, S. (2008). Melting and thermal expansion in the Fe–FeO system at high pressure. *Earth and Planetary Science Letters*, *265*(3-4), 655–665. https://doi.org/10.1016/j.epsl.2007.11.004

Shahar, A., Ziegler, K., Young, E. D., Ricolleau, A., Schauble, E. A., & Fei, Y. (2009). Experimentally determined Si isotope fractionation between silicate and Fe metal and implications for Earth's core formation. *Earth and Planetary Science Letters*, *288*(1-2), 228–234. https://doi.org/10.1016/j.epsl.2009.09.025

Shen, G., Lazor, P., & Saxena, S. (1993). Melting of wstite and iron up to pressures of 600 kbar. *Physics and Chemistry of Minerals*, *20*(2), 91–96. https://doi.org/10.1007/BF00207201

Shen, G., Wang, Y., Dewaele, A., Wu, C., Fratanduono, D. E., Eggert, J., Klotz, S., Dziubek, K. F., Loubeyre, P., Fat'yanov, O. V., Asimow, P. D., Mashimo, T., & Wentzcovitch, R. M. M. (2020). Toward an international practical pressure scale: A proposal for an IPPS ruby gauge (IPPS-Ruby2020). *High Pressure Research*, *40*(3), 299–314. https://doi.org/10.1080/08957959.2020.1791107

Shirey, S. B., & Richardson, S. H. (2011). Start of the Wilson Cycle at 3 Ga Shown by Diamonds from Subcontinental Mantle. *Science*, *333*(6041), 434–436. https://doi.org/10.1126/science.1206275

Shukla, G., Wu, Z., Hsu, H., Floris, A., Cococcioni, M., & Wentzcovitch, R. M. (2015). Thermoelasticity of Fe 2+ -bearing bridgmanite. *Geophysical Research Letters*, *42*(6), 1741–1749. https://doi.org/10.1002/2014GL062888

Simmons, N. A., & Grand, S. P. (2002). Partial melting in the deepest mantle. *Geophysical Research Letters*, *29*(11), 1552. https://doi.org/10.1029/2001GL013716

Simmons, N. A., Forte, A. M., Boschi, L., & Grand, S. P. (2010). GyPSuM: A joint tomographic model of mantle density and seismic wave speeds. *Journal of Geophysical Research*, *115*(B12), B12310. https://doi.org/10.1029/2010JB007631

Simon, F., & Glatzel, G. (1929). Bemerkungen zur Schmelzdruckkurve. *Zeitschrift für anorganische und allgemeine Chemie*, *178*(1), 309–316. https://doi.org/10.1002/zaac.19291780123

Sinmyo, R., Hirose, K., Nishio-Hamane, D., Seto, Y., Fujino, K., Sata, N., & Ohishi, Y. (2008). Partitioning of iron between perovskite/postperovskite and ferropericlase in the lower mantle. *Journal of Geophysical Research: Solid Earth*, *113*(11). https://doi.org/10.1029/2008JB005730

Sinmyo, R., Hirose, K., & Ohishi, Y. (2019). Melting curve of iron to 290 GPa determined in a resistance-heated diamond-anvil cell. *Earth and Planetary Science Letters*, *510*, 45–52. https://doi.org/10.1016/j.epsl.2019.01.006

Sohl, F., & Schubert, G. (2007). Interior Structure, Composition, and Mineralogy of the Terrestrial Planets. *Treatise on geophysics* (pp. 27–68). Elsevier. https://doi.org/10.1016/B978-044452748-6.00153-X

Solomatova, N. V., Jackson, J. M., Sturhahn, W., Wicks, J. K., Zhao, J., Toellner, T. S., Kalkan, B., & Steinhardt, W. M. (2016). Equation of state and spin crossover of (Mg,Fe)O at high pressure, with implications for explaining topographic relief at the core-mantle boundary. *American Mineralogist*, *101*(5), 1084–1093. https://doi.org/10.2138/am-2016-5510

Steenstra, E., & van Westrenen, W. (2020). Geochemical constraints on core-mantle differentiation in Mercury and the aubrite parent body. *Icarus*, *340*(January), 113621. https://doi.org/10.1016/j.icarus.2020.113621

Steinberger, B., Sutherland, R., & O'Connell, R. J. (2004). Prediction of Emperor-Hawaii seamount locations from a revised model of global plate motion and mantle flow. *Nature*, *430*(6996), 167–173. https://doi.org/10.1038/nature02660

Sturhahn, W. (2000). CONUSS and PHOENIX: Evaluation of nuclear resonant scattering data. *Hyperfine Interactions*, *125*(1-4), 149–172. https://doi.org/10.1023/A:1012681503686

Sturhahn, W. (2021). MINUTI open source software, version 2.2.0.

Sturhahn, W. (2004). Nuclear resonant spectroscopy. *Journal of Physics: Condensed Matter*, *16*(5), S497–S530. https://doi.org/10.1088/0953-8984/16/5/009

Sturhahn, W., & Jackson, J. M. (2007). Geophysical applications of nuclear resonant spectroscopy. *Advances in high-pressure mineralogy* (pp. 157–174). Geological Society of America. https://doi.org/10.1130/2007.2421(09)

Sturhahn, W., Jackson, J. M., & Lin, J. F. (2005). The spin state of iron in minerals of Earth's lower mantle. *Geophysical Research Letters*, *32*(12), 1–5. https://doi.org/10.1029/2005GL022802

Stutzmann, V., Dewaele, A., Bouchet, J., Bottin, F., & Mezouar, M. (2015). High-pressure melting curve of titanium. *Physical Review B - Condensed Matter and Materials Physics*, *92*(22), 1–10. https://doi.org/10.1103/PhysRevB.92.224110

Sun, D., Helmberger, D., Lai, V. H., Gurnis, M., Jackson, J. M., & Yang, H. Y. (2019). Slab Control on the Northeastern Edge of the Mid-Pacific LLSVP Near Hawaii. *Geophysical Research Letters*, *46*(6), 3142–3152. https://doi.org/10.1029/2018GL081130

Sun, D., Helmberger, D., Ni, S., & Bower, D. (2009). Direct measures of lateral velocity variation in the deep Earth. *Journal of Geophysical Research: Solid Earth*, *114*(5), 1–18. https://doi.org/10.1029/2008JB005873

Sun, D., Helmberger, D. V., Jackson, J. M., Clayton, R. W., & Bower, D. J. (2013). Rolling hills on the core-mantle boundary. *Earth and Planetary Science Letters*, *361*, 333–342. https://doi.org/10.1016/j.epsl.2012.10.027

Tange, Y., Takahashi, E., Nishihara, Y., Funakoshi, K.-i., & Sata, N. (2009). Phase relations in the system MgO-FeO-SiO 2 to 50 GPa and 2000°C: An application of experimental techniques using multianvil apparatus with sintered diamond anvils. *Journal of Geophysical Research*, *114*(B2), B02214. https://doi.org/10.1029/2008JB005891

Tarduno, J., Bunge, H.-P., Sleep, N., & Hansen, U. (2009). The Bent Hawaiian-Emperor Hotspot Track: Inheriting the Mantle Wind. *Science*, *324*(5923), 50–53. https://doi.org/10.1126/science.1161256

Tateno, S., Komabayashi, T., Hirose, K., Hirao, N., & Ohishi, Y. (2019). Static compression of B2 KCl to 230 GPa and its P-V-T equation of state. *American Mineralogist*, *104*(5), 718–723. https://doi.org/10.2138/am-2019-6779

Tatsumi, Y., & Stern, R. (2006). Manufacturing Continental Crust in the Subduction Factory. *Oceanography*, *19*(4), 104–112. https://doi.org/10.5670/oceanog.2006.09

Tatsumi, Y., Suzuki, T., Ozawa, H., Hirose, K., Hanyu, T., & Ohishi, Y. (2014). Accumulation of 'anti-continent' at the base of the mantle and its recycling in mantle plumes. *Geochimica et Cosmochimica Acta*, *143*, 23–33. https://doi.org/10.1016/j.gca.2013.11.019

Thorne, M. S., & Garnero, E. J. (2004). Inferences on ultralow-velocity zone structure from a global analysis of SPdKS waves. *Journal of Geophysical Research: Solid Earth*, *109*(8), 1–22. https://doi.org/10.1029/2004JB003010

Thorne, M. S., Takeuchi, N., & Shiomi, K. (2019). Melting at the Edge of a Slab in the Deepest Mantle. *Geophysical Research Letters*, *46*(14), 8000–8008. https://doi.org/10.1029/2019GL082493

To, A., Fukao, Y., & Tsuboi, S. (2011). Evidence for a thick and localized ultra low shear velocity zone at the base of the mantle beneath the central Pacific. *Physics of the Earth and Planetary Interiors*, *184*(3-4), 119–133. https://doi.org/10.1016/j.pepi.2010.10.015

Toby, B. H., & Von Dreele, R. B. (2013). GSAS-II: The genesis of a modern open-source all purpose crystallography software package. *Journal of Applied Crystallography*, *46*(2), 544–549. https://doi.org/10.1107/S0021889813003531

Toellner, T. S. (2000). Monochromatization of synchrotron radiation for nuclear resonant scattering experiments. *Hyperfine Interactions*, *125*(1-4), 3–28. https://doi.org/10.1023/A:1012621317798

Torchio, R., Boccato, S., Miozzi, F., Rosa, A. D., Ishimatsu, N., Kantor, I., Sévelin-Radiguet, N., Briggs, R., Meneghini, C., Irifune, T., & Morard, G. (2020). Melting Curve and Phase Relations of Fe-Ni Alloys: Implications for the Earth's Core Composition. *Geophysical Research Letters*, *47*(14), 1–7. https://doi.org/10.1029/2020GL088169

Tsuchiya, T., Wentzcovitch, R. M., da Silva, C. R. S., & de Gironcoli, S. (2006). Spin Transition in Magnesiowüstite in Earth's Lower Mantle. *Physical Review Letters*, *96*(19), 198501. https://doi.org/10.1103/PhysRevLett.96.198501

von Goldbeck, O. K. (1982). Iron—Nickel Fe—Ni. *Iron—binary phase diagrams* (pp. 73–78). Springer Berlin Heidelberg. https://doi.org/10.1007/978-3-662-08024-5_44

Wang, C. H., Chen, T. K., Chang, C. C., Lee, Y. C., Wang, M. J., Huang, K. C., Wu, P. M., & Wu, M. K. (2018). Fe-vacancy and superconductivity in FeSe-based superconductors. *Physica C: Superconductivity and its Applications*, *549*(February), 61–65. https://doi.org/10.1016/j.physc.2018.02.047

Wang, H., & Salveson, I. (2005). A review on the mineral chemistry of the non-stoichiometric iron sulphide, Fe1-xS (0 x 0.125): Polymorphs, phase relations and transitions, electronic and magnetic structures. *Phase Transitions*, *78*(7-8), 547–567. https://doi.org/10.1080/01411590500185542

Watt, J. P., Davies, G. F., & O'Connell, R. J. (1976). The elastic properties of composite materials. *Reviews of Geophysics*, *14*(4), 541. https://doi.org/10.1029/RG014i004p00541

Welberry, T. R., Goossens, D. J., & Heerdegen, A. P. (2014). Local order in wüstite using a pair distribution function (PDF) approach. *Mineralogical Magazine*, *78*(2), 373–385. https://doi.org/10.1180/minmag.2014.078.2.10

Wentzcovitch, R. M., Wu, Z., & Carrier, P. (2010). First Principles Quasiharmonic Thermoelasticity of Mantle Minerals. *Reviews in Mineralogy and Geochemistry*, *71*(1), 99–128. https://doi.org/10.2138/rmg.2010.71.5

Wicks, J. K., Jackson, J. M., & Sturhahn, W. (2010). Very low sound velocities in iron-rich (Mg,Fe)O: Implications for the core-mantle boundary region. *Geophysical Research Letters*, *37*(15), 1–5. https://doi.org/10.1029/2010GL043689

Wicks, J. K. (2013). Sound Velocities and Equation of State of iron-rich (Mg,Fe)O Thesis by. *California Institute of Technology*, *2013*.

Wicks, J. K., Jackson, J. M., Sturhahn, W., & Zhang, D. (2017). Sound velocity and density of magnesiowüstites: Implications for ultralow-velocity zone topography. *Geophysical Research Letters*, *44*(5), 2148–2158. https://doi.org/10.1002/2016GL071225

Wicks, J. K., Jackson, J. M., Sturhahn, W., Zhuravlev, K. K., Tkachev, S. N., & Prakapenka, V. B. (2015). Thermal equation of state and stability of (Mg0.06Fe0.94)O. *Physics of the Earth and Planetary Interiors*, *249*, 28–42. https://doi.org/10.1016/j.pepi.2015.09.003

Wicks, J. K., Smith, R. F., Fratanduono, D. E., Coppari, F., Kraus, R. G., Newman, M. G., Rygg, J. R., Eggert, J. H., & Duffy, T. S. (2018). Crystal structure and equation of state of Fe-Si alloys at super-Earth core conditions. *Science Advances*, *4*(4), eaao5864. https://doi.org/10.1126/sciadv.aao5864

Williams, Q., & Garnero, E. J. (1996). Seismic evidence for partial melt at the base of earth's mantle. *Science*, *273*(5281), 1528–1530. https://doi.org/10.1126/science.273.5281.1528

Wolf, A. S., Jackson, J. M., Dera, P., Prakapenka, V. B., & Al, W. E. T. (2015). Journal of Geophysical Research : Solid Earth The thermal equation of state of (Mg , Fe) SiO 3 bridgmanite (perovskite) and implications for lower mantle structures. *J. geophys. Res.*, *120*, 7460–7489. https://doi.org/10.1002/2015JB012108.Received

Wu, Z., & Wentzcovitch, R. M. (2014). Spin crossover in ferropericlase and velocity heterogeneities in the lower mantle. *Proceedings of the National Academy of Sciences*, *111*(29), 10468–10472. https://doi.org/10.1073/pnas.1322427111

Yu, S., & Garnero, E. J. (2018). Ultralow Velocity Zone Locations: A Global Assessment. *Geochemistry, Geophysics, Geosystems*, *19*(2), 396–414. https://doi.org/10.1002/2017GC007281

Yuan, K., & Romanowicz, B. (2017). Seismic evidence for partial melting at the root of major hot spot plumes. *Science*, *357*(6349), 1–5. https://doi.org/10.1126/science.aan0760

Zhan, Z. (2020). Mechanisms and Implications of Deep Earthquakes. *Annual Review of Earth and Planetary Sciences*, *48*, 147–174. https://doi.org/10.1146/annurev-earth-053018-060314

Zhang, B., Ni, S., Sun, D., Shen, Z., Jackson, J. M., & Wu, W. (2018). Constraints on small-scale heterogeneity in the lowermost mantle from observations of near podal PcP precursors. *Earth and Planetary Science Letters*, *489*, 267–276. https://doi.org/10.1016/j.epsl.2018.01.033

Zhang, D., Jackson, J. M., Sturhahn, W., Zhao, J., Alp, E. E., & Hu, M. Y. (2022). Measurements of the Lamb-Mössbauer factor at simultaneous high-pressure-temperature conditions and estimates of the equilibrium isotopic fractionation of iron. *American Mineralogist*, *107*(3), 421–431. https://doi.org/10.2138/am-2021-7884

Zhang, D., Jackson, J. M., Zhao, J., Sturhahn, W., Alp, E. E., Hu, M. Y., Toellner, T. S., Murphy, C. A., & Prakapenka, V. B. (2016). Temperature of Earth's core constrained from melting of Fe and Fe0.9Ni0.1 at high pressures. *Earth and Planetary Science Letters*, *447*, 72–83. https://doi.org/10.1016/j.epsl.2016.04.026

Zhang, D., Jackson, J. M., Zhao, J., Sturhahn, W., Alp, E. E., Toellner, T. S., & Hu, M. Y. (2015). Fast temperature spectrometer for samples under extreme conditions. *Review of Scientific Instruments*, *86*(1), 013105. https://doi.org/10.1063/1.4905431

Zhang, L., & Fei, Y. (2008). Melting behavior of (Mg,Fe)O solid solutions at high pressure. *Geophysical Research Letters*, *35*(13), L13302. https://doi.org/10.1029/2008GL034585

Zhang, Y., Sekine, T., Lin, J. F., He, H., Liu, F., Zhang, M., Sato, T., Zhu, W., & Yu, Y. (2018). Shock Compression and Melting of an Fe-Ni-Si Alloy: Implications for the Temperature Profile of the Earth's Core and the Heat Flux Across the Core-Mantle Boundary. *Journal of Geophysical Research: Solid Earth*, *123*(2), 1314–1327. https://doi.org/10.1002/2017JB014723

Zhao, C., Garnero, E. J., Li, M., McNamara, A., & Yu, S. (2017). Intermittent and lateral varying ULVZ structure at the northeastern margin of the Pacific LLSVP. *Journal of Geophysical Research: Solid Earth*, *122*(2), 1198–1220. https://doi.org/10.1002/2016JB013449

Zhao, D. (2004). Global tomographic images of mantle plumes and subducting slabs: Insight into deep Earth dynamics. *Physics of the Earth and Planetary Interiors*, *146*(1-2), 3–34. https://doi.org/10.1016/j.pepi.2003.07.032

Appendix A

SUPPLEMENTARY MATERIAL FOR CHAPTER 2

We develop an inverse mixing model with the purpose to determine the mixture of individual minerals with aggregate properties that bets match a set of target properties (e.g., velocity reductions and density increase relative to PREM for a given ULVZ observation). The mixture contains $(N + 1)$ individual minerals, e.g., (Mg,Fe)O magnesiowüstite (Mw), (Mg,Fe)SiO_3 bridgmanite (Br), $CaSiO_3$ calcium silicate perovskite (CaPv). The concentrations $p_j \geq 0$ of the mienrals in the mixture are normalized by

$$\sum_{j=1}^{N+1} p_j = 1$$

The minerals have properties ϕ_{jk}, where j and k are the number of mineral types and properties, respectively. In addition to the density, properties of interest for our inversions are the bulk modulus and shear modulus or their inverse, dependent on Voigt or Reuss mixing, respectively. We calculate these moduli from the compressional and shear velocities. Average properties of the aggregate are then

$$\langle \phi_k \rangle = \sum_{j=1}^{N+1} p_j \phi_{jk} = \phi_{N+1,k} + \sum_{j=1}^{N} p_j (\phi_{j,k} - \phi_{N+1,k})$$

where the concentration p_{N+1} is eliminated by use of $\sum_{j=1}^{N+1} p_j = 1$. The measure for matching these average properties and the target properties Φ_k is defined as

$$M(\{p_j\}) = \sum_{k=1}^{n} w_k (\langle \phi_k \rangle - \Phi_k)^2 + \sum_{j=1}^{N} \frac{(p_j - P_j)^2}{\delta^2 P_j}$$

where n is the number of properties. In order to produce a physically meaningful solution to the inversion, we can introduce priors P_j on the mineral concentrations with uncertainties $\delta^2 P_j$. The best matching is achieved for the smallest measure. The weights w_k are taken as

$$w_k = \left(\delta\Phi_k^2 + \sum_{j=1}^{N+1} p_j^2 \delta\phi_{jk}^2 \right)^{-1}$$

where $\delta\Phi_k^2$ and $\delta\phi_{jk}^2$ are the variances of the target properties Φ_k and mineral properties ϕ_{jk}, respectively. Because n (number of properties: elastic moduli and

density) exceeds the dimensionality of the parameter space N (total minerals minus one), the measure never takes its smallest possible value, zero, but can only be minimized by finding a local minimum of it. The optimal concentrations satisfy N non-linear equations given by

$$\frac{\partial}{\partial p_j} M\left(\{p_j\}\right) = 0$$

The non-linearity is caused by the concentration dependence of the weights w_k. If the solution does not satisfy $p_j \geq 0$ for all concentrations, the local minimum of the measure is located outside of the truncated N dimensional parameter space.

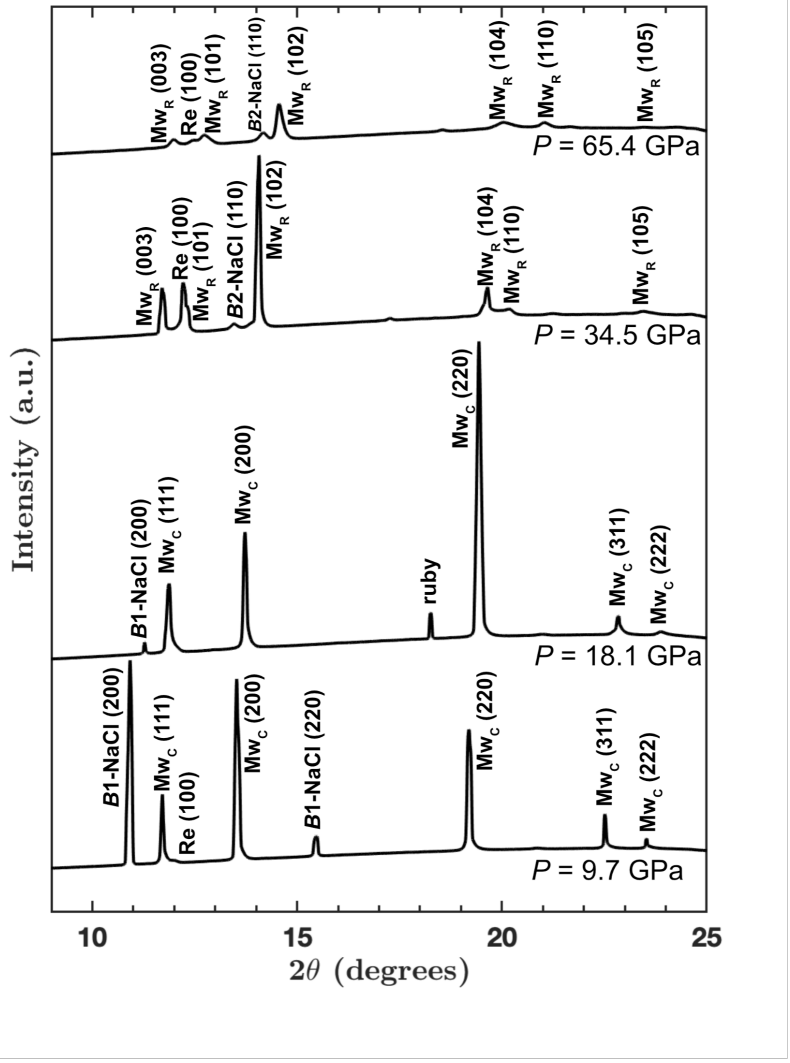

Figure A.1: Examples of integrated XRD patterns for Mw94. MwC and MwR labels identify diffraction peaks for the B1 and rhombohedral crystal structures of Mw94, respectively. The splitting of MwC peaks indicates the onset of the rhombohedral distortion. The B1-NaCl (200) peak may be overlapping with the peak labeled MwR (003) at 34.5 GPa, indicating that NaCl is undergoing transition from the B1 to B2 phase at this pressure. Evidence for B1-NaCl peaks is not observed at pressures above 34.5 GPa.

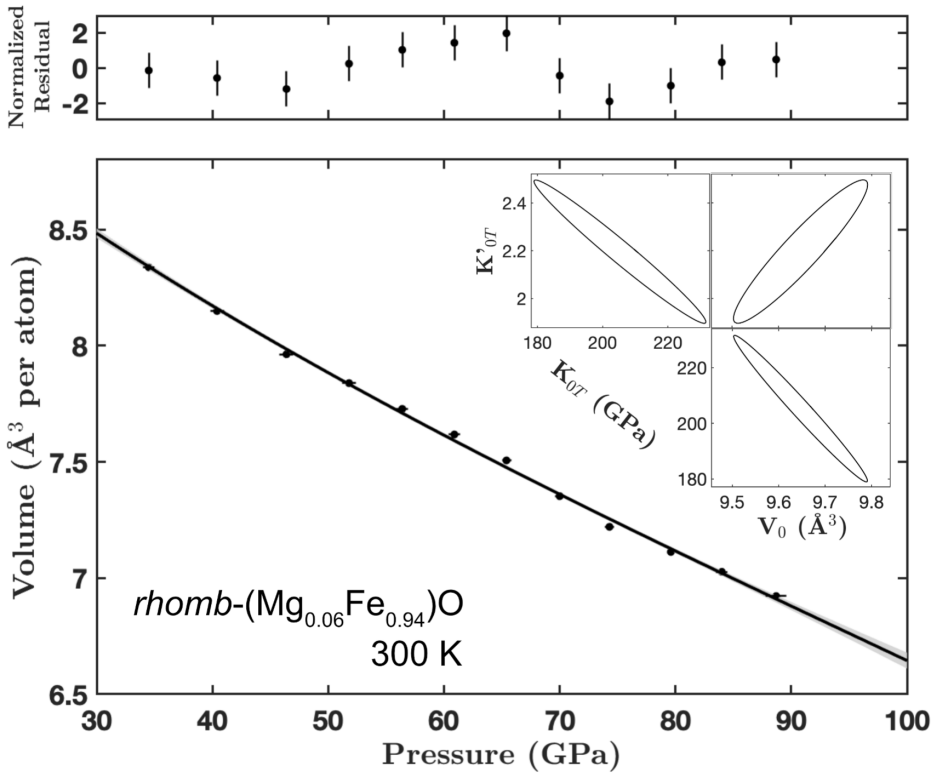

Figure A.2: Unit-cell volumes of rhombohedral Mw94 (solid black circles) and third-order Birch Murnaghan equation of state (solid black line) fit using MINUTI (Sturhahn, 2021). Normalized residuals of the fit are shown in the top panel. Error ellipses demonstrate the correlations between fit parameters.

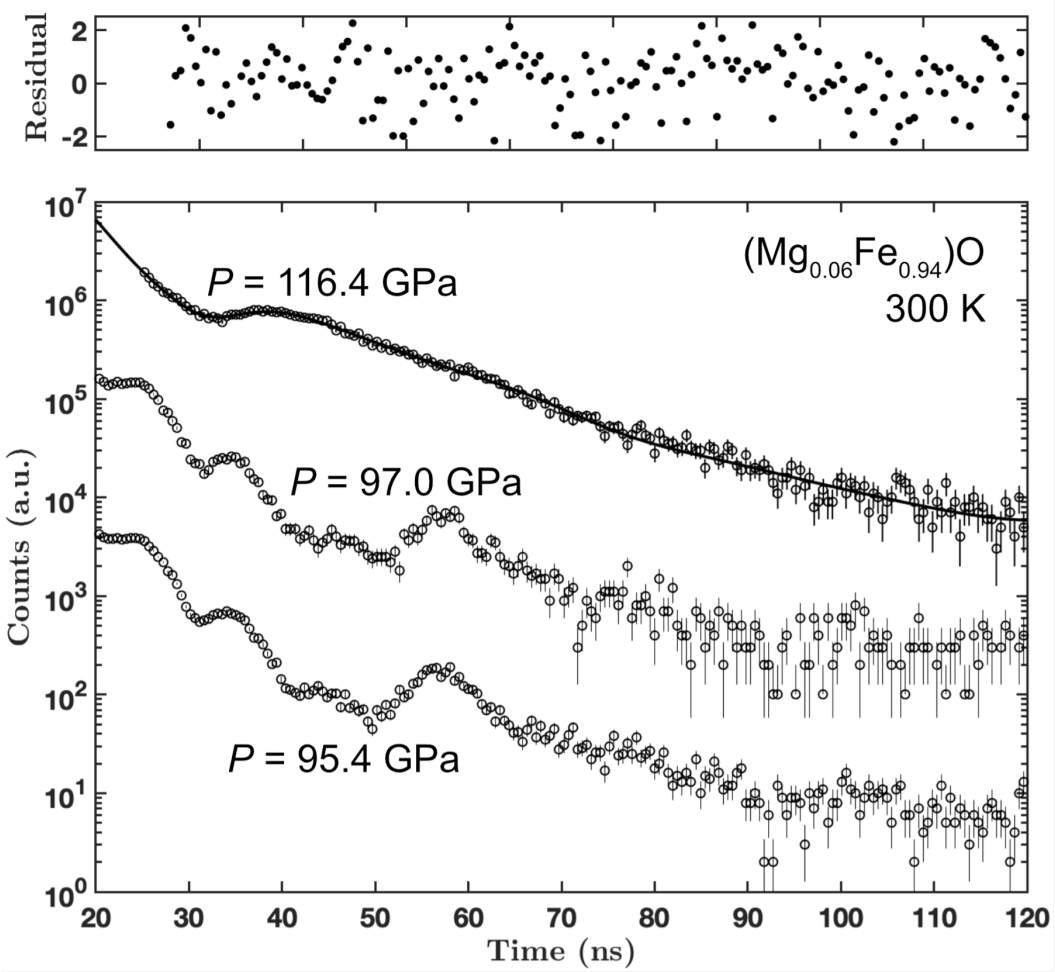

Figure A.3: SMS spectra of Mw94 at three compression points with the highest-pressure spectrum fit using CONUSS version 2.2.0 (Sturhahn, 2000). The significant loss of fast oscillations in the highest-pressure spectrum suggests the loss of magnetic ordering that may be associated with the high-spin to low-spin transition in the Fe2+ sites. The best-fit model at 116.4 GPa shows that 36% of the iron atoms have transitioned into the low-spin state, with 3% of the iron atoms retaining the magnetic ordering in a high-spin state and the remaining fraction indicative of a broad high-spin Fe2+-like site with no magnetic ordering (Table A.2).

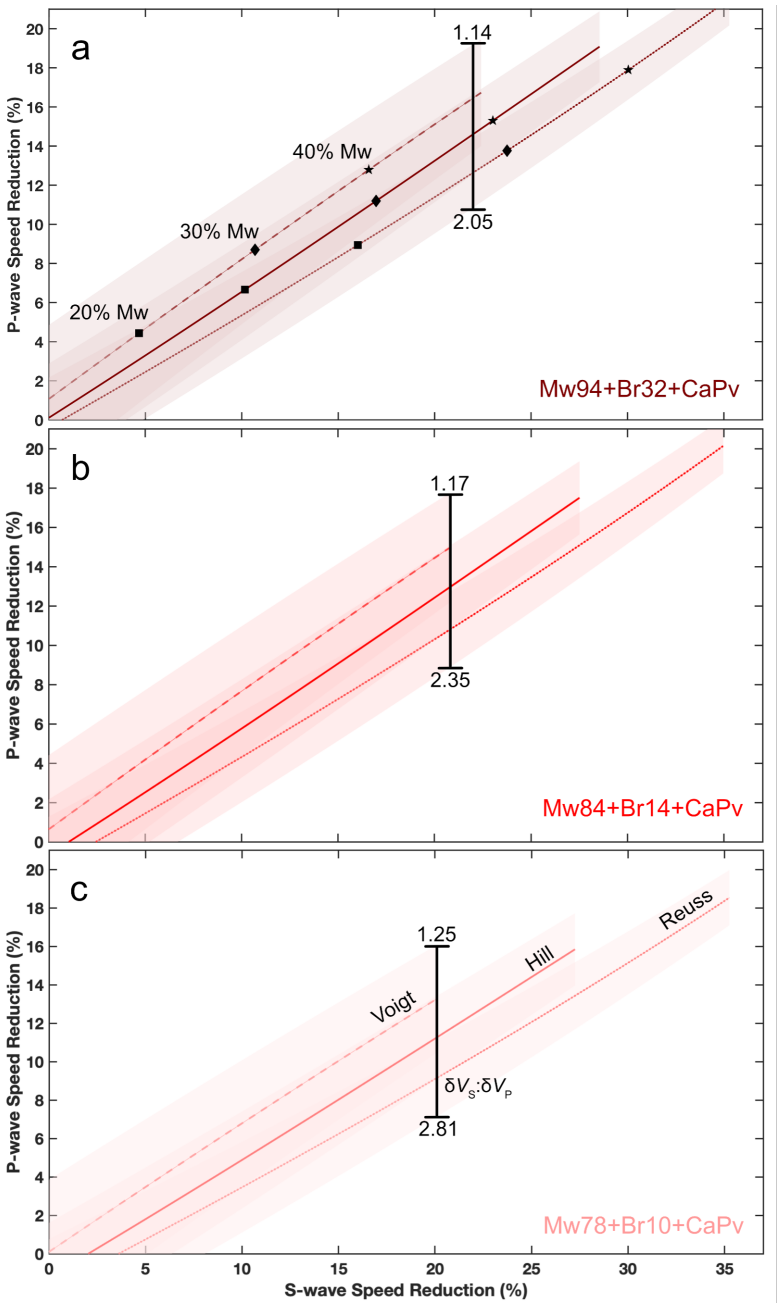

Figure A.4: Seismic signatures of phase assemblages containing iron-rich (Mg,Fe)O (or magnesiowüstite "Mw") in the lowermost mantle, relative to PREM. Forward models of three different iron-concentrations of Mw mixed with bridgmanite and calcium perovskite at a fixed Br:CaPv ratio of 10:1. Vertical bars indicate the range of δVP:δVS at a given δVS value. Mw# and Br# indicate the mol% of Fe. (a) Concentration of Mw94 ranges from 13.6% (Voigt), 5.7% (Reuss), and 8.3% (Hill) up to 50%. (b) Concentration of Mw84 ranges from 16.7% (Voigt), 6.8% (Reuss), and 10.2% (Hill) up to 50%. (c) Concentration of Mw78 ranges from 17.8% (Voigt), 6.9% (Reuss), and 10.6% (Hill) up to 50%.

Table A.1: Pressure-volume measurements for Mw94 fit from XRD patterns using the GSAS-II software (Toby & Von Dreele, 2013). Pressures were determined from ruby fluorescence (Dewaele et al., 2008) with uncertainties estimated as the difference of the pressures measured for two rubies before and after each XRD measurement (given in parentheses). Measurements up through 30.1 GPa exhibit the B1 phase, while measurements at higher pressures show that Mw94 is fully in the rhombohedral phase. We exclude measurements at 26.7 GPa and 30.1 GPa from the final B1 EOS fit due to change in the P-V trend preceding the cubic-rhombohedral transition

Measurement	Pressure (GPa)	Volume ($Å^3$ /atom)	Measurement	Pressure (GPa)	Volume ($Å^3$ /atom)
P1	1.5 (2)	9.751 (13)	P14	26.7 (3)	8.575 (11)
P2	3.3 (1)	9.653 (15)	P15	30.1 (3)	8.451 (20)
P3	5.2 (1)	9.562 (6)	P16	34.5 (5)	8.337 (7)
P4	6.4 (2)	9.474 (15)	P17	40.4 (6)	8.149 (5)
P5	8.1 (1)	9.424 (18)	P18	46.4 (6)	7.963 (7)
P6	9.7 (3)	9.303 (15)	P19	51.8 (6)	7.839 (10)
P7	11.3 (2)	9.262 (6)	P20	56.4 (5)	7.728 (12)
P8a	12.7 (1)	9.183 (6)	P21	60.9 (5)	7.618 (13)
P8b	13.4 (1)	9.143 (6)	P22	65.4 (4)	7.506 (12)
P9	15.4 (1)	9.054 (8)	P23	70.0 (4)	7.352 (15)
P10	16.8 (1)	9.001 (5)	P24	74.3 (4)	7.220 (15)
P11	18.1 (1)	8.953 (8)	P25	79.6 (1)	7.112 (13)
P12	20.1 (2)	8.863 (14)	P26	84.0 (5)	7.027 (13)
P13	23.3 (2)	8.757 (20)	P27	88.7 (9)	6.922 (15)

Table A.2: Hyperfine parameters for Mw94 at P = 116.4 ± 0.5 GPa fit using CONUSS version 2.2.0 (Sturhahn, 2000). Uncertainties are given at the 68% level. Three distinct Fe^{2+} sites are required to fit the spectrum. At this pressure, 36% of iron atoms have transitioned into the low-spin state, with 3% of iron atoms retaining the magnetic ordering in a high-spin state, and 60% remain in a high-spin state with no magnetic ordering. The FWHM values give the full width at half maximum of a Gaussian distribution of either isomer shift (sites 1 and 3) or magnetic hyperfine field (site 2).

$P = 116.4 \pm 0.5$ GPa	Site 1 Fe^{2+}_{HS}	Site 2 Fe^{2+}_{HS}	Site 3 Fe^{2+}_{LS}
Weight	0.600 ± 0.019	0.035 ± 0.015	0.364 ± 0.019
Relative Isomer Shift (mm/s)	0.430 ± 0.011	0.430 ± 0.011	0
FWHM	1.83 ± 0.02 mm/s	10.6 ± 1.4 T	0.092 ± 0.015 mm/s
Magnetic Hyperfine Field (T)	0	34.2 ± 0.3	0
Thickness (micron)		3.17 ± 0.04	
Reduced χ^2		1.1 ± 0.1	

Table A.3: Compressional (V_P) and shear (V_S) wave velocities and densities for the phase assemblages considered here, calculated at CMB conditions (135.8 GPa and 3800 K). For bridgmanite (Br), we follow the finite strain formalism in B. Li and Zhang (2005), with updated values for K_{0T} and K'_{0T} from Dorfman et al. (2013), updated temperature derivatives from Wentzcovitch et al. (2010), and thermal parameters from Wolf et al. (2015). For calcium perovskite, we use results from Gréaux et al. (2019) and extrapolate using the finite strain analysis of Duffy and Anderson (1989). Mw# and Br# indicate the mol% of Fe.

	Mw94	Mw84	Mw78	Br32	Br14	Br10	CaPv
V_P (km/s)	8.93 ± 0.14	9.07 ± 0.14	9.40 ± 0.14	14.55 ± 0.36	14.88 ± 0.37	14.96 ± 0.37	13.14 ± 0.33
V_S (km/s)	3.46 ± 0.09	3.45 ± 0.09	3.44 ± 0.09	8.01 ± 0.20	8.20 ± 0.21	8.24 ± 0.21	6.78 ± 0.34
ρ (g/cm^3)	8.528 ± 0.015	8.221 ± 0.015	7.888 ± 0.015	5.733 ± 0.057	5.479 ± 0.055	5.423 ± 0.054	5.494 ± 0.055

Appendix B

SUPPLEMENTARY MATERIAL FOR CHAPTER 3

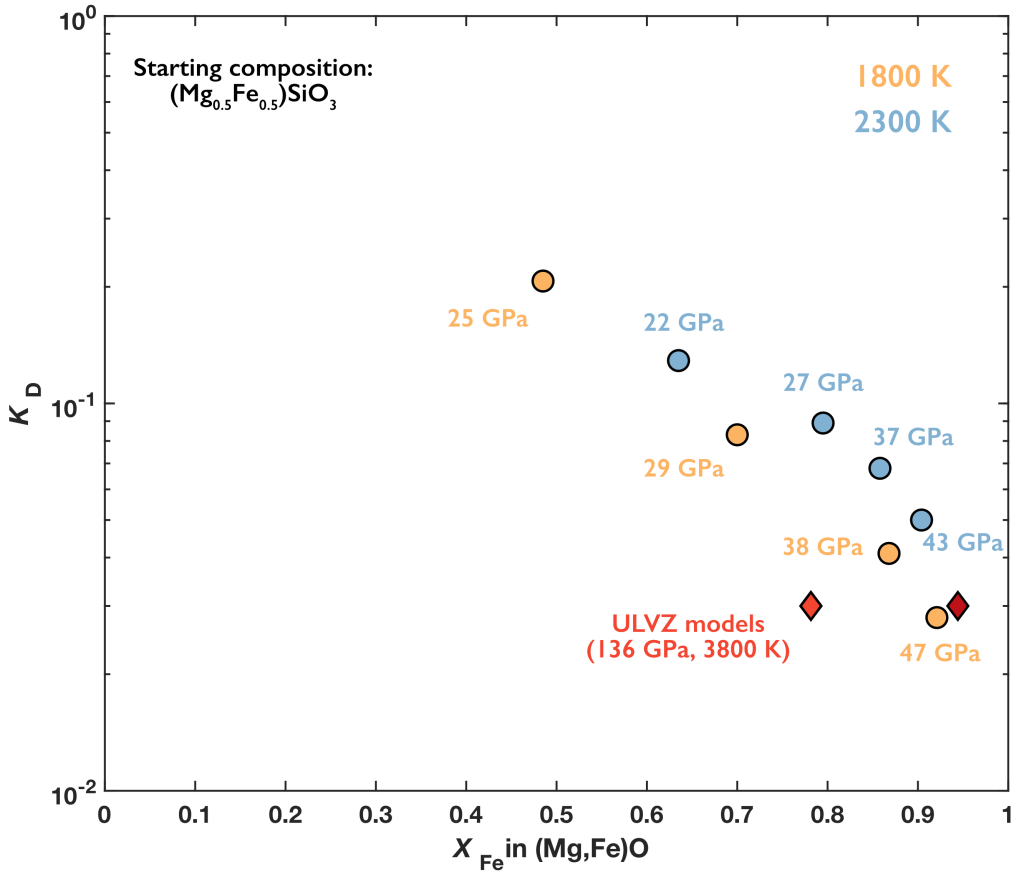

Figure B.1: Fe-Mg distribution coefficients between magnesiowüstite and bridgmanite as a function of iron content in magnesiowüstite. Circles indicate results from Tange et al. (2009) over a range of pressures for two temperatures (yellow – 1800 K, blue – 2300 K). Red diamonds indicate coefficient used to calculate relative iron concentrations among constituent phases in the ULVZ compositional models for assemblages with $(Mg_{0.22}Fe_{0.78})O$ (lighter) and $(Mg_{0.06}Fe_{0.94})O$ (darker) . The choice of coefficient is additionally consistent with recent measurements of iron partitioning in similar iron-rich assemblages (Dorfman et al., 2021).

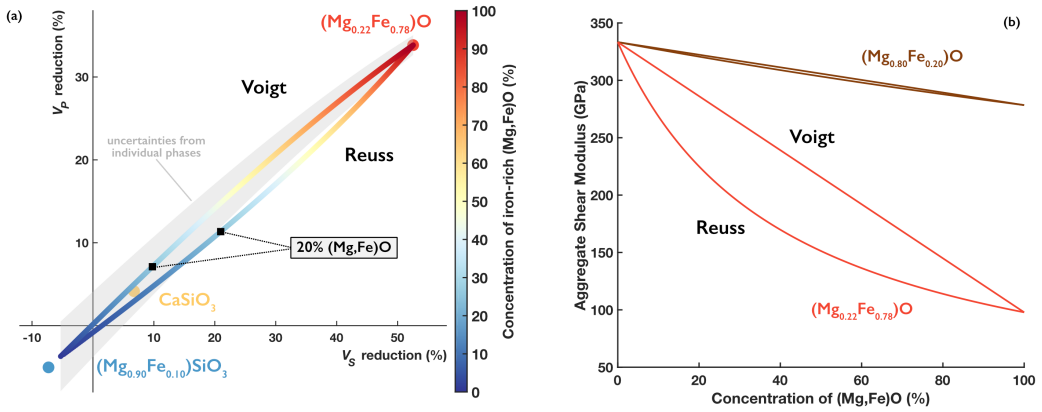

Figure B.2: Voigt and Reuss mixing bounds for aggregates with very slow magnesiowüstite. (a) Colored curves show forward models of aggregate velocities (% reduction relative to IASP) for a magnesiowüstite-bearing solid-state ULVZ, with color indicating relative concentration of magnesiowüstite. Circles indicate relative velocities of $(Mg_{0.22}Fe_{0.78})O$ (red), $(Mg_{0.90}Fe_{0.10})SiO_3$ (blue), and $CaSiO_3$ (yellow). Relative concentrations of $(Mg_{0.90}Fe_{0.10})SiO_3$ and $CaSiO_3$ are held at a constant ratio of 85:15. Gray shading shows uncertainties in aggregate velocities for the Voigt mixing bound propagated from uncertainties of each constituent phase. Black markers (20% concentration of magnesiowüstite) demonstrate large velocity difference between Voigt and Reuss mixing bounds for identical aggregate compositions. (b) Aggregate shear moduli of forward models shown in (a) as a function of (Mg,Fe)O concentration for $(Mg_{0.22}Fe_{0.78})O$ magnesiowüstite (red) and $(Mg_{0.80}Fe_{0.20})O$ ferropericlase (brown). The very low shear modulus of magnesiowüstite leads to large difference in aggregate shear moduli between Voigt and Reuss mixing bounds, unlike for the much faster ferropericlase.

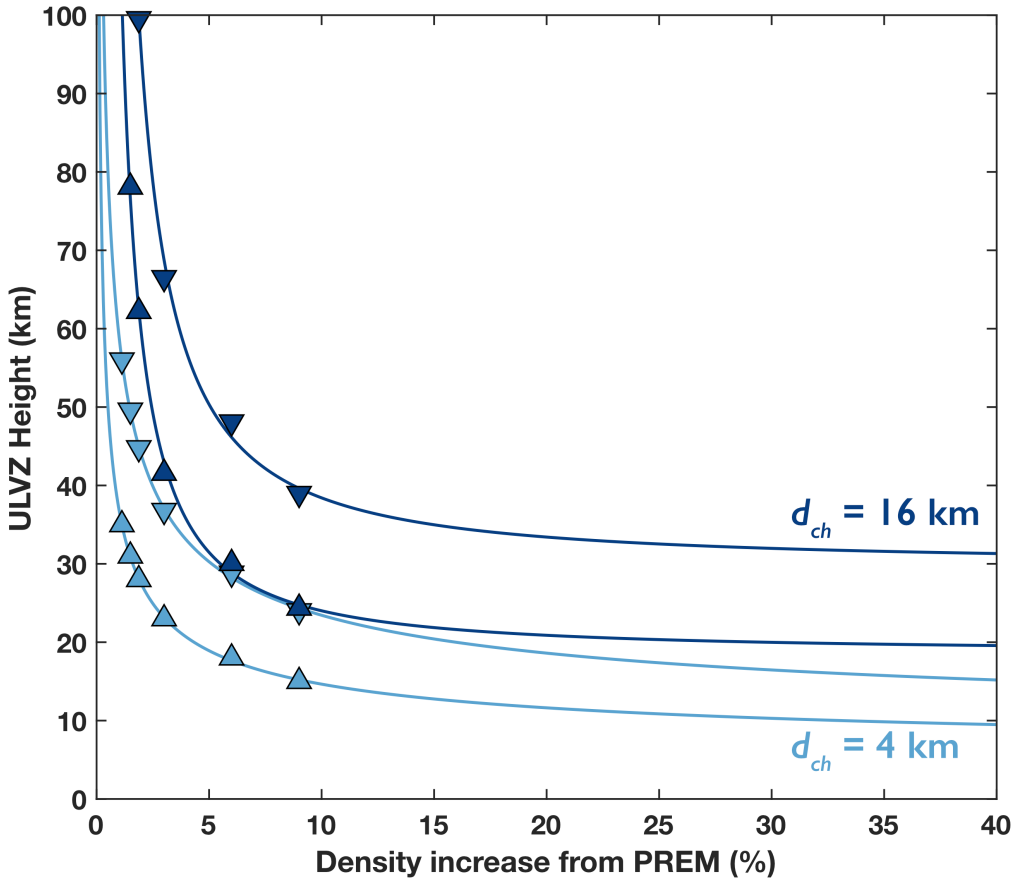

Figure B.3: Published results from geodynamic models of solid-state ULVZs. Upward triangles show lower bounds on heights of solid ULVZs containing low viscosity magnesiowüstite (Reali et al., 2019), as a function of ULVZ density, given initial chemically distinct layers with thickness 4 km (light blue) and 16 km (dark blue). Downward triangles show upper bounds calculated from mid-range estimates of uncertainties in thermal conductivity and lower mantle viscosity (see Bower et al., 2011 for further details). Solid lines show fits to the data using functional form $height = a\,(\Delta\rho)^{-b} + c$, where $\Delta\rho$ is the density increase relative to PREM.

Table B.1: Compressional (V_P) and shear (V_S) wave velocities and densities for the phase assemblages considered here, calculated at CMB conditions (135.8 GPa and 3800 K). Properties of magnesiowüstite phases $(Mg_{0.06}Fe_{0.94})O$ (Mw94) and $(Mg_{0.22}Fe_{0.78})O$ (Mw78) and of calcium silicate perovskite (CaPv) are calculated as described in Dobrosavljevic et al. (2019). Properties of bridgmanite phases $(Mg_{0.68}Fe_{0.32})SiO_3$ (Br32) and $(Mg_{0.90}Fe_{0.10})SiO_3$ (Br10) are calculated as described in Dobrosavljevic et al. (2019) except with updated temperature derivatives from Shukla et al. (2015). Distribution of iron between the magnesiowüstite and bridgmanite phases is calculated using the coefficient shown in Fig. B.1 and discussed in Dobrosavljevic et al. (2019).

	Mw94	Mw78	Br32	Br10	CaPv
V_P (km/s)	8.93 ± 0.14	9.40 ± 0.14	14.07 ± 0.35	14.47 ± 0.36	13.14 ± 0.33
V_S (km/s)	3.46 ± 0.09	3.44 ± 0.09	7.66 ± 0.19	7.84 ± 0.20	6.78 ± 0.34
ρ (g/cm^3)	8.528 ± 0.015	7.888 ± 0.015	5.733 ± 0.057	5.423 ± 0.054	5.494 ± 0.055

Table B.2: Best-fitting inverted ULVZ compositional models. Relative concentrations of $(Mg_{0.06}Fe_{0.94})O$ magnesiowüstite (Mw94) and $(Mg_{0.22}Fe_{0.78})O$ magnesiowüstite (Mw78) coexisting with bridgmanite (Br) and $CaSiO_3$ calcium silicate perovskite (CaPv) for the best fitting ULVZ compositional models (for Voigt and Reuss mixing bounds) calculated with the inversion approach for the preferred 30 km seismic model. Also shown are concentrations of FeO in each assemblage and aggregate velocity reductions relative to IASP and density increases relative PREM at the CMB. Parentheses indicate uncertainties in the last digit for fit parameters.

Compositional Model		X_{Mw} (%)	X_{Br} (%)	X_{CaPv} (%)	mol% FeO	wt% FeO	dV_P (%)	dV_S (%)	dρ(%)
Mw94	Voigt	37(2)	51(4)	12	43(2)	45(2)	-13(2)	-18(2)	+21(1)
	Reuss	20(1)	69(4)	10	30(1)	34(1)	-10(2)	-18(2)	+13(1)
Mw78	Voigt	41(2)	53(4)	6	35(2)	41(2)	-11(2)	-18(2)	+16(1)
	Reuss	21(1)	69(3)	10	20(1)	23(1)	-8(2)	-18(2)	+7(2)

Appendix C

SUPPLEMENTARY MATERIAL FOR CHAPTER 4

C.1 Sample preparation procedures

Samples were synthesized from individual pieces of Ni, Si, and 95%-enriched ^{57}Fe that were arc melted in an argon atmosphere and cold rolled to a uniform thickness of approximately 10 μm. Scanning electron microscopy measurements confirmed a sample composition of $Fe_{0.80(1)}Ni_{0.10(1)}Si_{0.10(1)}$ with a compositional homogeneity at the 1 μm scale. The samples in this study were cut from the same sample batch studied by Morrison et al. (2018), Morrison et al. (2019), who reported the thermoelastic properties of Fe-Ni-Si alloys.

Samples were cut into rectangular sections with lateral dimensions of 30 to 100 μm and loaded in diamond anvil cells (DACs) with diamond culet diameters ranging from 250 to 400 μm. Seats holding the anvils were composed of tungsten carbide on the upstream side of the DAC and carbon boron nitride on the downstream side in order to maximize the accessible 2θ range available for the XRD measurements. Rhenium gaskets serving as sample chambers were pre-indented to a thickness of 45 to 55 μm from a starting thickness of 250 μm. Each gasket was drilled with an electron discharge machine to produce sample chamber diameters ranging from 80 to 165 μm, depending on the diamond culet size. Samples were sandwiched inside the sample chamber between flakes of dehydrated KCl with a minimum thickness of 10 μm that served as both thermal insulation and a pressure transmitting medium. At least one ruby sphere was loaded into the sample chamber without contact with the sample.

Once loaded, each DAC was heated in a vacuum oven for 12 to 24 hours in order to minimize oxygen and moisture in the sample chamber, then subsequently sealed and compressed to its target pressure. Pressures of the sample chamber were estimated before and after each heating run from the fluorescence spectrum of the ruby spheres (Shen et al., 2020), and measured during the heating cycle for the x-ray diffraction measurements. Each heating location on the sample was laser annealed at approximately 1500 K before the heating run for at least 5 minutes in order to determine sample coupling behavior with the infrared heating lasers and to relax any deviatoric stresses induced by the cold compression process. In the

SMS measurements, the annealing time was used to collect a high-quality SMS time spectrum used for fitting the sample's starting effective thickness (Section 4.3.2). We note that all samples in both sets of melting experiments were cut from the same bulk material and prepared using the same loading methods in order to minimize uncertainties arising from variability in sample characteristics and preparation procedures.

C.2 Temperature-laser power relationships

The relationship between sample temperature and incident laser power has been used in some previous melting studies as a proxy method for detecting the onset of melting, with observations including both a plateau in temperature as well as a discontinuous jump in temperature with increasing laser power (e.g., Asanuma et al., 2010; Lord et al., 2010. The plateau in temperature has been suggested to be caused by latent heat of melting (Lord et al., 2010), while the discontinuous jump has been attributed to a change in heating efficiency due to increased absorptivity of the liquid melt relative to the solid sample (Asanuma et al., 2010). Numerical modeling of heat flow inside a typical laser-heated DAC assemblage (Geballe & Jeanloz, 2012) has suggested that the latent heat of melting is likely too weak to be detected in experiments with heating times longer than ~1 millisecond, much faster than those in this study and the above referenced studies. Instead, changes in temperature – laser power relationships are suggested to be explainable by changes most likely in absorptivity/reflectivity or possibly in thermal conductivity of the sample. However, as discussed by Geballe and Jeanloz (2012), absorptivity changes are not an intrinsic quality of the sample and may be caused by phenomena other than melting. This suggestion is supported by several studies that detected melting via diffuse XRD scattering but did not observe a consistent discontinuity in the temperature – laser power relationship at melting (e.g., Anzellini et al., 2013; Parisiades et al., 2019; Stutzmann et al., 2015).

In this study we find that discontinuities in sample temperature as a function of incident laser power cannot be used consistently as a proxy for the onset of melting. In Fig. C.1 we show examples of typical temperature – laser power profiles for SMS and XRD measurements. SMS heating runs generally exhibit a monotonic increase in temperature beyond the melting temperature that is constrained by the loss of the Mössbauer signal, followed by a peak and small plateau at a higher temperature, followed by a decrease in temperature that approaches the melting temperature. There may be a subtle change in the slope of temperature vs laser

power at melting that is difficult to identify without prior knowledge of the melting temperature location. For XRD measurements, we see complicated and variable behavior across the heating runs. We show two representative examples in Fig. C.1. For run D1P2S3, we observe a small jump in temperature followed by a plateau in temperature slightly above the melting temperature determined by the onset of the diffuse scattering signal. For run D6P1S1, we observe a possible small plateau in temperature followed by an increase of variable slope. As with the SMS measurements, melting temperatures in XRD runs would be challenging to determine from temperature – laser power profiles and may lead to overestimation of the melting temperature. A similar combination of temperature jumps and plateaus was observed by Asanuma et al. (2010) in the melting of Fe-Si.

C.3 Choice of background regions for detecting liquid diffuse signals

In order to explore whether the choice of the narrow low-angle region for background integration is the most effective choice for detecting a small liquid diffuse signal, we consider several other approaches. Firstly, we follow the same approach outlined in the main text but for a nearby low-angle region, shown in Fig. C.16. This region is similarly close to the lowest order sample Bragg reflections, with the difference that there are stronger noisy fluctuations in the quenched patterns, likely due to the proximity of the *fcc* (111) reflection, which recrystallizes at high temperatures and remains present in many of the quenched patterns due to the sluggish back-transformation during quench from *hcp* to *fcc*. For this region, we find that we can detect a liquid diffuse signal at the same exact temperature as for the originally chosen low-angle region. However, we do see more scatter in the normalized background intensities, due to noisy fluctuations in this background region (Fig. C.16d).

We additionally explore an alternate approach that considers the background shapes of the full XRD pattern. To do so, we use the DIOPTAS software (Prescher & Prakapenka, 2015) to fit the background shapes for each hot and cold XRD pattern in heating run D1P2S3 (the same run considered as an example in the main text and Fig. 4.4). We show an example of the background fit in Fig. C.17a and the full suite of background fits for hot and cold patterns in Fig. C.17b and C.17c, respectively. We then follow a similar procedure of normalizing each hot pattern background by the corresponding cold quenched pattern background. This approach is similar to the background updating approach taken in the main text analysis, except that we are now considering fits to the full background instead of the actual intensities of

narrow background regions.

We plot the normalized background fits in Fig. C.17d, along with shaded bars indicating the low-angle and high-angle regions integrated in the main text analysis. We find that there is an apparent onset of the characteristic main and secondary oscillations of the liquid structure factor (e.g., Kuwayama et al., 2020) that mark the presence of the liquid diffuse signal from the melt. We note that the low-angle region chosen in the main text aligns well with the strongest intensities of the liquid diffuse signal.

In order to determine whether this background fitting approach provides more useful information than the approach in the main text, we similarly integrate the intensities of the normalized background fits for several regions. These regions include the full 2θ range of the XRD patterns, the same low-angle region from the main text, and the same high-angle region from the main text where no liquid diffuse signal is expected to be observable. We plot the results in Fig. C.17e. As can be seen, no liquid diffuse signal is observable in the high-angle region, as expected. Similarly, no liquid diffuse signal can be identified when considering the full 2θ range. The reason for this is that the liquid diffuse signal is small and detectable only in a narrow scattering angle region – the region around the sample's lowest order Bragg reflections. Finally, the low-angle region may show some discontinuous increase in background intensity. However, the increase is more difficult to identify clearly in this analysis, and the exact onset of the liquid diffuse signal is difficult to constrain precisely without prior knowledge of the melting temperature. Indeed, simply looking at the integrated intensities from these background fits may lead to overestimated melting temperatures, depending on how the linear trend before melting is interpreted.

These finding suggests that the fits to the background shapes do not capture all of the details in the actual raw diffraction patterns, and that these details are in fact valuable for precisely quantifying the onset of liquid diffuse scattering and avoiding overestimated melting temperatures. Given these findings, we suggest that the approach taken in the main text (choosing a narrow low-angle region and following the normalization procedure) leads to the best sensitivity to a small liquid diffuse signal and allows for the best precision in constraining the melting temperatures without overestimation. Accordingly, we apply this procedure for all burst heating runs in our XRD data set for final determination of melting temperatures (Figs. C.2-C.8).

C.4 Equations of state

In-situ pressures are calculated from unit-cell volumes using previously published thermal equations of state. For B2-KCl, we use a recently reported thermal equation of state (Tateno et al., 2019) and assume a KCl temperature identical to that of the average sample surface temperature (discussed further in Text C.5). For *hcp*-$Fe_{0.80(1)}Ni_{0.10(1)}Si_{0.10(1)}$, Morrison et al. (2018) measured the isothermal compression of this identical material in a helium pressure medium. More recently, Komabayashi, Pesce, Sinmyo, et al. (2019) calculated two equation of state models for a nearly identical composition: Model B using results from Morrison et al. (2018), and Model A using results from previous studies with stiffer SiO_2 pressure media. Due to the relative stiffness of KCl compared to helium, we use Model A for calculating *hcp* phase pressures, with thermal parameters previously measured for pure iron by Murphy et al. (2011), following Morrison et al. (2018). The compatibility of both models with compression data within mutual uncertainties, which differ primarily in the fitting tradeoff between K_0 and K'_0, is supported by results from a recent compression study on a nearly identical composition (Edmund et al., 2020). For *fcc*-$Fe_{0.80(1)}Ni_{0.10(1)}Si_{0.10(1)}$, we follow Komabayashi (2014) in assuming the same K_0 and K'_0, as the *fcc* phase, adjusting the V_0 using the *hcp*/*fcc* V_0 ratio for pure iron, and determining thermal parameters by refitting the *fcc*-Fe data compiled by Komabayashi (2014). These equations of state (Table C.2) result in excellent agreement between $Fe_{0.80(1)}Ni_{0.10(1)}Si_{0.10(1)}$ and KCl pressures, consistently within 1-2 GPa at both high and ambient temperatures (Figs. C.2-C.10).

C.5 Thermal pressure modeling

As described in Section 4.3.3, we calculate a thermal pressure model of 2.9 GPa per 1000 K for $Fe_{0.80(1)}Ni_{0.10(1)}Si_{0.10(1)}$ loaded in KCl by fitting a compilation of all thermal pressure measurements of $Fe_{0.80(1)}Ni_{0.10(1)}Si_{0.10(1)}$ in this study. For the fit, we use only *hcp*-$Fe_{0.80(1)}Ni_{0.10(1)}Si_{0.10(1)}$, as the *fcc* data exhibit more scatter due to recrystallization during heating and due to significant changes in volume and pressure at and above melting (Fig. 4.7). This fit is in excellent agreement with the fit to all thermal pressure data for KCl in this study (Fig. 4.7), where we assume a KCl temperature identical to the sample surface temperature. Fits to thermal pressures for individual heating runs demonstrate no pressure dependence of the thermal pressure slope (Fig. C.19). In order to determine appropriate uncertainties on pressures at melting when applying this thermal pressure model to the SMS measurements, we examine consequences of KCl temperature uncertainty and compare to previous

studies that reported *in-situ* pressures of heated Fe sample loaded in KCl.

The true temperature and temperature distribution of the KCl pressure medium is uncertain but can be bounded by known temperatures in the sample chamber. As described by Campbell et al. (2009), the sample surface temperature should represent an upper bound, while an average of the sample surface temperature and the diamond culet temperature (300 K) should represent a lower bound. In our calculation of KCl pressures, we use the sample surface temperature (upper bound), because it is the most proximal temperature measurement of the sample and, as stated above, leads to excellent agreement with *in-situ* measurements of the $Fe_{0.80(1)}Ni_{0.10(1)}Si_{0.10(1)}$ sample pressure evolution during heating. Nevertheless, we explore this particular temperature uncertainty. We recalculate KCl pressures assuming the lower bound temperature (average of sample surface and 300 K) and fit the recalculated thermal pressures (Fig. C.20), resulting in a slope of 2.1±0.5 GPa per 1000 K. For a melting temperature of 3000 K, this would result in a thermal pressure contribution of around 5 GPa, compared to the 8 GPa suggested by our original thermal pressure model of 2.9 GPa per 1000 K. For modeling the melting pressures in the SMS measurements and to account for the uncertainty in KCl temperatures, we use the original thermal pressure model, for reasons stated above and add an uncertainty of 3 GPa to the resulting melting pressures; this 3 GPa uncertainty is in addition to the uncertainty on the starting cold pressures for the SMS measurements.

We compare to previous *in-situ* pressures reported for Fe loaded in KCl. We compile pressure data for Fe and for the KCl pressure medium reported by Anzellini et al. (2013), calculated as pressure increase relative to the first reported measurement as a function of temperature increase relative to the first reported measurement, as the authors do not report 300 K pressures. We fit these thermal pressure compilations to constrain the temperature dependence: 3.6±0.7 GPa per 1000 K for the Fe pressures and 2.1±0.3 GPa per 1000 K for the KCl pressures (Fig. C.20-C.21). We note that Anzellini et al. (2013) similarly assumed a KCl temperature identical to the sample surface temperature. We also consider the thermal pressure reported by Sinmyo et al. (2019) for a thin Fe foil in KCl, who constrained a slope of 4 GPa per 1000 K (Fig. C.20). Including the 3 GPa uncertainty at melting (2500-3000 K), all of the above thermal pressure slopes are in agreement with our thermal pressure model. We note that our thermal pressure model accounts for the uncertainty in KCl temperatures, as discussed above. Given these findings, we apply this thermal pressure model to the SMS measurements, as discussed in Section 4.3.3 and Text

C.7.

Finally, we consider thermal pressure data published for $Fe_{0.9}Ni_{0.1}$ by D. Zhang et al. (2016), also included in Fig. C.20. Those thermal pressures fall somewhat higher at lower temperatures (<1500 K), while exhibiting relatively good agreement with our thermal pressure model at higher temperatures (>1500 K). We note that the data set from D. Zhang et al. (2016) is limited to temperatures below 2000 K. Given the smaller temperature range of that data set and the relatively good agreement at the higher temperatures (1500 – 2000 K), we apply our thermal pressure model to the published melting results for $Fe_{0.9}Ni_{0.1}$, as discussed in Text C.7. Using an identical thermal pressure model for SMS melting results on Fe, $Fe_{0.9}Ni_{0.1}$, and $Fe_{0.8}Ni_{0.1}Si_{0.1}$, all measured using identical experimental methods at the same beamline, represents a systematic approach for precisely constraining the combined effect of alloyed-Ni and Si on the melting temperatures of Fe.

C.6 Error analysis for calculating phase boundaries and the triple point locations

Fits to phase boundary data points for both the melting curve and the solid *hcp/fcc* transition are calculated using a weighted least squares method, where the weighting for each data point is calculated as the squared inverse of the temperature uncertainty. The melting curve is fit using the Simon-Glatzel relationship (Section 4.3.4), while the *hcp-fcc* transition is fit using a linear relationship. The reported uncertainties on the resulting fit parameters are calculated at the 1-σ uncertainty level. The shaded uncertainty bounds shown for the phase boundary fits (Fig. 4.8) are calculated as the root-mean-square of the uncertainty in the phase boundary shape from the fit at the 1-σ uncertainty level and the average temperature uncertainty for the phase boundary data points. The location of the *hcp-fcc-liquid* quasi-triple point is calculated as the intersection of the melting curve and *hcp/fcc* boundary. The uncertainty in the triple point temperature is calculated as the uncertainty in the melting curve temperature at the triple point location, calculated as described above. The uncertainty in the triple point pressure is calculated as an average of the range of pressures spanned by the uncertainty in the *hcp/fcc* boundary line (shaded region) along the melting curve and the range of pressures spanned by the shaded uncertainty bound of the melting curve at the triple point temperature. We follow an identical procedure in the refitting of Fe and Fe0.9Ni0.1 melting curves and recalculation of *hcp-fcc-liquid* (quasi-) triple points for those phases, as described in Text C.7 and shown in Fig. 4.9.

C.7 Recalculating melting pressures from previous studies and refitting melting curves of *fcc*-Fe and *fcc*-$Fe_{0.9}Ni_{0.1}$

Melting pressures for published SMS results (Jackson et al., 2013; D. Zhang et al., 2016) are recalculated using reported cold pressures before heating and the new thermal pressure model (2.9 GPa per 1000 K), with a 3 GPa uncertainty added to the cold pressure uncertainties, as discussed in Text C.5. We use the Simon-Glatzel formulation $T_m = T_{m0}\left(\frac{P_m - P_{m0}}{x} + 1\right)^y$ to fit a melting curve of *fcc*-Fe to the recalculated SMS dataset, using the lowest pressure SMS data point as an anchor point (P_{m0}, T_{m0}) . We find best-fitting parameters of x=28±15 and y=0.31±0.14, with a fit quality of $R^2 = 0.94$. We calculate an *hcp-fcc-liquid* triple point location for pure Fe to be at 110±10 GPa and 3380±130 K (Fig. 4.9a). Treatment of uncertainties and error propagation follows the procedure described in Text C.6. For the *hcp/fcc* phase boundary taken from Komabayashi et al. (2009), we assume an uncertainty of ±80 K to account for the width of the phase coexistence region reported in that study. For Fe-Ni, we fit SMS data from D. Zhang et al. (2016) on *fcc*-$Fe_{0.9}Ni_{0.1}$ using recalculated melting pressures (Fig. 4.9b). We use the Simon-Glatzel formulation and find best-fitting parameters of x=16±2 and y=0.30±0.02, with a fit quality of R^2 = 0.98. For this fit, we use the 0 GPa melting data point from von Goldbeck (1982) as an anchor point, as $Fe_{0.9}Ni_{0.1}$ crystallizes in the *fcc* structure at 0 GPa, unlike for pure Fe, where the *bcc* structure is stable at 0 GPa. We calculate an *hcp-fcc-liquid* quasi-triple point location for $Fe_{0.9}Ni_{0.1}$ at 125±8 GPa and 3440±90 K. Treatment of uncertainties and error propagation follows the procedure described in Text C.6. For the *hcp/fcc* phase boundary taken from Komabayashi et al. (2012), we assume an uncertainty of ±80 K to account for the width of the phase coexistence region reported in that study.

Table C.1: Phase boundary conditions from all heating runs. Techniques XRDb and XRDc correspond to burst and continuous XRD heating modes, respectively. η represents the starting effective thickness used in the SMS fitting procedure (Section 4.3.2). Effective thickness is dimensionless and is the product of the numerical density of the ^{57}Fe atoms, the physical thickness of the sample, the nuclear resonant cross-section ($2.56\text{x}10^{-22}$ m^2 for ^{57}Fe), and the Lamb-Mössbauer factor (probability of recoil-free scattering events). Melting temperatures are determined by loss of the Mössbauer signal (SMS), onset of a liquid diffuse scattering signal (XRDb), or onset of a plateau in volumes (XRDc). The offset between the x-ray beam and the laser hotspot at melting is caused by thermal expansion of the laser optics during heating and is fit during the SMS fitting procedure. Uncertainties are shown in parentheses.

Heating Run	Technique	P (GPa)	T_{melt} (K)	P (GPa)	$T_{hcp\text{-}fcc}$ (K)	η	Offset (μm)	Reduced χ^2
D9S1	SMS	23.9(4)	1980(80)			110	7(2)	0.46(15)
D9S2	SMS	23.7(4)	1915(90)			214	6(1)	0.77(18)
CP4S1	SMS	36.1(3.4)	2310(140)			90	7(2)	0.49(13)
CP4S2	SMS	36.5(4)	2310(80)			82	7(2)	0.98(20)
D1S1	SMS	45.2(4.4)	2530(95)			97	14(3)	1.92(22)
D1S2	SMS	45.2(4.5)	2560(80)			63	11(3)	2.93(30)
D6S1	SMS	55.2(3.4)	2590(95)			96	17(4)	2.21(22)
D6S2	SMS	55.5(4)	2580(80)			94	14(3)	3.72(23)
D7c	SMS	73.2(3.8)	2745(65)			100	14(3)	3.14(20)
D1P1S1	XRDb	49.5(3.5)	2570(75)	48.8(2)	2025(75)			
D1P1S2	XRDb	47.4(2.1)	2450(100)	44.8(2.1)	1900(80)			
D1P1cM	XRDc	48.4(3)	2570(70)	48.9(1.6)	2030(60)			
D1P2S3	XRDb	55.8(1.6)	2410(110)	54.8(12)	2070(70)			
D1P2S4	XRDb	55.1(2.3)	2500(100)	51.8(2.7)	2025(100)			
D1P2S5	XRDb	53.6(2)	2520(80)	51.6(2)	2040(85)			
D6P1S1	XRDb	73.0(1.7)	2660(60)	75.9(2)	2250(50)			
D6P1S2	XRDb	69.6(2.1)	2600(150)	71.3(2.1)	2280(75)			
D6P2S3	XRDb	82.6(1.7)	2805(85)	82(2.1)	2380(105)			
D6P2S4	XRDc	78.9(2)	2720(120)	78.7(2.9)	2385(90)			

Table C.2: Parameters for thermal (Vinet) equations of state (Mie-Grüneisen-Debye formulation) used to calculate *in-situ* pressures from unit-cell volumes during heating runs. See Section 4.3.3 and Text C.4 for details and references.

Phase	V_0 (Å^3)	K_{0T} (GPa)	K'_{0T}	γ_0	q	Θ_0 (K)
hcp-$Fe_{0.8}Ni_{0.1}Si_{0.1}$	22.6	165	5.4	2.0	1.0	417
fcc-$Fe_{0.8}Ni_{0.1}Si_{0.1}$	45.6	165	5.4	2.53	2.07	417
*B*2-KCl	54.5	18.3	5.6	2.30	0.80	235

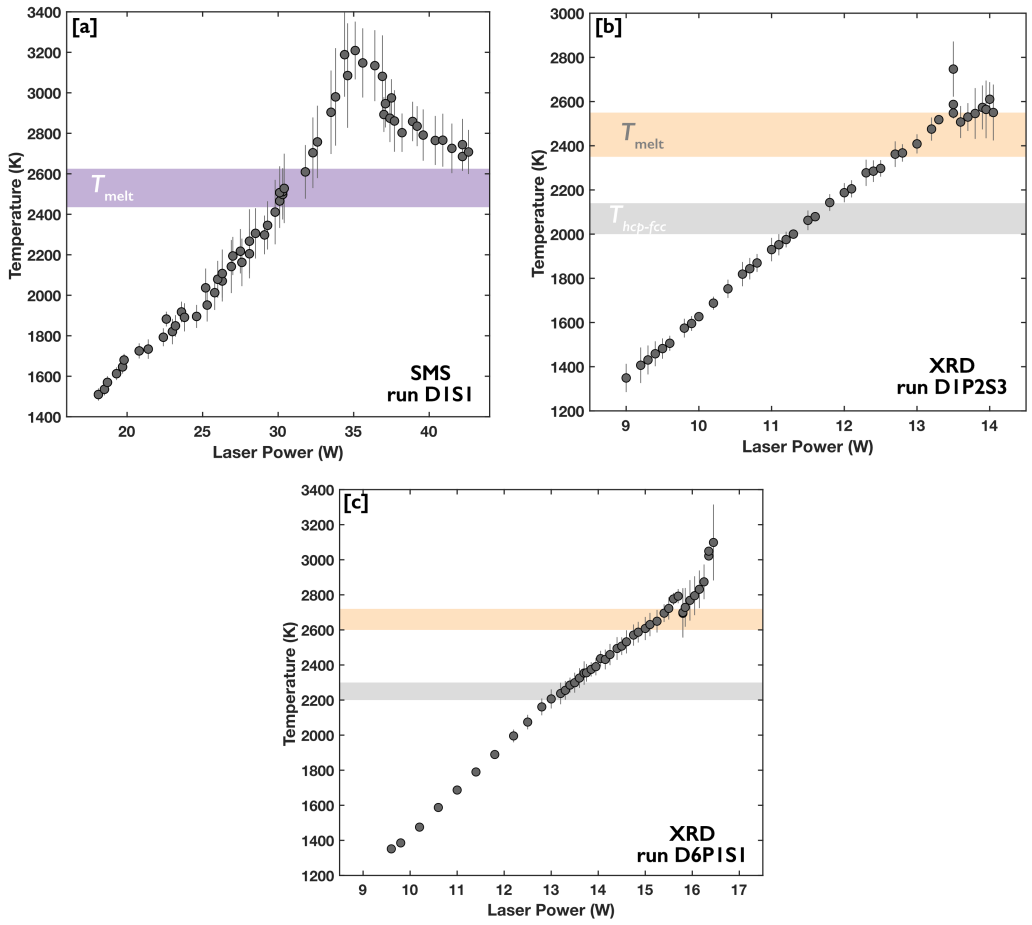

Figure C.1: Representative profiles of sample temperature as a function of incident laser power for SMS run D1S1 [a], XRD run D1P2S3 [b], and XRD run D6P1S1 [c]. See Table C.1 for more details. The purple bar in [a] represents the melting temperature determined by the loss of the Mössbauer signal, while the orange bars in [b] and [c] represent melting temperatures determined by the onset of the liquid diffuse scattering signal. Gray bars in [b] and [c] represent the *hcp-fcc* transition.

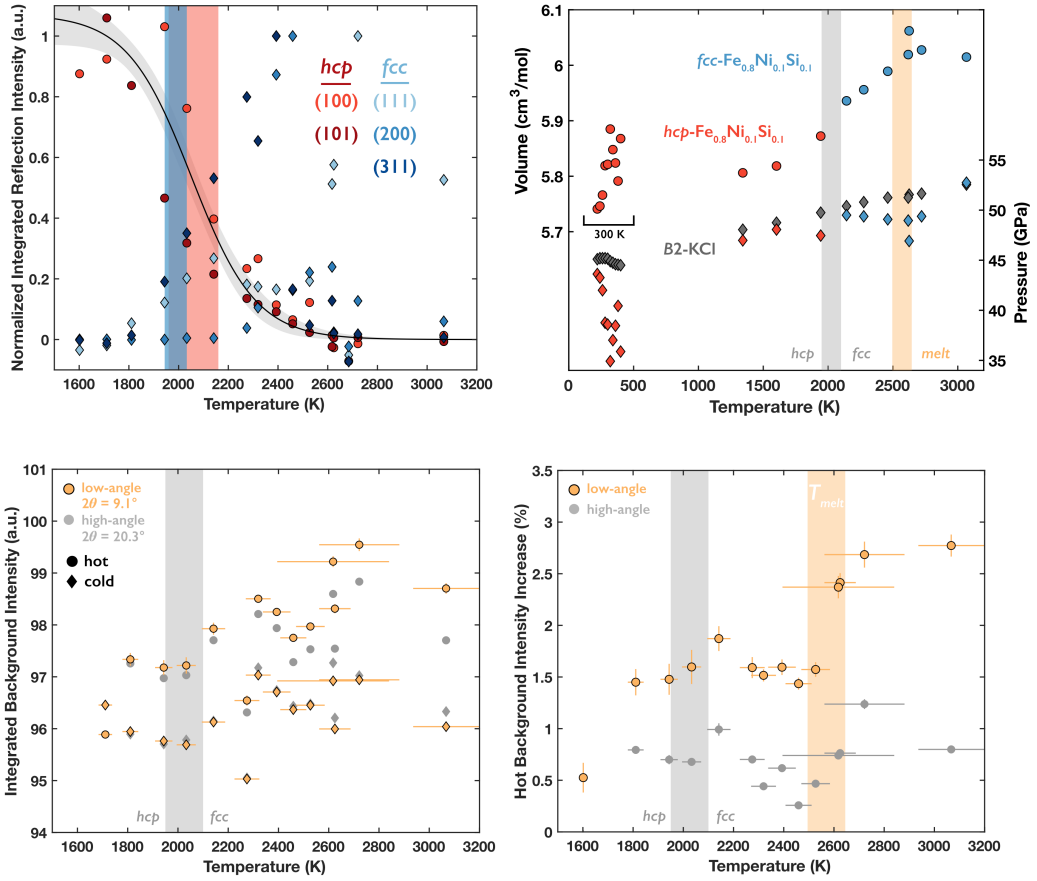

Figure C.2: Burst XRD heating run D1P1S1. Top left: Changes in normalized integrated intensities from multiple *hcp*- (red) and *fcc*-$Fe_{0.8}Ni_{0.1}Si_{0.1}$ (blue) reflections. Shaded bars represent *hcp*-out (red) and *hcp*-in (blue) temperatures. Top right: Unit-cell volumes (left y-axis and circles) and pressures (right y-axis and diamonds) for *hcp*- (red) and *fcc*-$Fe_{0.8}Ni_{0.1}Si_{0.1}$ (blue) and *B*2-KCl (gray). 300 K measurement results are spaced out for ease of viewing in the order of acquisition sequence, from first (leftmost) to last (rightmost) heat and quench step. Shaded bars represent *hcp-fcc* transition (gray) and melting temperature (orange) for this and subsequent panels. Bottom left: Integrated background intensities at low-angle (orange points) and high-angle (gray points) regions for hot (circles) and cold (diamonds) patterns. Bottom right: Normalized background intensities after the background updating procedure (Section 4.3.2) for the low-angle (orange) and high-angle (gray) regions. See Table C.1 for further details.

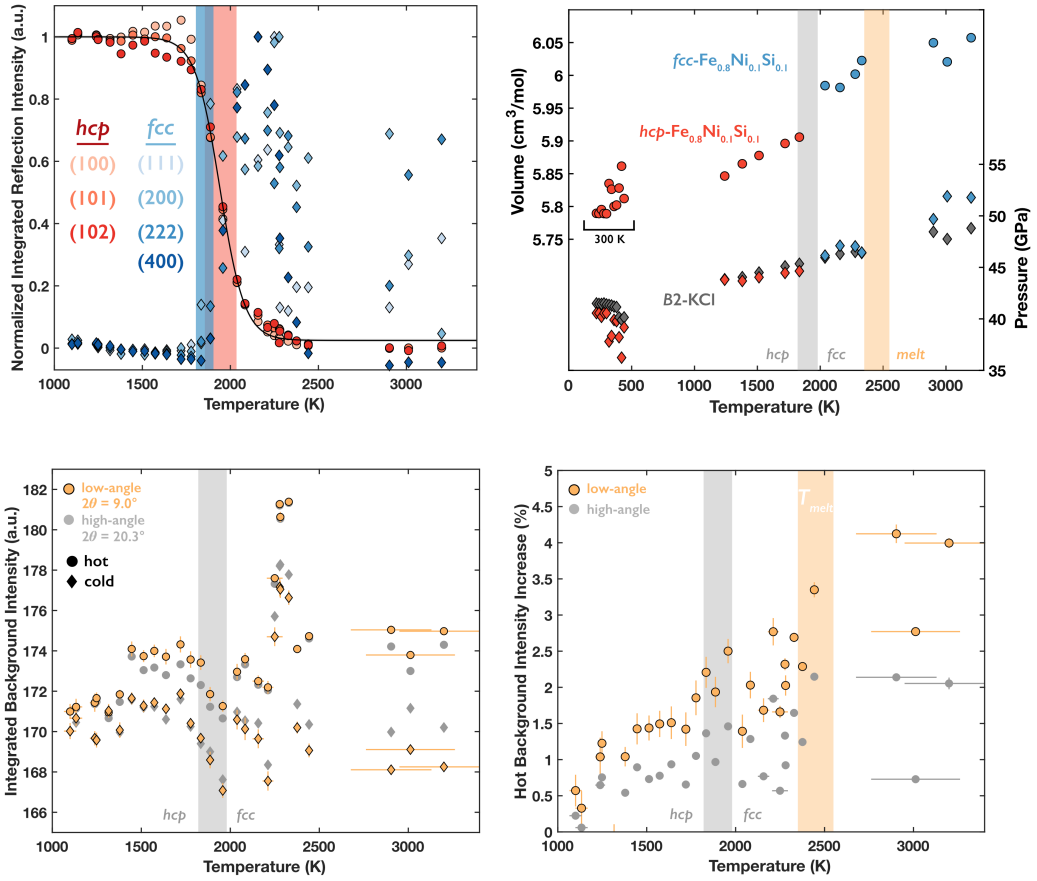

Figure C.3: Burst XRD heating run D1P1S2. Top left: Changes in normalized integrated intensities from multiple *hcp*- (red) and *fcc*-$Fe_{0.8}Ni_{0.1}Si_{0.1}$ (blue) reflections. Shaded bars represent *hcp*-out (red) and *hcp*-in (blue) temperatures. Top right: Unit-cell volumes (left y-axis and circles) and pressures (right y-axis and diamonds) for *hcp*- (red) and *fcc*-$Fe_{0.8}Ni_{0.1}Si_{0.1}$ (blue) and *B*2-KCl (gray). 300 K measurement results are spaced out for ease of viewing in the order of acquisition sequence, from first (leftmost) to last (rightmost) heat and quench step. Shaded bars represent *hcp-fcc* transition (gray) and melting temperature (orange) for this and subsequent panels. Bottom left: Integrated background intensities at low-angle (orange points) and high-angle (gray points) regions for hot (circles) and cold (diamonds) patterns. Bottom right: Normalized background intensities after the background updating procedure (Section 4.3.2) for the low-angle (orange) and high-angle (gray) regions. See Table C.1 for further details.

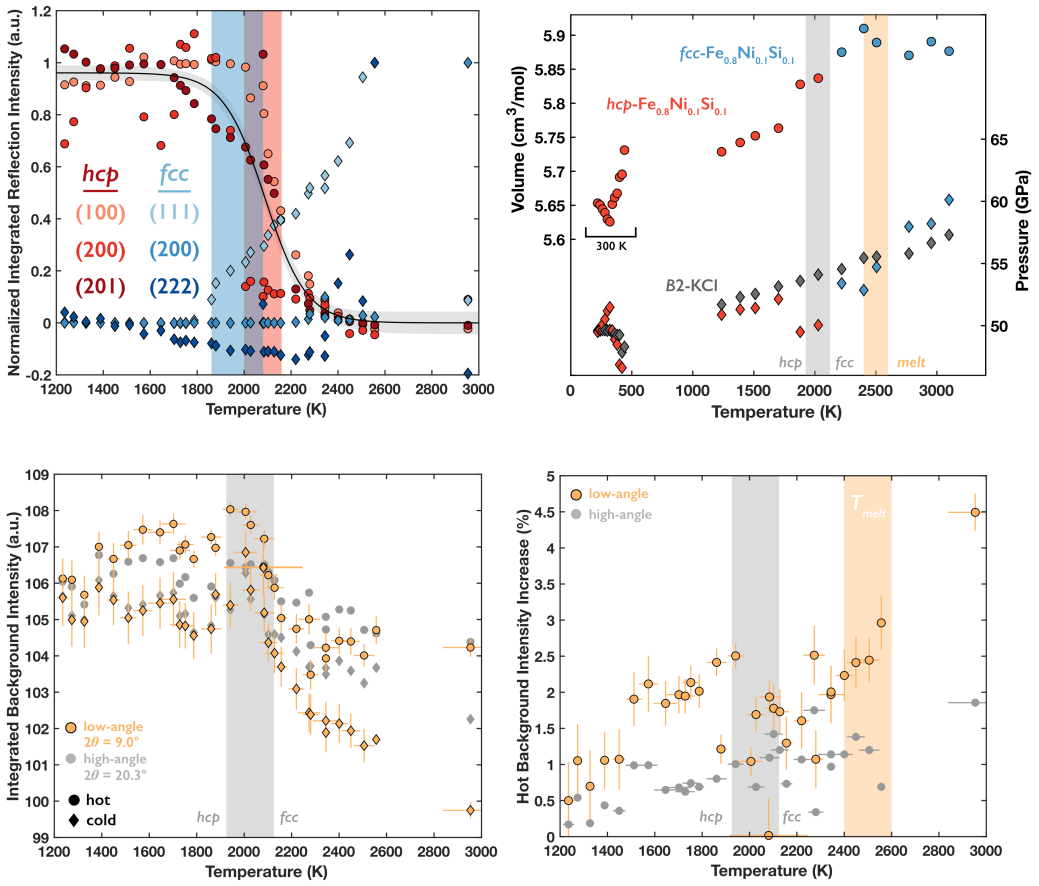

Figure C.4: Burst XRD heating run D1P2S4. Top left: Changes in normalized integrated intensities from multiple *hcp*- (red) and *fcc*-$Fe_{0.8}Ni_{0.1}Si_{0.1}$ (blue) reflections. Shaded bars represent *hcp*-out (red) and *hcp*-in (blue) temperatures. Top right: Unit-cell volumes (left y-axis and circles) and pressures (right y-axis and diamonds) for *hcp*- (red) and *fcc*-$Fe_{0.8}Ni_{0.1}Si_{0.1}$ (blue) and *B*2-KCl (gray). 300 K measurement results are spaced out for ease of viewing in the order of acquisition sequence, from first (leftmost) to last (rightmost) heat and quench step. Shaded bars represent *hcp-fcc* transition (gray) and melting temperature (orange) for this and subsequent panels. Bottom left: Integrated background intensities at low-angle (orange points) and high-angle (gray points) regions for hot (circles) and cold (diamonds) patterns. Bottom right: Normalized background intensities after the background updating procedure (Section 4.3.2) for the low-angle (orange) and high-angle (gray) regions. See Table C.1 for further details.

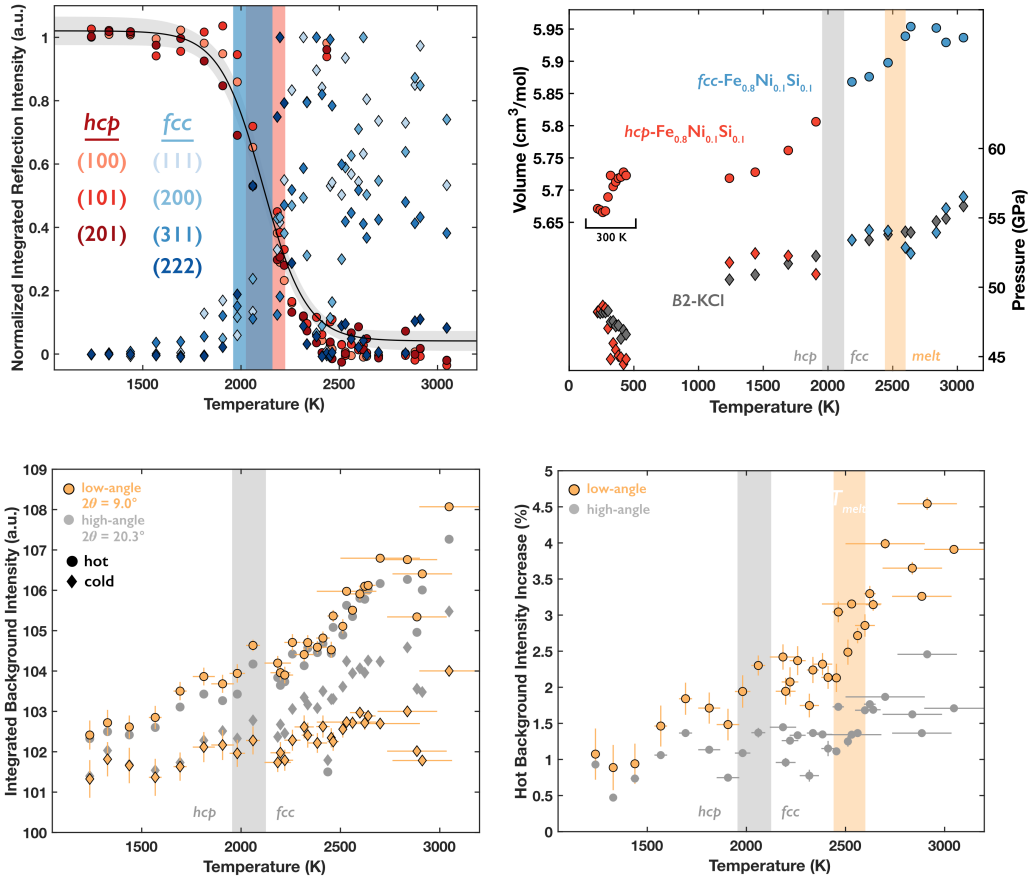

Figure C.5: Burst XRD heating run D1P2S5. Top left: Changes in normalized integrated intensities from multiple *hcp*- (red) and *fcc*-$Fe_{0.8}Ni_{0.1}Si_{0.1}$ (blue) reflections. Shaded bars represent *hcp*-out (red) and *hcp*-in (blue) temperatures. Top right: Unit-cell volumes (left y-axis and circles) and pressures (right y-axis and diamonds) for *hcp*- (red) and *fcc*-$Fe_{0.8}Ni_{0.1}Si_{0.1}$ (blue) and *B*2-KCl (gray). 300 K measurement results are spaced out for ease of viewing in the order of acquisition sequence, from first (leftmost) to last (rightmost) heat and quench step. Shaded bars represent *hcp-fcc* transition (gray) and melting temperature (orange) for this and subsequent panels. Bottom left: Integrated background intensities at low-angle (orange points) and high-angle (gray points) regions for hot (circles) and cold (diamonds) patterns. Bottom right: Normalized background intensities after the background updating procedure (Section 4.3.2) for the low-angle (orange) and high-angle (gray) regions. See Table C.1 for further details.

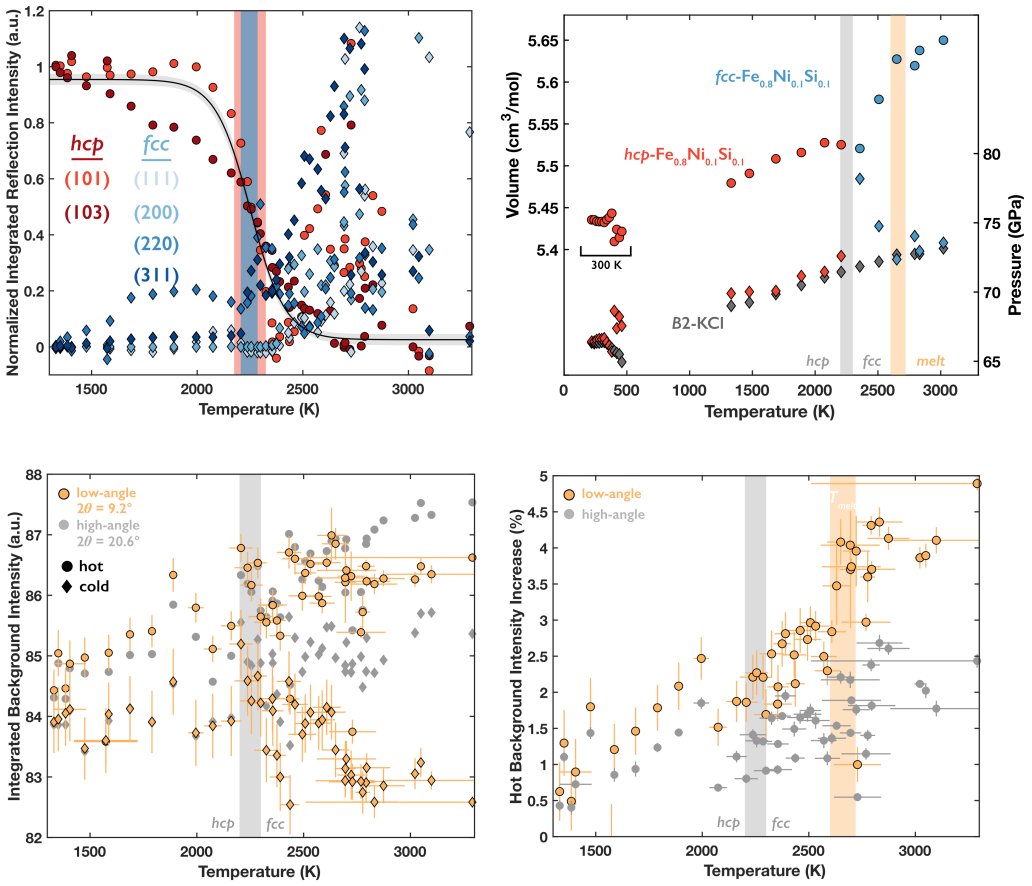

Figure C.6: Burst XRD heating run D6P1S1. Top left: Changes in normalized integrated intensities from multiple *hcp*- (red) and *fcc*-$Fe_{0.8}Ni_{0.1}Si_{0.1}$ (blue) reflections. Shaded bars represent *hcp*-out (red) and *hcp*-in (blue) temperatures. Top right: Unit-cell volumes (left y-axis and circles) and pressures (right y-axis and diamonds) for *hcp*- (red) and *fcc*-$Fe_{0.8}Ni_{0.1}Si_{0.1}$ (blue) and *B*2-KCl (gray). 300 K measurement results are spaced out for ease of viewing in the order of acquisition sequence, from first (leftmost) to last (rightmost) heat and quench step. Shaded bars represent *hcp-fcc* transition (gray) and melting temperature (orange) for this and subsequent panels. Bottom left: Integrated background intensities at low-angle (orange points) and high-angle (gray points) regions for hot (circles) and cold (diamonds) patterns. Bottom right: Normalized background intensities after the background updating procedure (Section 4.3.2) for the low-angle (orange) and high-angle (gray) regions. See Table C.1 for further details.

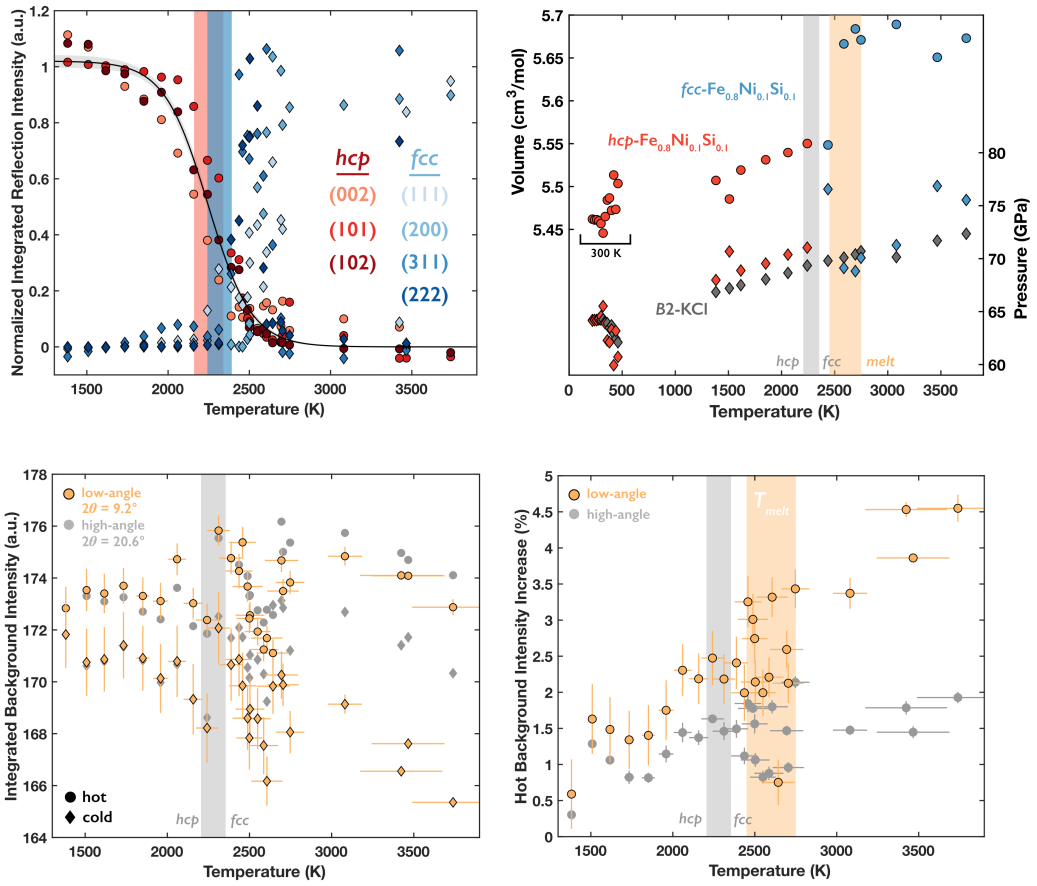

Figure C.7: Burst XRD heating run D6P1S2. Top left: Changes in normalized integrated intensities from multiple *hcp*- (red) and *fcc*-$Fe_{0.8}Ni_{0.1}Si_{0.1}$ (blue) reflections. Shaded bars represent *hcp*-out (red) and *hcp*-in (blue) temperatures. Top right: Unit-cell volumes (left y-axis and circles) and pressures (right y-axis and diamonds) for *hcp*- (red) and *fcc*-$Fe_{0.8}Ni_{0.1}Si_{0.1}$ (blue) and *B*2-KCl (gray). 300 K measurement results are spaced out for ease of viewing in the order of acquisition sequence, from first (leftmost) to last (rightmost) heat and quench step. Shaded bars represent *hcp-fcc* transition (gray) and melting temperature (orange) for this and subsequent panels. Bottom left: Integrated background intensities at low-angle (orange points) and high-angle (gray points) regions for hot (circles) and cold (diamonds) patterns. Bottom right: Normalized background intensities after the background updating procedure (Section 4.3.2) for the low-angle (orange) and high-angle (gray) regions. See Table C.1 for further details.

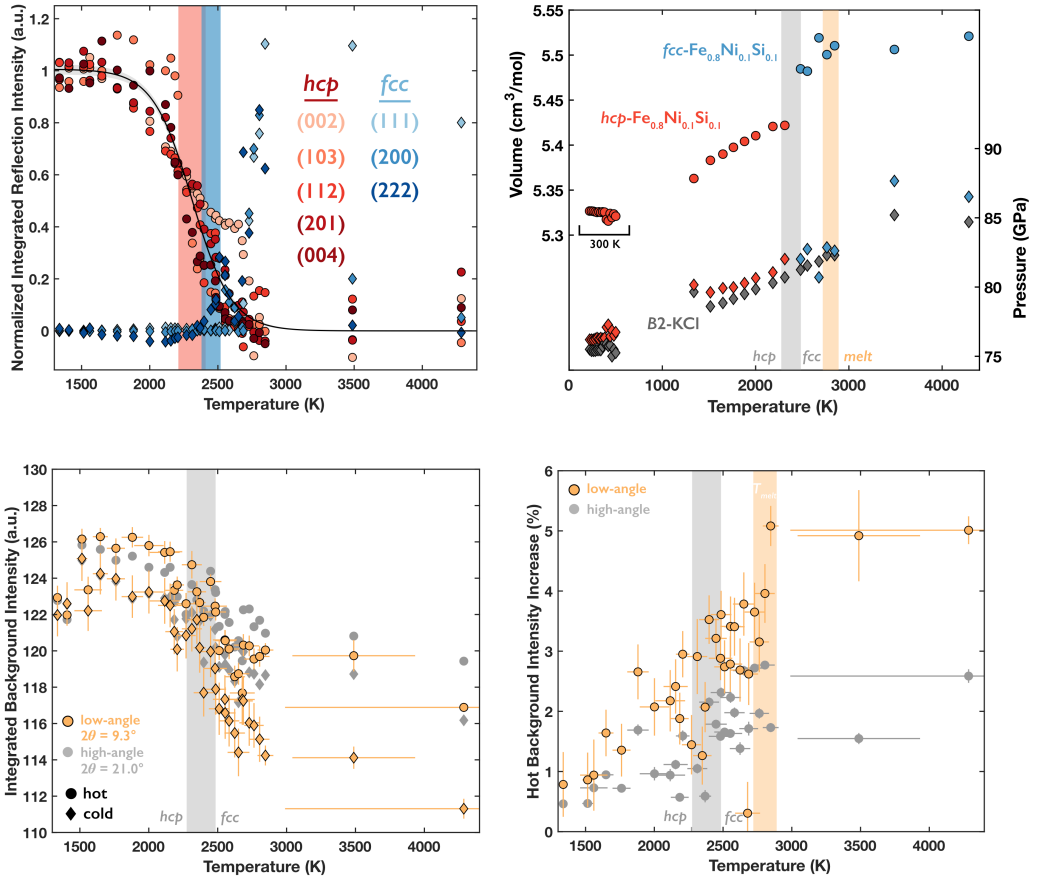

Figure C.8: Burst XRD heating run D6P2S3. Top left: Changes in normalized integrated intensities from multiple *hcp*- (red) and *fcc*-$Fe_{0.8}Ni_{0.1}Si_{0.1}$ (blue) reflections. Shaded bars represent *hcp*-out (red) and *hcp*-in (blue) temperatures. Top right: Unit-cell volumes (left y-axis and circles) and pressures (right y-axis and diamonds) for *hcp*- (red) and *fcc*-$Fe_{0.8}Ni_{0.1}Si_{0.1}$ (blue) and *B*2-KCl (gray). 300 K measurement results are spaced out for ease of viewing in the order of acquisition sequence, from first (leftmost) to last (rightmost) heat and quench step. Shaded bars represent *hcp-fcc* transition (gray) and melting temperature (orange) for this and subsequent panels. Bottom left: Integrated background intensities at low-angle (orange points) and high-angle (gray points) regions for hot (circles) and cold (diamonds) patterns. Bottom right: Normalized background intensities after the background updating procedure (Section 4.3.2) for the low-angle (orange) and high-angle (gray) regions. See Table C.1 for further details.

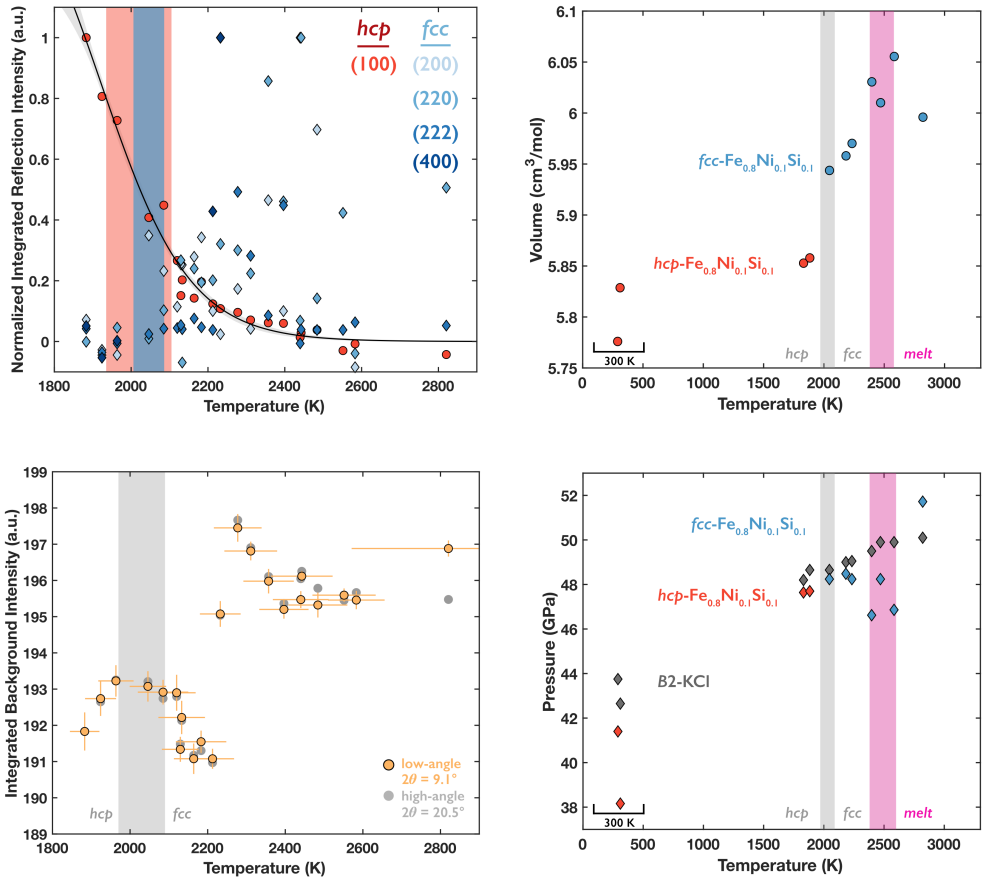

Figure C.9: Continuous XRD heating run D1P1cM. Top left: Changes in normalized integrated intensities from multiple *hcp*- (red) and *fcc*-$Fe_{0.8}Ni_{0.1}Si_{0.1}$ (blue) reflections. Shaded bars represent *hcp*-out (red) and *hcp*-in (blue) temperatures. Top right: Unit-cell volumes for *hcp*- (red) and *fcc*-$Fe_{0.8}Ni_{0.1}Si_{0.1}$ (blue) and *B*2-KCl (gray). 300 K measurement results are spaced out for ease of viewing, with the before-heating measurement to the left and the after-heating measurement to the right. Shaded bars represent *hcp-fcc* transition (gray) and melting temperature (purple) for this and subsequent panels. Bottom left: Integrated background intensities at low-angle (orange points) and high-angle (gray points) regions for hot patterns. Bottom right: Pressures of *hcp*- (red) and *fcc*-$Fe_{0.8}Ni_{0.1}Si_{0.1}$ (blue) and *B*2-KCl (gray). For continuous heating runs, the background updating method cannot be implemented and no liquid diffuse signal can be detected. Instead, the melting temperature is determined by the onset of plateaus in the volume (top right panel) as a function of temperature, as described in Section 4.3.2. See Table C.1 for further details.

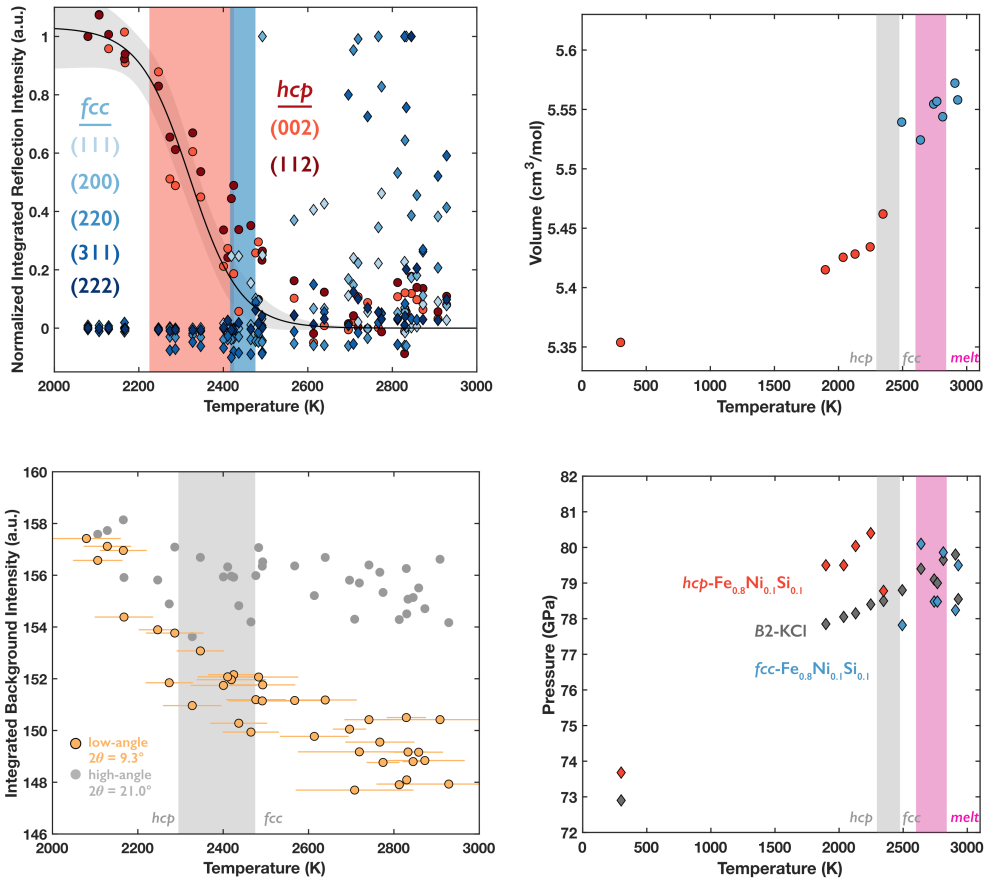

Figure C.10: Continuous XRD heating run D6P2S4. Top left: Changes in normalized integrated intensities from multiple *hcp*- (red) and *fcc*-$Fe_{0.8}Ni_{0.1}Si_{0.1}$ (blue) reflections. Shaded bars represent *hcp*-out (red) and *hcp*-in (blue) temperatures. Top right: Unit-cell volumes for *hcp*- (red) and *fcc*-$Fe_{0.8}Ni_{0.1}Si_{0.1}$ (blue) and *B*2-KCl (gray). 300 K measurement results are spaced out for ease of viewing, with the before-heating measurement to the left and the after-heating measurement to the right. Shaded bars represent *hcp-fcc* transition (gray) and melting temperature (purple) for this and subsequent panels. Bottom left: Integrated background intensities at low-angle (orange points) and high-angle (gray points) regions for hot patterns. Bottom right: Pressures of *hcp*- (red) and *fcc*-$Fe_{0.8}Ni_{0.1}Si_{0.1}$ (blue) and *B*2-KCl (gray). For continuous heating runs, the background updating method cannot be implemented and no liquid diffuse signal can be detected. Instead, the melting temperature is determined by the onset of plateaus in the volume (top right panel) as a function of temperature, as described in Section 4.3.2. See Table C.1 for further details.

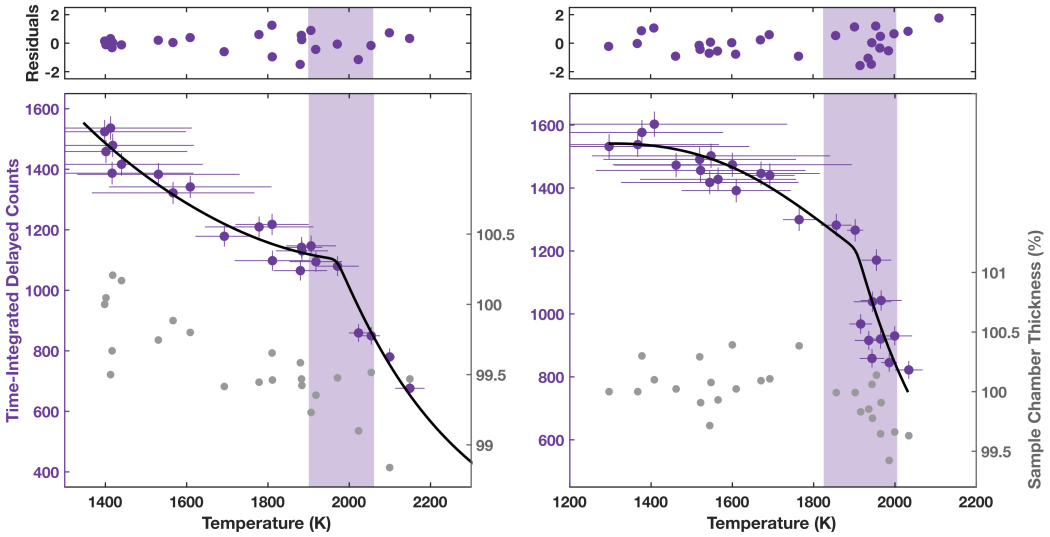

Figure C.11: SMS heating runs D9S1 (left) and D9S2 (right) (22-24 GPa). A scattering intensity model (solid black line) is fit to the delayed counts-temperature profile (purple points, left axis) in MINUTI (Sturhahn, 2021) to constrain the melting temperature (purple bar). Changes in sample chamber thickness (gray points, right axis) are calculated from total x-ray transmission intensity changes and are limited to less than 2% for all heating runs. Residuals from the fits are shown in units of standard deviation. See Table C.1 for further details.

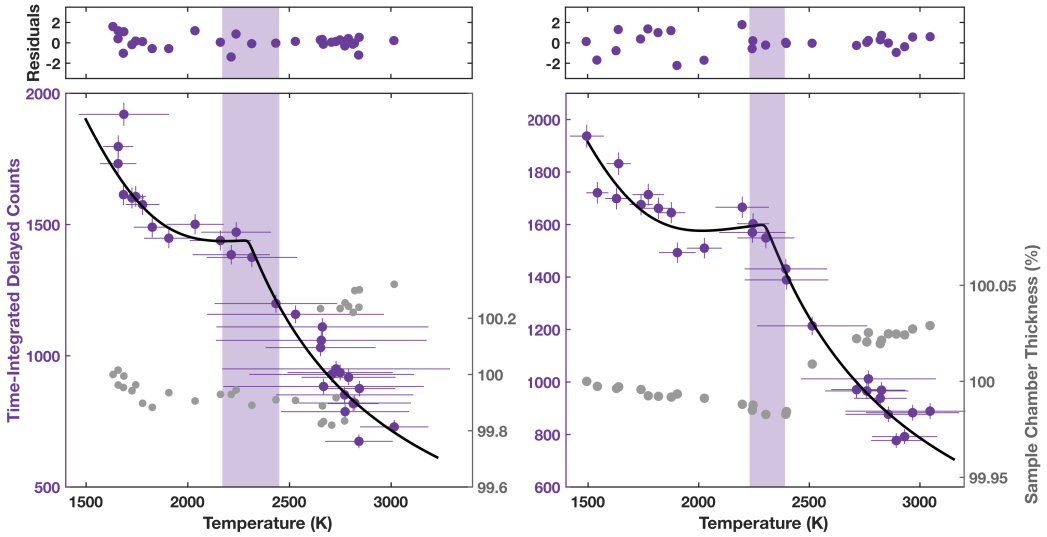

Figure C.12: SMS heating runs CP4S1 (left) and CP4S2 (right) (34-38 GPa). A scattering intensity model (solid black line) is fit to the delayed counts-temperature profile (purple points, left axis) in MINUTI (Sturhahn, 2021) to constrain the melting temperature (purple bar). Changes in sample chamber thickness (gray points, right axis) are calculated from total x-ray transmission intensity changes and are limited to less than 2% for all heating runs. Residuals from the fits are shown in units of standard deviation. See Table C.1 for further details.

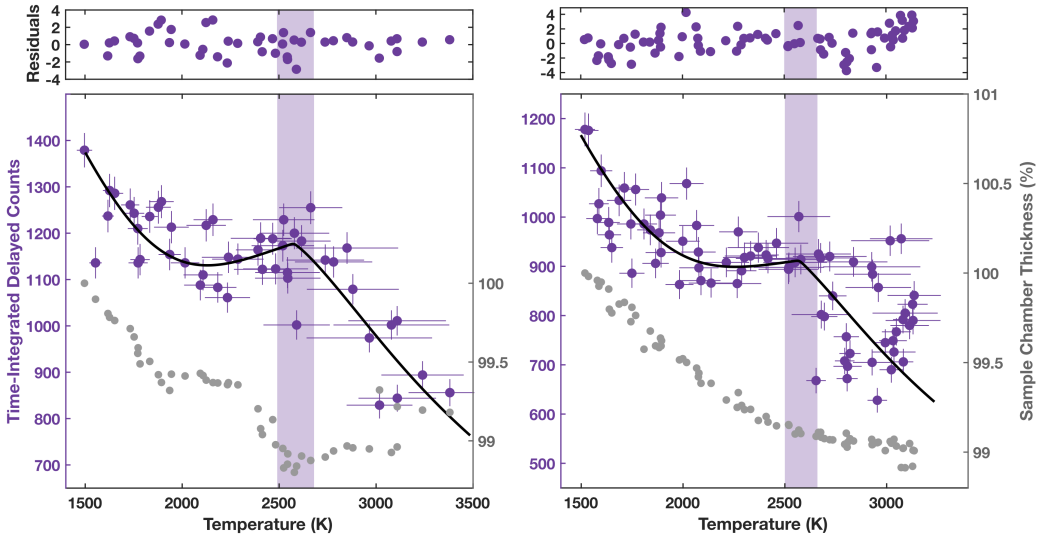

Figure C.13: SMS heating runs D6S1 (left) (49-54 GPa) and D6S2 (right) (54-57 GPa). A scattering intensity model (solid black line) is fit to the delayed counts-temperature profile (purple points, left axis) in MINUTI (Sturhahn, 2021) to constrain the melting temperature (purple bar). Changes in sample chamber thickness (gray points, right axis) are calculated from total x-ray transmission intensity changes and are limited to less than 2% for all heating runs. Residuals from the fits are shown in units of standard deviation. See Table C.1 for further details.

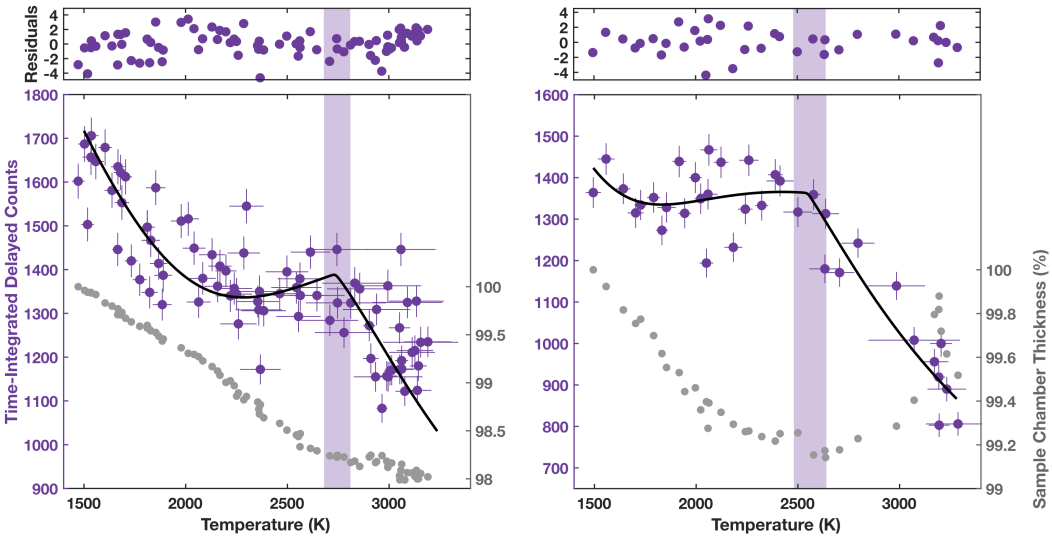

Figure C.14: SMS heating runs D7c (left) (71-75 GPa) and D1S2 (right) (42-47 GPa). A scattering intensity model (solid black line) is fit to the delayed counts-temperature profile (purple points, left axis) in MINUTI (Sturhahn, 2021) to constrain the melting temperature (purple bar). Changes in sample chamber thickness (gray points, right axis) are calculated from total x-ray transmission intensity changes and are limited to less than 2% for all heating runs. Residuals from the fits are shown in units of standard deviation. See Table C.1 for further details.

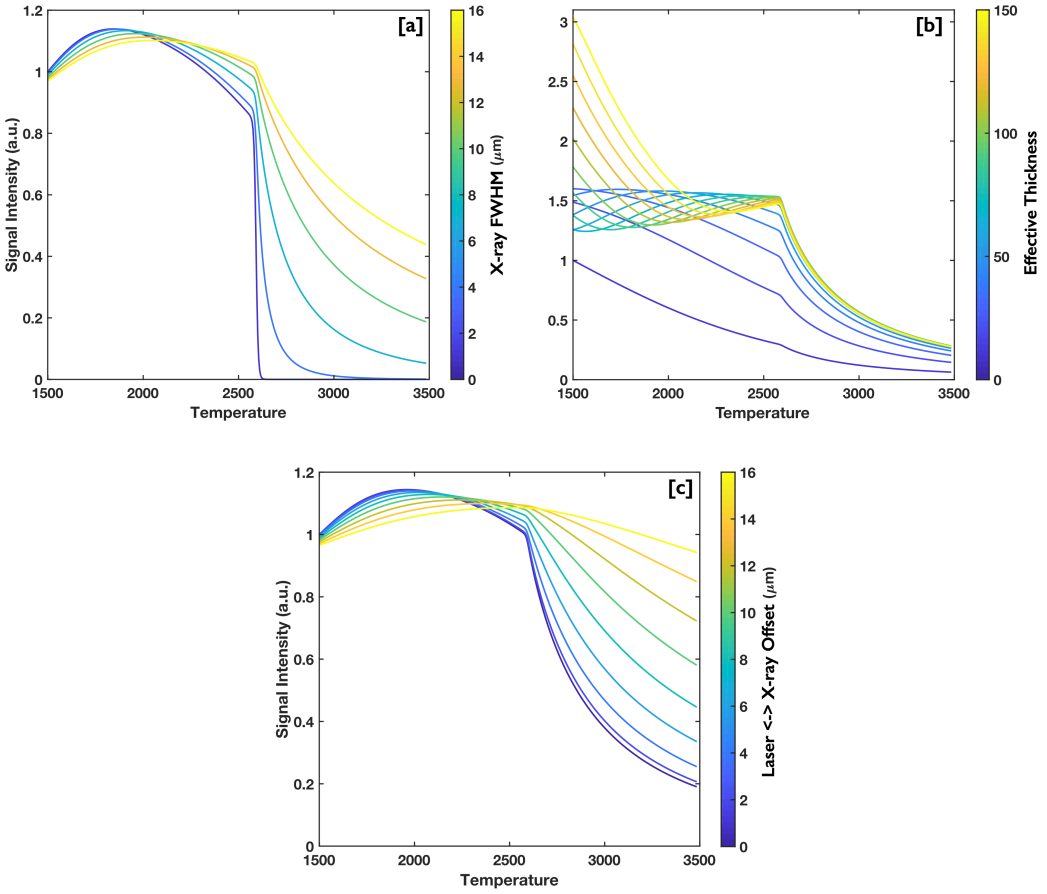

Figure C.15: Forward models of Mössbauer signal (time-integrated delayed counts) intensity as a function of temperature. All panels are calculated with a constant laser hotspot FWHM of 35 μm and a constant melting temperature set to 2600 K. Panel [a] shows the effect of x-ray beam size, with constant effective thickness (50), and x-ray offsets (0 μm). Larger x-ray beams traverse a larger radial gradient of sample temperatures, leading to a shallower drop-off of intensity. Panel [b] shows the effect of effective thickness, with constant x-ray beam size (14 μm) and offsets (0 μm). Panel [c] shows the effect of lateral offset between the x-ray beam and the laser hotspot, with constant x-ray size (14 μm) and effective thickness (50). Offset magnitude is constrained in the fitting procedure (Table C.1) and is in good agreement with the $\sim$10 μm magnitude visually estimated during heating runs with CCD cameras. Effective thickness is dimensionless and is the product of the numerical density of the ^{57}Fe atoms, the physical thickness of the sample, the nuclear resonant cross-section (2.56x10^{-22} m^2 for ^{57}Fe), and the Lamb-Mössbauer factor (probability of recoil-free scattering events).

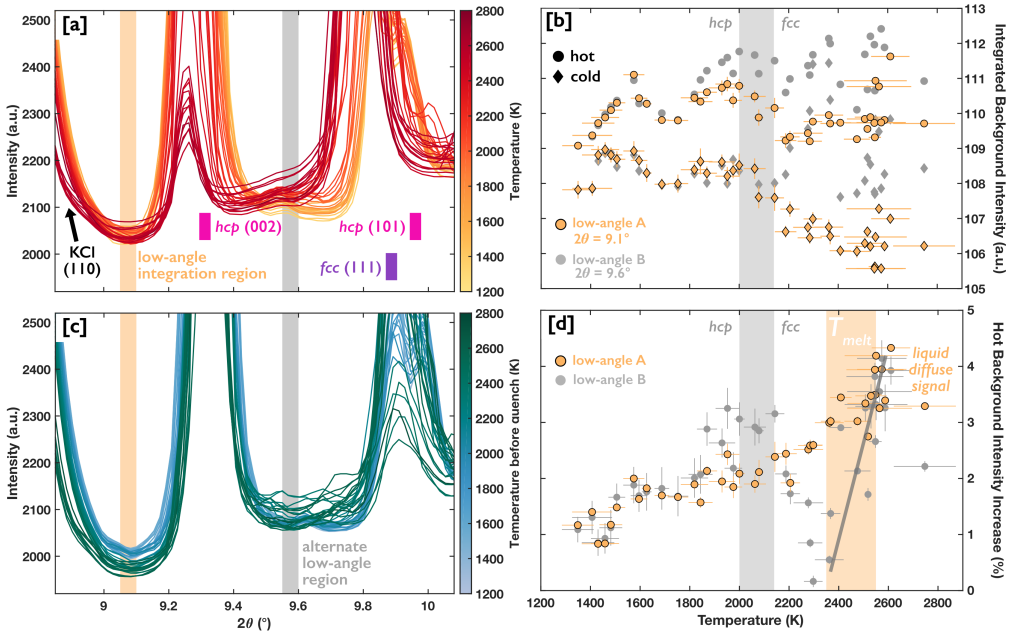

Figure C.16: Background analysis as described in Section 4.3.2 and Fig. 4.4 applied to a nearby alternate low-angle integration region (2θ=9.6°, gray bar in panels [a, c]). A discontinuous increase in background intensity is identified at the same temperature as for the original integration region (orange bar, panel [d]), suggesting good agreement in melting temperatures determined from different low-angle integration regions. Greater scatter in background intensities for this region is likely a result of recrystallization effects from the nearby *fcc* peak (purple tick, panel [a]) that is present in some quenched patterns due to the sluggish back-transformation.

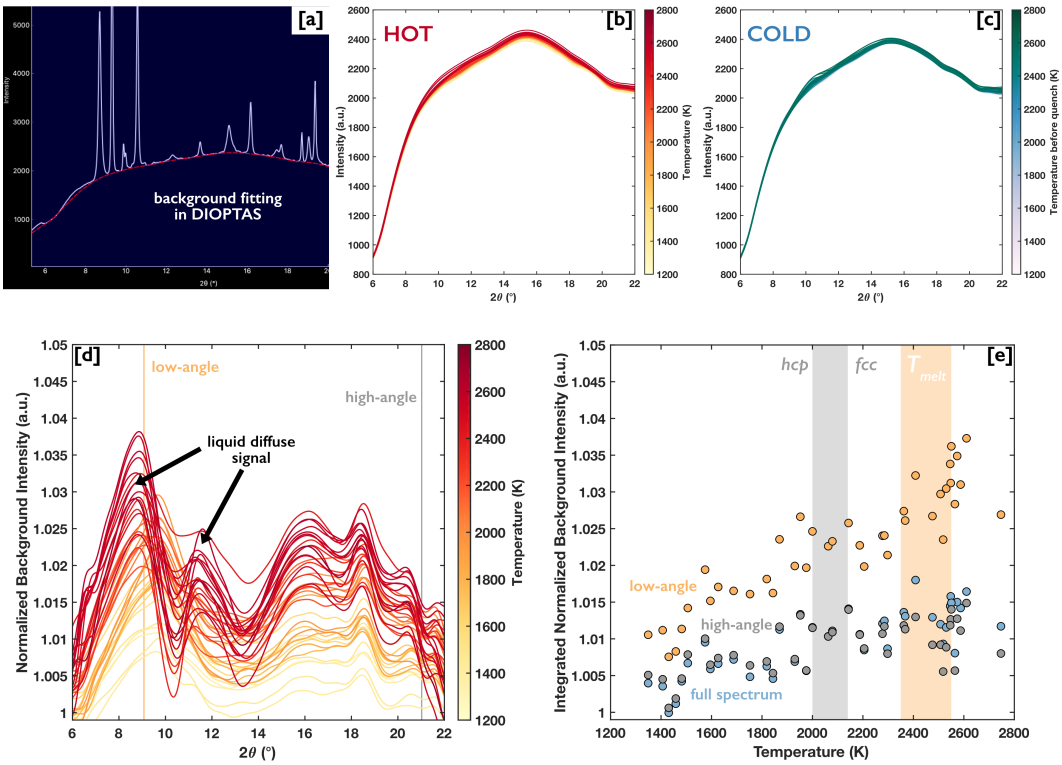

Figure C.17: Analysis of fits to background shapes for detecting liquid diffuse signals. Panel [a]: Example of a fit to the background shape in DIOPTAS. Panels [b] and [c]: Fits produced using DIOPTAS for the hot and cold patterns for heating run D1P2S3, respectively. Panel [d]: Hot pattern background fits ([b]) normalized by cold pattern background fits ([c]). Shaded bars represent the low-angle (orange) and high-angle (gray) integration regions shown in Fig. 4.4. Black arrows identify background intensity attributed to the liquid diffuse signal as the sample is heated above the melting temperature. The signal shape arises from the oscillations of the liquid structure factor, as shown for liquid iron by Kuwayama et al. (2020). Panel [e]: Integrated intensities for the two integration regions (low-angle: orange, high-angle: gray), as well as for the full scattering angle region of the entire XRD pattern (6-22θ). Shaded bars represent the *hcp-fcc* transition (gray) and the melting temperature as determined in Fig. 4.4 using the analysis described in Section 4.3.2. Only the low-angle region allows for the possible detection of a liquid diffuse signal, though the discontinuous change in the intensity trend as a function of temperature at melting is more difficult to identify compared to the original analysis in Fig. 4.4 and Section 4.3.2. See Text C.3 for further discussion.

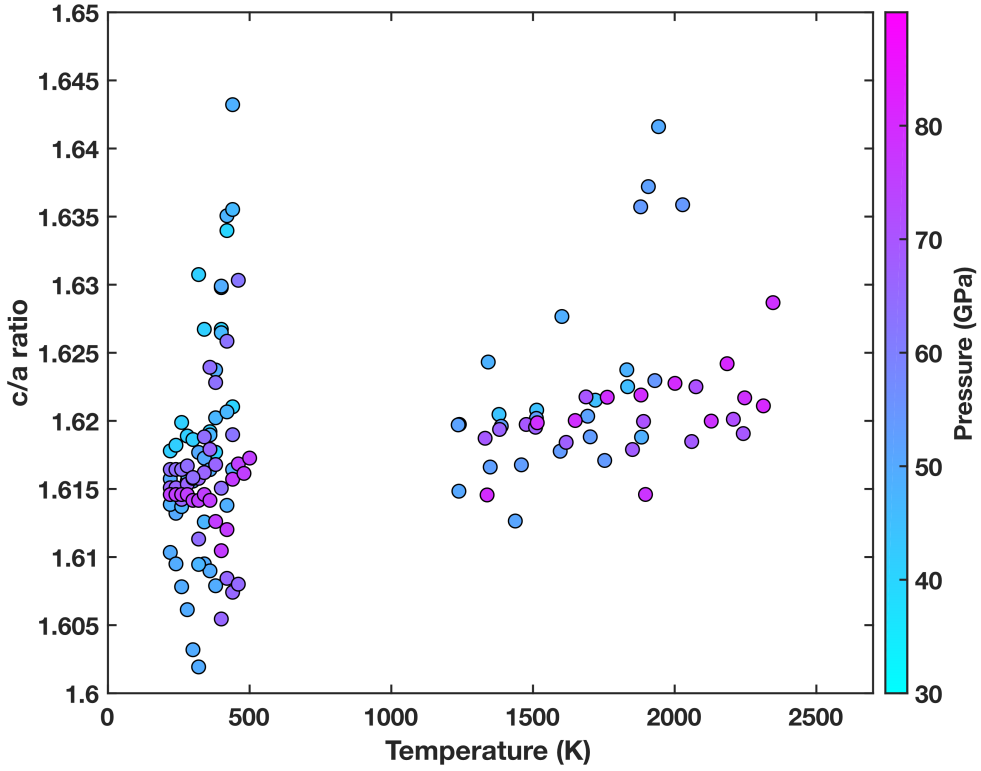

Figure C.18: Compilation of all c/a ratios for *hcp*-$Fe_{0.8}Ni_{0.1}Si_{0.1}$ measured in this study. 300 K measurement results are spaced out for ease of viewing in the order of acquisition sequence, from first (leftmost) to last (rightmost) heat and quench step. 300 K values cluster around 1.615, in agreement with previous measurements on this identical material in a helium pressure medium (Morrison et al., 2018), but with more scatter caused by recrystallization effects during heating and quenching across the *hcp-fcc* boundary. A small temperature dependence of c/a ratios is in agreement with previous high-temperature measurements on a similar Fe-Ni-Si alloy (Komabayashi, Pesce, Sinmyo, et al., 2019).

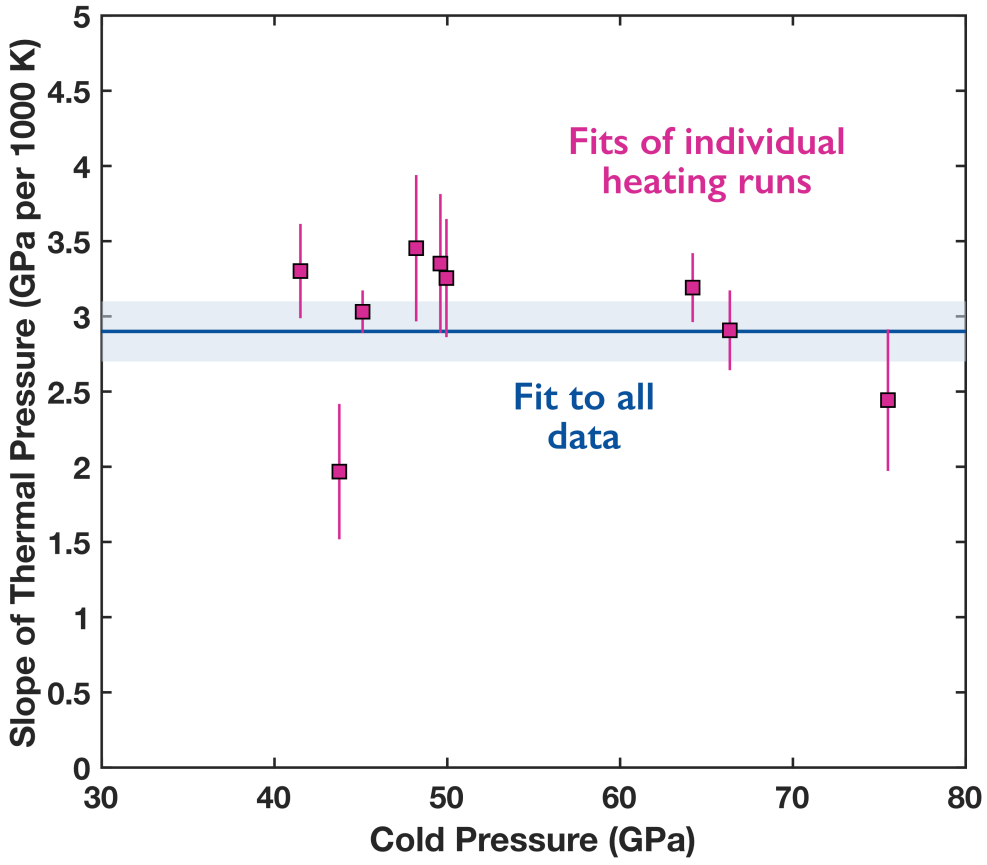

Figure C.19: Thermal pressure slopes constrained for each individual heating run (pink squares) plotted as a function of starting 300 K sample pressure. Absence of pressure dependence in the thermal pressure slopes from individual heating run fits supports the choice of a linear thermal pressure model (blue line) applied to SMS measurements to determine pressure at melting. See Text C.5 and Figs. C.20-C.21 for further details.

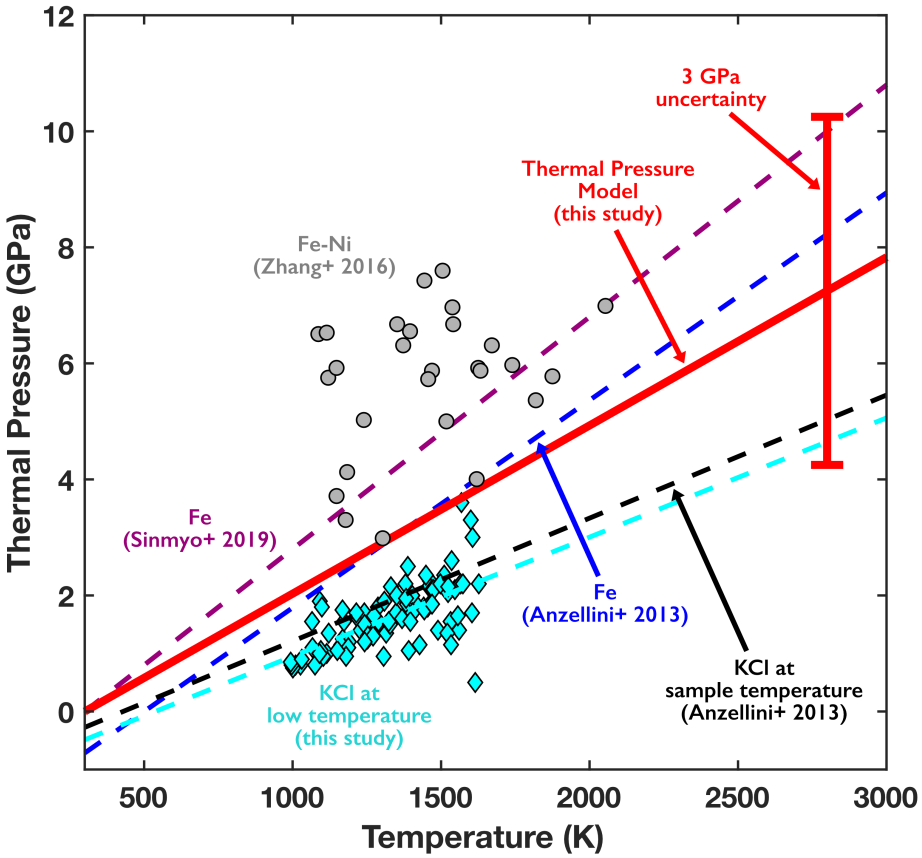

Figure C.20: Thermal pressure model (solid red line) constructed from in-situ pressure measurements in this study (Section 4.3.3), used to calculate melting pressures for SMS measurements and previous data on the melting of Fe and Fe-Ni (Text C.7). The 3 GPa uncertainty added to calculated melting pressures is demonstrated at 2800 K with error bars. The model is consistent with previous *in-situ* pressure measurements for Fe (blue – Anzellini et al., 2013, purple – Sinmyo et al., 2019) and Fe-Ni (gray – D. Zhang et al., 2016), as well as for the KCl pressure medium at upper bound (black – Anzellini et al., 2013) and lower bound (cyan – this study) temperature estimates. See Text C.5 for further discussion. Results from Anzellini et al. (2013) represent fits to data as shown in Fig. C.21 and discussed in Text C.5.

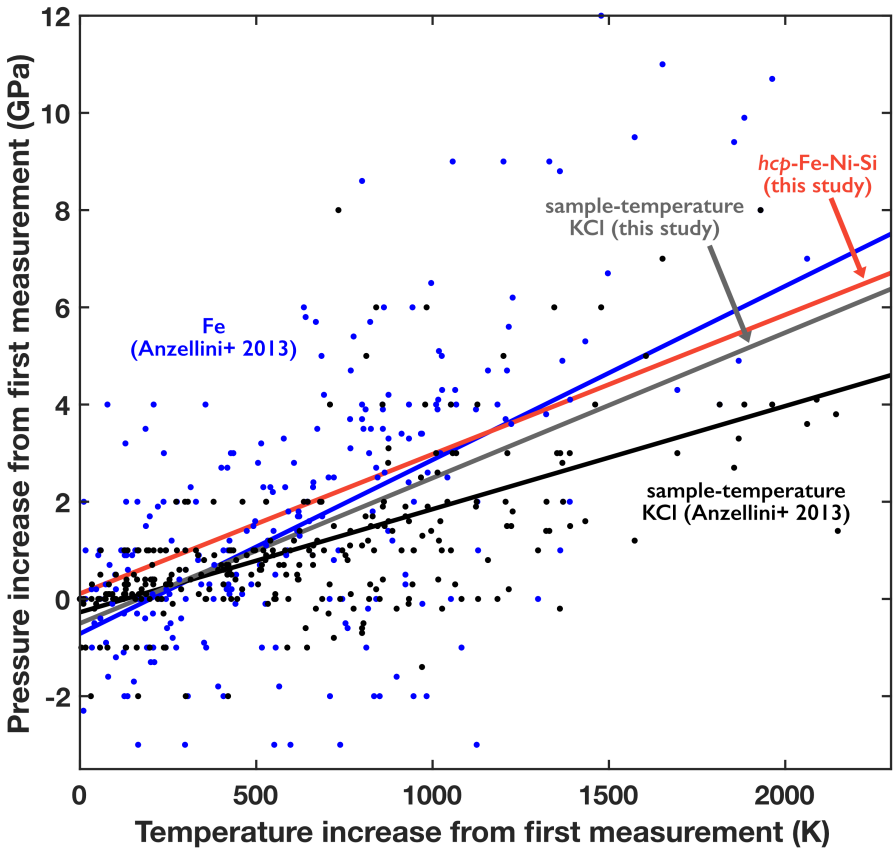

Figure C.21: Thermal pressure data on an Fe foil in a KCl pressure medium reported by Anzellini et al. (2013). As the authors did not report 300 K measurements, data presented here are calculated as pressure increase from the first reported measurement as a function of temperature increase from the first reported measurement. Data are shown for Fe pressures (blue) and KCl pressures (black), where the KCl temperature is assumed to be identical to the sample temperature. Solid blue and black lines represent fits to the thermal pressure data for Fe and KCl, respectively. Solid red and gray lines represent fits to the thermal pressure data from this study for Fe-Ni-Si and KCl, respectively, showing good agreement with thermal pressures from Anzellini et al. (2013). Comparison with previous studies is further discussed in Text C.5 and shown in Fig. C.20.

Appendix D

SUPPLEMENTARY MATERIAL FOR CHAPTER 5

Table D.1: *P-T* conditions of the vacancy order-disorder transition measured in the XRD heating runs.

Heating run	$P_{1,\,KCl}$ (GPa)	$P_{1,\,FeO}$ (GPa)	P_1 (GPa)	δP_1 (GPa)	T_1 (K)	δT_1 (K)
22D9S1	39.5	38.8	38.9	1.6	2570	130
22D9S2	37.7	37.4	37.6	1.1	2680	80
21D1S3	63.1	63.7	63.4	2.3	2950	250
21D1S2	64.5	65.1	64.8	2.3	3020	120
21D1S1	65.6	66.6	66.1	2.5	2950	150
22D1S2	68.5	68.3	68.4	2.1	3000	160
22D1S1	65.3	68.1	66.7	3.4	3050	150
20D4S2	72.9	69.9	71.4	3.5	3050	150
20D4S1	74.7	73.4	74.1	1.7	3150	150
20D4S3	74.7	74.4	74.5	1.2	3180	160
20D4S4	74.8	74.7	74.8	1.1	3200	200
21D7S1	91.9	95.0	93.5	4.5	3250	200
21D7S1	95.0	92.9	93.9	5.0	3250	160
21D8S1	113.4	113.6	113.5	4.1	3400	180
21D8S2	113.2	116.3	114.7	5.6	3480	220
21D8S3	112.8	120.6	116.7	7.9	3400	200
21D8S4	115.1	117.2	116.1	5.0	3500	200
22D7S1	131.7	134.2	132.9	6.2	3500	250
22D7S2	136.6	136.5	136.5	5.1	3550	220

Table D.2: *P-T* conditions of the melting transition measured in the XRD heating runs.

Heating run	$P_{2,\,KCl}$ (GPa)	$P_{2,\,FeO}$ (GPa)	P_2 (GPa)	δP_2 (GPa)	T_2 (K)	δT_2 (K)
22D9S1	38.3	38.3	38.3	2	2800	120
22D9S2	34.0	38.1	36.0	4.1	2850	100
22D1S1	67.1	71.6	69.3	4.2	3500	150
20D4S3	75.8	76.8	76.3	2.5	3500	150
20D4S4	75.6	76.7	76.1	2.5	3550	150
21D8S1	115.7	119.5	117.6	3.9	3950	120
21D8S2	114.9	120.3	117.6	5.7	4000	200
21D8S4	116.1	120.8	118.4	5.3	3950	200
22D7S1	135.2	137.9	136.5	5.4	4050	200
22D7S2	138.8	140.1	139.5	5.7	4200	220

Table D.3: Details of the SMS heating run results.

Heating run	Starting P_{ruby} (GPa)	P_{melt} (GPa)	δP_{melt} (GPa)	T_{melt} (K)	δT_{melt} (K)	χ^2
18D4P2	30	37	3	2920	105	0.37
18D4P3	40	48	3	3130	110	0.76
18D6S1a	50	59	3	3400	110	1.64

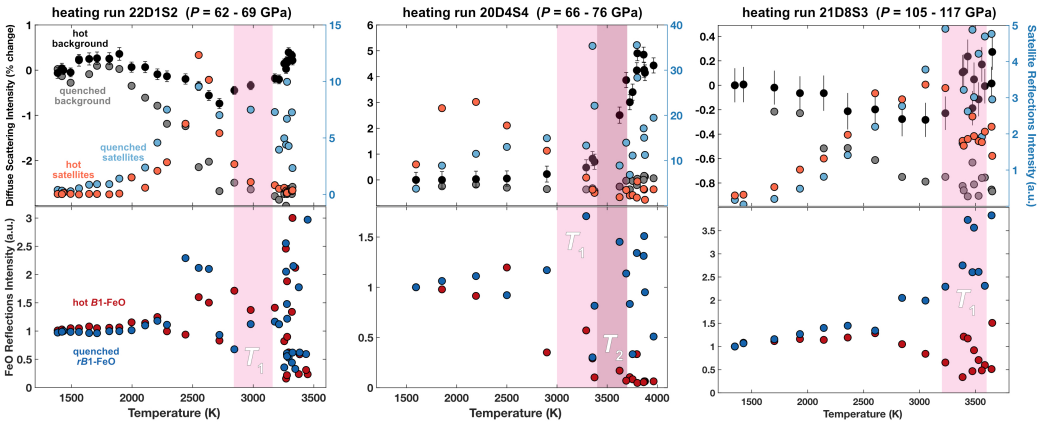

Figure D.1: Three additional XRD heating runs, showing trends discussed in 5.4.1.